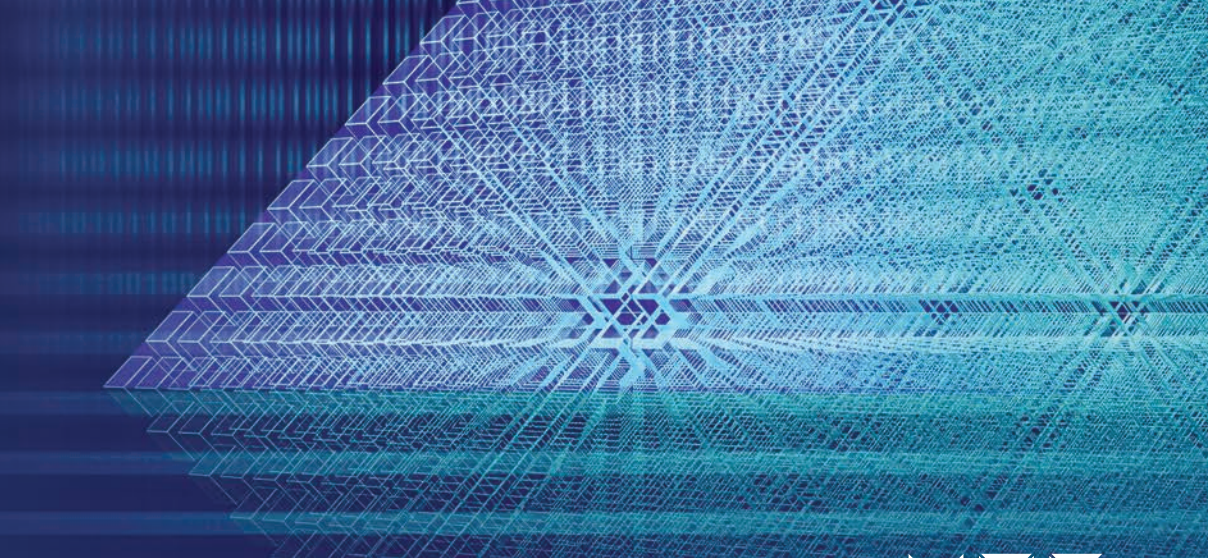

TECHNICAL REPORTS SERIES NO. 485

Improvement of the Reliability and Accuracy of Heavy Ion Beam Analysis

IAEA
International Atomic Energy Agency

IMPROVEMENT OF THE RELIABILITY AND ACCURACY OF HEAVY ION BEAM ANALYSIS

The following States are Members of the International Atomic Energy Agency:

AFGHANISTAN
ALBANIA
ALGERIA
ANGOLA
ANTIGUA AND BARBUDA
ARGENTINA
ARMENIA
AUSTRALIA
AUSTRIA
AZERBAIJAN
BAHAMAS
BAHRAIN
BANGLADESH
BARBADOS
BELARUS
BELGIUM
BELIZE
BENIN
BOLIVIA, PLURINATIONAL STATE OF
BOSNIA AND HERZEGOVINA
BOTSWANA
BRAZIL
BRUNEI DARUSSALAM
BULGARIA
BURKINA FASO
BURUNDI
CAMBODIA
CAMEROON
CANADA
CENTRAL AFRICAN REPUBLIC
CHAD
CHILE
CHINA
COLOMBIA
CONGO
COSTA RICA
CÔTE D'IVOIRE
CROATIA
CUBA
CYPRUS
CZECH REPUBLIC
DEMOCRATIC REPUBLIC OF THE CONGO
DENMARK
DJIBOUTI
DOMINICA
DOMINICAN REPUBLIC
ECUADOR
EGYPT
EL SALVADOR
ERITREA
ESTONIA
ESWATINI
ETHIOPIA
FIJI
FINLAND
FRANCE
GABON
GEORGIA
GERMANY
GHANA
GREECE
GRENADA
GUATEMALA
GUYANA
HAITI
HOLY SEE
HONDURAS
HUNGARY
ICELAND
INDIA
INDONESIA
IRAN, ISLAMIC REPUBLIC OF
IRAQ
IRELAND
ISRAEL
ITALY
JAMAICA
JAPAN
JORDAN
KAZAKHSTAN
KENYA
KOREA, REPUBLIC OF
KUWAIT
KYRGYZSTAN
LAO PEOPLE'S DEMOCRATIC REPUBLIC
LATVIA
LEBANON
LESOTHO
LIBERIA
LIBYA
LIECHTENSTEIN
LITHUANIA
LUXEMBOURG
MADAGASCAR
MALAWI
MALAYSIA
MALI
MALTA
MARSHALL ISLANDS
MAURITANIA
MAURITIUS
MEXICO
MONACO
MONGOLIA
MONTENEGRO
MOROCCO
MOZAMBIQUE
MYANMAR
NAMIBIA
NEPAL
NETHERLANDS
NEW ZEALAND
NICARAGUA
NIGER
NIGERIA
NORTH MACEDONIA
NORWAY
OMAN
PAKISTAN
PALAU
PANAMA
PAPUA NEW GUINEA
PARAGUAY
PERU
PHILIPPINES
POLAND
PORTUGAL
QATAR
REPUBLIC OF MOLDOVA
ROMANIA
RUSSIAN FEDERATION
RWANDA
SAINT LUCIA
SAINT VINCENT AND THE GRENADINES
SAN MARINO
SAUDI ARABIA
SENEGAL
SERBIA
SEYCHELLES
SIERRA LEONE
SINGAPORE
SLOVAKIA
SLOVENIA
SOUTH AFRICA
SPAIN
SRI LANKA
SUDAN
SWEDEN
SWITZERLAND
SYRIAN ARAB REPUBLIC
TAJIKISTAN
THAILAND
TOGO
TRINIDAD AND TOBAGO
TUNISIA
TURKEY
TURKMENISTAN
UGANDA
UKRAINE
UNITED ARAB EMIRATES
UNITED KINGDOM OF GREAT BRITAIN AND NORTHERN IRELAND
UNITED REPUBLIC OF TANZANIA
UNITED STATES OF AMERICA
URUGUAY
UZBEKISTAN
VANUATU
VENEZUELA, BOLIVARIAN REPUBLIC OF
VIET NAM
YEMEN
ZAMBIA
ZIMBABWE

The Agency's Statute was approved on 23 October 1956 by the Conference on the Statute of the IAEA held at United Nations Headquarters, New York; it entered into force on 29 July 1957. The Headquarters of the Agency are situated in Vienna. Its principal objective is "to accelerate and enlarge the contribution of atomic energy to peace, health and prosperity throughout the world''.

TECHNICAL REPORTS SERIES No. 485

IMPROVEMENT OF THE RELIABILITY AND ACCURACY OF HEAVY ION BEAM ANALYSIS

INTERNATIONAL ATOMIC ENERGY AGENCY
VIENNA, 2019

COPYRIGHT NOTICE

Marketing and Sales Unit, Publishing Section
International Atomic Energy Agency
Vienna International Centre
PO Box 100
1400 Vienna, Austria
fax: +43 1 26007 22529
tel.: +43 1 2600 22417
email: sales.publications@iaea.org
www.iaea.org/books

Printed by the IAEA in Austria
May 2019
STI/PUB/010/485

IAEA Library Cataloguing in Publication Data

Names: International Atomic Energy Agency.
Title: Improvement of the reliability and accuracy of heavy ion beam analysis / International Atomic Energy Agency.
Description: Vienna : International Atomic Energy Agency, 2019. | Series: Technical reports series (International Atomic Energy Agency), ISSN 0074–1914 ; no. 485 | Includes bibliographical references.
Identifiers: IAEAL 19-01230 | ISBN 978–92–0–103517–2 (paperback : alk. paper)
Subjects: LCSH: Ion bombardment. | Stopping power (Nuclear physics). | Solids — Effect of radiation on.
Classification: UDC 539.1 | STI/DOC/010/485

FOREWORD

Many emerging technologies are based on the development of advanced engineering materials capable of withstanding higher temperatures, higher stresses, and more aggressive corrosive and oxidizing environments than their predecessors. These advanced materials may be more efficient and more sensitive, and therefore more suitable for use in high technology products such as light emitting materials, sensors and lasers. Nuclear analytical facilities and techniques are available to support research in this area and development of new light element composites and alloys. Nuclear analytical techniques using heavy ions from particle accelerators have demonstrated a competitive advantage in that they can provide important information about the concentrations, distributions and locations of light elements that are not readily available or accessible using non-nuclear spectrometries. The coordinated research project described in this publication helped to address identified shortcomings and limitations in the use of heavy ions through the delivery of better analytical tools with a higher degree of reliability, accuracy and user confidence.

This publication includes a detailed description of experimental procedures and data evaluation practice, in conjunction with relevant theory, with detail not readily available in widely disseminated scientific publications. Such advanced and complex knowledge can usually only be gained through on the job training, or through working with experts, which are not efficient means of mass dissemination. The new stopping cross-section dataset is a real asset as it includes extensive new data not available before. All these elements will significantly contribute to knowledge transfer in the ion beam community, leading to improvement of the accuracy of quantitative light element analysis worldwide, with a special emphasis on materials science. The intended audience of this publication includes students and highly skilled researchers.

The IAEA wishes to acknowledge the assistance of all the experts who contributed to the outcomes of this coordinated research project. The IAEA also acknowledges N.P. Barradas (Portugal) for compiling the project results, establishing a framework for their analysis and drafting this publication.

The IAEA officer responsible for this publication was A. Simon of the Division of Physical and Chemical Sciences.

EDITORIAL NOTE

Although great care has been taken to maintain the accuracy of information contained in this publication, neither the IAEA nor its Member States assume any responsibility for consequences which may arise from its use.

This publication does not address questions of responsibility, legal or otherwise, for acts or omissions on the part of any person.

Guidance provided here, describing good practices, represents expert opinion but does not constitute recommendations made on the basis of a consensus of Member States.

The use of particular designations of countries or territories does not imply any judgement by the publisher, the IAEA, as to the legal status of such countries or territories, of their authorities and institutions or of the delimitation of their boundaries.

The mention of names of specific companies or products (whether or not indicated as registered) does not imply any intention to infringe proprietary rights, nor should it be construed as an endorsement or recommendation on the part of the IAEA.

The IAEA has no responsibility for the persistence or accuracy of URLs for external or third party Internet web sites referred to in this book and does not guarantee that any content on such web sites is, or will remain, accurate or appropriate.

CONTENTS

1. INTRODUCTION

1.1. BACKGROUND

The successful development and deployment of advanced technologies requires solutions to be found for many material related problems and challenges. These solutions can range from the ability to design, engineer and manufacture suitable candidate materials, to the reliable prediction of their service life performance from accelerated testing conditions, to the provision of suitable analytical tools and instruments for materials analysis.

Nuclear analytical techniques are extremely useful tools for the analysis of materials and are able to support and provide significant contributions to many of these areas. While nuclear analytical techniques are often complementary to non-nuclear techniques, nuclear analytical techniques can, in many cases, provide information that cannot be obtained through alternative methods. Hence, the continued and expanded use of nuclear analytical techniques will be required in the material characterization community.

The nuclear analytical technique ion beam analysis (IBA) uses energetic ions to probe matter. IBA encompasses a large set of different techniques, which together can probe the compositional depth profile and structure of samples of all types, provenances and purposes, from fundamental science to technologically advanced materials.

Taken as a whole, IBA is sensitive to all the elements in the periodic table. The accessible depth varies from the surface-most atomic layer to about a tenth of a millimetre. The sensitivity of the analysis is often around one in a thousand, but it can also reach part per million levels in favourable cases, and even part per billion levels in extreme cases. Quantification is usually based on first principles, without the need for standards. In fact, many analytical techniques, both nuclear and non-nuclear, use IBA to characterize standard samples that are required for quantification.

The reliable determination and quantification of light elements in materials ($Z < 14$) is of importance in the development of advanced materials, both for energy and non-energy applications. Heavy ion beams from accelerators (principally, chlorine, bromine and iodine) provide a tool capable of analysing light and heavy elements simultaneously in thin films and on surfaces of materials; heavy ion beams do not suffer from many drawbacks encountered with other light element spectrometries. Heavy ion elastic recoil detection analysis (ERDA) is being called on to analyse increasingly complex materials, particularly those composed of light elements such as glass and ceramics. However, new materials

can pose new problems and challenges for data analysis and interpretations, which must be adequately addressed.

Many advanced materials derive their functional properties from compounds containing light elements. Applications abound for thin films tailored for electrical, electronic, optical and magnetic properties. Advanced engineering materials pose many bulk and surface related material challenges. High temperatures, high stresses, and corrosive and oxidizing environments all place high demands on material properties and performance, spawning the development of carbon and oxide ceramic materials. Carbon based materials (e.g. tungsten carbide, titanium carbide, silicon carbide) have very high resistance to high heat loads and can be extremely hard, making them useful for high temperature heat pipes, superhard cutting tools and plasma facing materials. Alumina, zirconia and magnesium alloys are being developed for oxidation and corrosion resistant protective coatings.

Light elements are important components in many materials of nuclear interest, with oxide ceramic and glass matrices for nuclear waste immobilization being of particular relevance and importance. Many studies are being undertaken to investigate the chemical durability of the surfaces of those materials against radiation induced and chemical induced damage, surface behaviour being an important issue in the qualification of nuclear matrices.

IBA provides very efficient investigative tools for evaluations, in which heavy ion beams from accelerators are applied to analyse surface alterations in a wide range of matrices. However, an issue affecting all of the above cited application areas is that the reliability, quantification and interpretation of data obtained by heavy ion beams from accelerators is not satisfactory and is constrained by inadequacies and inconsistencies in the analytical software codes and basic ion beam data.

Practitioners of IBA are dependent on the availability of suitable analytical software and its ability to provide reliable and correct results. Erroneous results or misinterpretations of a material's structure and composition can result from inadequate science in the analysis software, insufficient accuracy in basic ion beam data, or inadequate documentation and guidance for people to extract the correct information. The need for a comparison and validation of ion beam analytical codes has long been recognized by the IBA and materials science communities. This need has been discussed at several IAEA meetings, resulting in various recommendations to undertake a comparison and validation exercise (see Refs [1, 2]). As a result of these recommendations, resources were made available to conduct an IAEA exercise implemented through two technical meetings on the intercomparison and evaluation of software for accelerator based nuclear techniques of analysis (September 2004, Vienna, and October 2005, Budapest). The outcomes are described by the participants in their final report

entitled International Atomic Energy Agency Intercomparison of Ion Beam Analysis Software and presented as an invited talk at the 18th International Ion Beam Analysis Conference (Hyderabad, India, 2007) [3].

Accurate quantification also depends on the basic data used by the ion beam data evaluation codes, such as scattering cross-sections and stopping powers. To meet the nuclear data needs of the IBA community, the coordinated research project (CRP) entitled Development of a Reference Database for Ion Beam Analysis was initiated by the IAEA in 2005 and was concluded in 2010. On the basis of new data and new evaluations made under the framework of that project, as well as on the data available from the literature, the evaluation of the most widely used differential scattering cross-sections was performed. The data measured were incorporated into the IBANDL database[1]; the evaluated cross-sections were made available to the community through the on-line calculator SigmaCalc[2], both supported by the IAEA. Through the continued inclusion of new data, and through the development of new evaluations, as well as improvements and extensions of existing ones, the need of the IBA community for scattering cross-sections has been effectively met.

Marie Curie noted, in 1900, that "Alpha rays are material projectiles capable of losing velocity when crossing matter" (translation from French)[3] [4]. This is the first reference to what today is called 'stopping power', and it constitutes the basis for the depth sensitivity of IBA techniques. For instance, in Rutherford backscattering, particles backscattered at a deeper layer lose more energy than particles backscattered at a surface layer. By measuring the energy of the backscattered ions, it is possible to determine the depth from which they come, provided the energy loss (i.e. the stopping power) is known.

Theoretical calculation of stopping powers from first principles has seen strong progress over the decades, but an equivalent to SigmaCalc — where extremely reliable values are calculated for practically any system in a very fast manner — does not yet exist. It is not likely that this goal will be reached in the foreseeable future, and in practice, semiempirical interpolative schemes are used. The most widely used method is called the stopping and range of ions in matter (SRIM)[4]. SRIM is based on theoretical formulations and semiempirical models, and it includes a host of adjustable parameters that come from adjusting the models to existing experimental data. This poses a strong constraint for heavy ions because there are about as many stopping power experiments published

---

[1] www-nds.iaea.org/ibandl/

[2] www-nds.iaea.org/sigmacalc/

[3] In the French original: "les rayons alpha sont des projectiles materiels susceptibles de perdre de leur vitesse en traversant la matière" [4].

[4] www.srim.org

for hydrogen and helium as for all other ions taken together. The database of stopping powers for heavy ions is very sparse, and there are no data at all for many systems, including a number that are essential for technologically relevant materials. As a consequence, the average accuracy of SRIM was found to be, for instance, 3% for ^{4}He in the 1–10 MeV/nucleon range. For ions with an atomic number Z from 19 to 92 in solid compounds, the average accuracy was found to be 10.7% [5].

As an example, time of flight–ERDA (TOF–ERDA) spectra were collected at the Ruđer Bošković Institute, Croatia [6], for the National Institute of Standards and Technology standard reference material 2136, which consists of eight thin chromium layers (30 nm) separated by chromium oxide layers (two to three monolayers thick). The total areal density of the sample is certified to be 175.3 ± 6.4 μg/cm^2 and can, therefore, be used to test how well experimental spectra can be simulated using heavy ion SRIM stopping power data. Measurements were performed with different incident ions (^{35}Cl, ^{81}Br, ^{127}I and ^{197}Au). The data for ^{81}Br are shown in Fig. 1, together with the results of state of the art Monte Carlo simulations, marked as 'CORTEO' in the figure. There are strong discrepancies between the experimental and simulated data using SRIM stopping power values, and the discrepancy is different for each recoil; that is, the accuracy of SRIM stopping powers is not the same for all the ions. Clearly, more measurements of heavy ion stopping powers are needed to improve the reliability of heavy IBA experiments.

1.2. OBJECTIVE

The aim of this CRP was to deliver demonstrable improvements in the ability of heavy ion ERDA to analyse light elements with a higher degree of reliability, accuracy and user confidence. Better descriptions and implementations of heavy ion interactions in matter are required, but the strongest constraint identified was the lack of basic stopping power data for heavy ions.

Thus, experimental and simulation activities were undertaken in targeted model systems to acquire data and information to alleviate deficiencies and inadequacies in the analytical methodology, and to improve the reliability and accuracy of heavy ion stopping powers. The ion–target systems for which stopping power measurements were made are given in Table 1, and a summary of the participating laboratories is given in Table 2.

Given that reliability and accuracy of analysis critically depend on the accuracy with which the basic data are known, a very strong effort was made to calculate the accuracy of the stopping powers determined. All the contributions

to accuracy were taken into account by constructing an uncertainty budget for each experiment performed.

The outputs and benefits of this CRP will go beyond ion beam laboratories that use heavy ion beams for materials research to those that use light ion beams for other materials science problems, as the underlying knowledge is common to all ion beam types.

1.3. SCOPE

The scope of this work is determined by the needs of the IBA community. Therefore, this work is dedicated to the determination of stopping power values relevant to IBA, in particular with relevance to heavy ion ERDA.

The ions chosen pertain to two categories: those commonly used as primary beam particles or those commonly found in technologically relevant materials. In the second case, heavy ion ERDA is used to detect the ions as recoil ions; knowledge of their stopping is, therefore, also needed.

The materials chosen can also be divided into two categories: the first includes elemental materials such as silicon or gold, and the second consists of oxides and nitrides, for which existing databases are very sparse and for which large deviations are expected to exist in the values calculated with semiempirical interpolative schemes. The energies at which the stopping power values were measured correspond, in all cases, to the energy range commonly used in actual experiments.

1.4. STRUCTURE

This publication starts with an introductory section on stopping power. Basic concepts and definitions related to energy loss of a beam of ions in matter are first established, followed by a presentation of the concepts and models behind stopping power theory. Links to available resources on stopping powers are then given and include databases of experimental values and computer programs that calculate stopping powers in the energy range useful for IBA. Finally, a review of experimental methods for the determination of stopping powers is made. Section 3 presents the laboratories that participated in the experiments, including detailed descriptions of the set-ups and experimental conditions used. A key issue in the experimental determination of stopping power is the availability of adequate targets. Thus, Section 4 is dedicated to the manufacture and procurement of the targets used in the experiments. In Section 5, the methods to calculate the uncertainties associated with the different measurements are

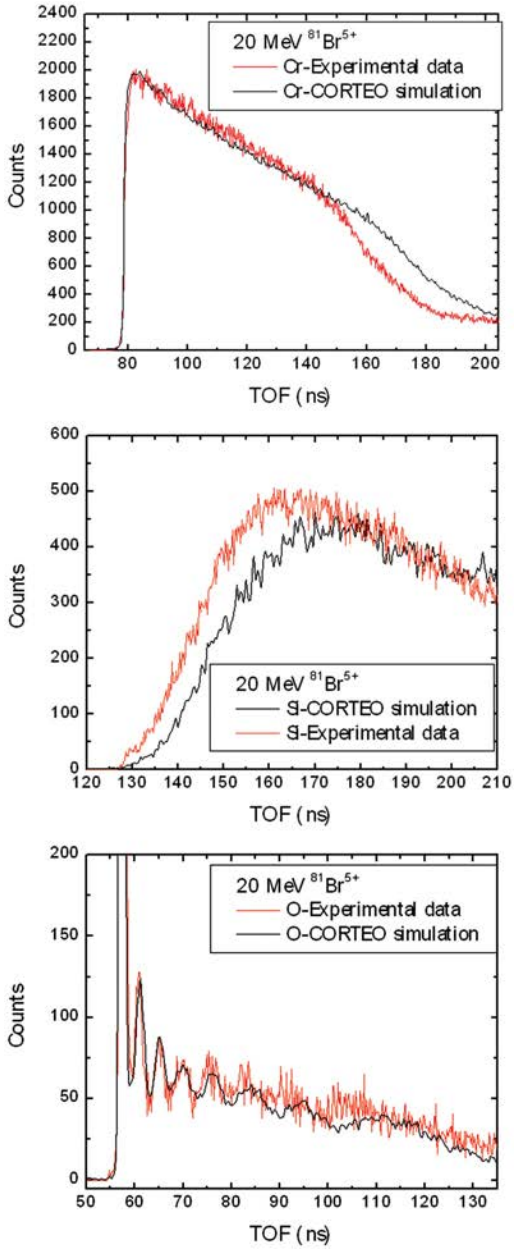

FIG. 1. Time of flight–E–elastic recoil detection analysis spectra of the National Institute of Standards and Technology standard reference material 2136 measured with 20 MeV ^{81}Br ions. The chromium, silicon and oxygen recoil spectra are shown. (Reproduced courtesy of the Ruđer Bošković Institute, Croatia.)

TABLE 1. IONS USED, ENERGIES, TARGETS AND METHODS FOR THE STOPPING POWER MEASUREMENTS PERFORMED IN THE COORDINATED RESEARCH PROJECT

Ion	Energy (MeV)	Target	Method (bulk or transmission)	Group[a]
^{4}He	1–2.4	a-Si, TiO_2, GaN, InN	Bulk	Lisbon
^{7}Li	1–3	a-Si	Bulk	Lisbon, RBI
^{11}B	1–2.5	a-Si, TiO_2	Bulk	Lisbon, RBI
^{12}C	3–15	a-Si, TiO_2, GaN, InN	Bulk	Lisbon, RBI
^{16}O	3–15	TiO_2, GaN, InN	Bulk	Lisbon, RBI
^{12}C	3–15	Ta_2O_5	Bulk	Lisbon, RBI
^{16}O	3–15	Ta_2O_5	Bulk	Lisbon, RBI
^{35}Cl	6–27	Ta_2O_5	Bulk	Lisbon, RBI
^{12}C	1.2–6	Al_2O_3, Si_3N_4, SiO_2, ZrO_2, Mylar	Transmission	iThemba LABS
^{16}O	1.6–8	Al_2O_3, Si_3N_4, ZrO_2, Mylar	Transmission	iThemba LABS
^{19}F	2–12	ZrO_2, Mylar	Transmission	iThemba LABS
^{24}Mg	3–12	ZrO_2, Mylar	Transmission	iThemba LABS
^{27}Al	3–12	ZrO_2	Transmission	iThemba LABS
^{28}Si	2.8–14	Al_2O_3, Si_3N_4, SiO_2, Mylar	Transmission	iThemba LABS
^{197}Au	80, 120	C, Al, Ni, Au	Transmission	Munich
^{127}I	60, 170	C, Al, Ni, Au	Transmission	Munich
^{58}Ni	40, 60	C, Al, Ni, Au	Transmission	Munich

TABLE 1. IONS USED, ENERGIES, TARGETS AND METHODS FOR THE STOPPING POWER MEASUREMENTS PERFORMED IN THE COORDINATED RESEARCH PROJECT (cont.)

Ion	Energy (MeV)	Target	Method (bulk or transmission)	Group[a]
^{197}Au	40	C, O, Al, Si, Hf	Transmission	Munich
^{63}Cu	40	C, O, Al, Si, Hf	Transmission	Munich
^{127}I	170	O, Si, Hf	Transmission	Munich
^{58}Ni	60	Si_3N_4, Al_2O_3, Ta_2O_5	Transmission	Munich
^{79}Br	40	Si_3N_4, Al_2O_3, Ta_2O_5	Transmission	Munich
^{35}Cl	35	Si_3N_4, Al_2O_3, Ta_2O_5	Transmission	Munich
^{12}C	0.5–14	Si_3N_4, Al_2O_3, Ta_2O_5	Transmission	Helsinki
^{16}O	0.5–14	Si_3N_4, Al_2O_3, Ta_2O_5	Transmission	Helsinki
^{35}Cl	0.8–20	Si_3N_4, Al_2O_3, Ta_2O_5	Transmission	Helsinki
^{79}Br	6.0–40	Si_3N_4, Al_2O_3, Ta_2O_5	Transmission	Helsinki
^{127}I	14–37	Si_3N_4, Al_2O_3, Ta_2O_5	Transmission	Helsinki
^{12}C	0.2–8.5	Si_3N_4, Al_2O_3	Transmission	Jyväskylä
^{16}O	0.25–8.0	Si_3N_4	Transmission	Jyväskylä
^{35}Cl	0.5–10.9	Si_3N_4, Al_2O_3	Transmission	Jyväskylä

Note: LABS — Laboratory for Accelerator Based Sciences; RBI — Ruđer Bošković Institute.
[a] Details provided in Table 2.

TABLE 2. PARTICIPATING LABORATORIES

Institution	Participants	Equipment used	Technique
University of Helsinki, Finland, Department of Physics, Division of Materials Physics	Jyrki Räisänen, Kenichiro Mizohata, Emma Härkönen, Mikko Ritala	5 MV tandem accelerator	Transmission with TOF detection, continuous energy range, fitting data analysis method
Instituto Superior Técnico/ University of Lisbon, Portugal	Nuno Pessoa Barradas, Eduardo Alves	2.5 MV Van de Graaff accelerator	Backscattering, Bayesian inference fitting data analysis
Ruđer Bošković Institute, Croatia, Laboratory for Ion Beam Interactions, Division of Experimental Physics	Zdravko Siketić, Iva Bogdanović Radović, Natko Skukan, Milko Jakšić	6 MV EN tandem accelerator	Backscattering, Bayesian inference fitting data analysis
University of Jyväskylä, Finland, Department of Physics, Accelerator Laboratory	Timo Sajavaara, Mikko Laitinen, Jaakko Julin, Jouni Heiskanen, Kai Arstila	Pelletron 1.7 MV tandem accelerator	Transmission with TOF detection
iThemba Laboratory for Accelerator Based Sciences (LABS), South Africa	Mandla Msimanga, Carlos Pineda-Vargas, Craig Comrie	6 MV tandem accelerator	Transmission with TOF detection, continuous energy range
Universität der Bundeswehr München, Germany, Institute for Applied Physics and Metrology — LRT2	Günther Dollinger, Andreas Bergmaier	15 MV tandem accelerator	Transmission with Q3D magnetic spectrograph

explained, and representative examples are given for all experimental set-ups and methods employed by the participating laboratories. Sections 6–8 report the experimental results obtained. Section 6 is dedicated to the stopping power values determined, corresponding to 15 ions and 16 target materials, a total of 89 ion–target combinations. Sections 7 and 8 are shorter and report energy loss straggling and electron screening experimental data, respectively. Section 9 reports on improved modelling capabilities that also resulted from this work. The conclusions are presented in Section 10. The stopping power data are included in tabulated form in the Appendix.

2. STOPPING POWER — DATA, MODELS AND METHODS

2.1. CONCEPTS, DEFINITIONS AND UNITS

2.1.1. Energy loss

The literature has differing definitions of stopping power and other concepts related to the energy loss of a particle beam crossing matter. The definitions adopted here will follow those given in the chapter on energy loss and energy straggling in the second edition of the Handbook of Modern Ion Beam Analysis [7]. However, the reader is referred to the convincing argument made by Sigmund that the energy loss per path length should be called 'stopping force' and not 'stopping power' [8].

Figure 2 should be considered. A monoenergetic beam of particles with atomic number Z_1 and mass number M_1, with initial energy E_0, crosses a monoelemental thin foil of thickness Δx and areal density Nt, composed of an element with atomic number Z_2 and mass M_2. The transmitted beam has energy $E_f = E_0 - \Delta E$, where ΔE is the energy loss of the beam crossing the foil.

The stopping power of the medium, S, is defined as the energy loss per path length:

$$S \equiv -\frac{dE}{dx} = -\lim_{\Delta x \to 0} \Delta E/\Delta x \tag{1}$$

The stopping power is, thus, a property of the medium; the energy loss is a property of the beam. The correct terminology should state the stopping power of a given element (or compound) for a given ion species or, alternatively, the stopping power for a given ion in a given element (or compound).

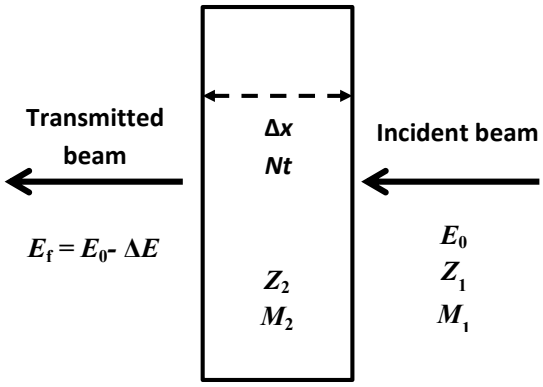

FIG. 2. Basic stopping power concepts.

The units of the stopping power, S, are, for instance, eV/nm or MeV/μm. S is also called the linear stopping power. The mass stopping power, with units such as MeV/(mg/cm^2), is defined as the ratio between the linear stopping power and the density, ρ, of the material:

$$S/\rho \equiv -\frac{1}{\rho}\frac{\mathrm{d}E}{\mathrm{d}x} = -\frac{1}{\rho}S \tag{2}$$

Most IBA techniques, such as ERDA or Rutherford backscattering spectroscopy (RBS), are not sensitive to actual thickness or depth, but to areal density or, in other words, to the amount of matter crossed, which is commonly given in units of at./cm^2 (where 'at.' stands for number of atoms, a convention universally used among IBA practitioners), μg/cm^2 or mg/cm^2. Thus, the stopping cross-section, ε, is often the most useful quantity:

$$\varepsilon \equiv -\frac{1}{N}\frac{\mathrm{d}E}{\mathrm{d}x} = -\frac{1}{N}S \tag{3}$$

where N is the atomic number surface density of the medium.

The stopping cross-section is, like the stopping power, a property of the medium. Commonly used units are, for instance, eV/(10^{15} at./cm^2), eV/(μg/cm^2) or keV/(mg/cm^2).

2.1.2. Straggling

As a beam of particles crosses a material, each ion undergoes a different number of collisions and follows a slightly different path. After crossing a certain

thickness, an initially monoenergetic beam has a certain energy distribution. The energy loss defined above is the average of this energy distribution (sometimes the median or the most probable energy loss is taken).

This phenomenon of the spreading of the energy distribution of the beam is called 'straggling'. It has several origins. The statistical fluctuations in the number of collisions lead to so-called energy loss straggling. Multiple scattering — that is, the combined effect of very many small angle scattering events — leads to a change in the angular distribution of the beam, which contributes to an increase in its energy distribution. Geometric straggling includes the effects of a finite sized beam, beam spot and detector. Other effects can be important in special circumstances [9].

Energy straggling results in the depth resolution degrading with depth. The result is a broadening of any interface signals in the spectra obtained and a distortion of the spectral shape. Any interface, intermixing and diffusion studies with RBS or ERDA (or other IBA techniques) must take energy straggling into account as accurately as possible, or the results will be incorrect.

State of the art calculations of depth resolution as a function of depth are made by the computer code DEPTH [9], which is based on the models developed by Amsel et al. [10]. The databases for straggling are, however, much sparser and less accurate than for stopping power. The theoretical models are, therefore, more difficult to test against data, and no statistical analysis of their accuracy has been presented so far.

2.2. CONCEPTS AND MODELS: A SHORT INTRODUCTION

Ziegler et al. presented an excellent historical summary of the first 75 years of research on the stopping of energetic ions in matter [11]. New developments since then have not changed the basic concepts, and the essential problems of stopping theory have been present since the seminal work by Bohr [12]. International Commission on Radiation Units and Measurements Report 73 [13] presented a critical survey on measurements and calculations of stopping powers for heavy ions, following International Commission on Radiation Units and Measurements Report 49 [14] for protons and alpha particles.

A detailed study on the theory and physical models of stopping power is outside the scope of this publication. The interested reader is referred to the chapter on energy loss in the Handbook of Modern Ion Beam Analysis [7] and the references therein as a starting point, or to Ref. [11] and the references therein for a more detailed view.

Energy loss is caused by electrostatic interactions of the moving ion with the nuclei and electrons of the target, and stopping power is usually taken to be

the sum of two independent contributions: (1) electronic stopping arising from inelastic collisions that lead to excitation and ionization and (2) nuclear stopping arising from elastic collisions between two screened nuclei. In terms of the stopping cross-section, stopping power can be written as $\varepsilon = \varepsilon_n + \varepsilon_e$, where ε_n and ε_e are the nuclear and electronic stopping cross-sections, respectively. This ignores correlations between the two sets of phenomena, which are important in single collisions but are averaged over many collisions.

As can be seen in Fig. 3, there are different regimes of stopping power behaviour, depending on the ion velocity compared with the Bohr velocity, v_0, which is the velocity of an electron in the ground state orbit of the hydrogen atom:

$$v_0 = e^2/\hbar \tag{4}$$

where e is the electron charge and ħ is the reduced Planck constant.

For ion velocities with v much larger than the Bohr velocity, $v >> v_0$, the ion becomes fully stripped. The problem is to describe a moving particle with charge Z_1e that interacts elastically with the free electrons of the target and inelastically with its bound electrons. The quantum mechanical relativistic Bethe–Bloch model, developed in the 1930s, predicts that the stopping power is

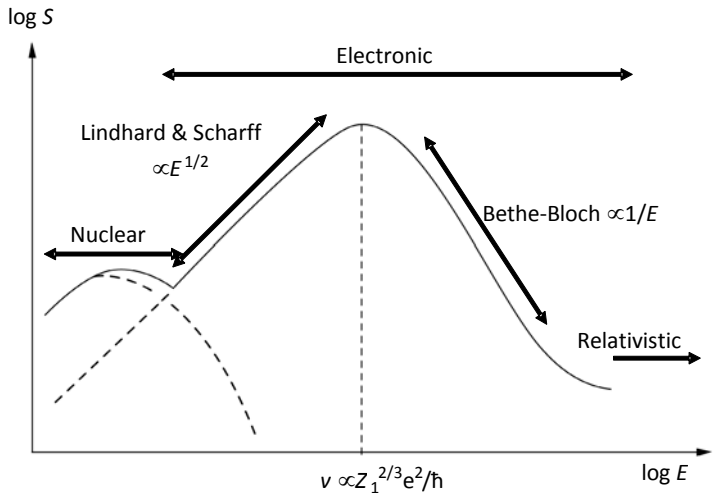

FIG. 3. Schematic representation of the variation of stopping power with ion energy [7].

inversely proportional to the square of the ion velocity and, for a given velocity, is proportional to the square of the ion charge, according to the Bethe formula [7]:

$$S = NZ_2 4\pi L\left(Z_1 e^2\right)^2 \Big/ m_e v \tag{5}$$

where m_e is the electron mass and L is the stopping number, which depends on the mean excitation potential of the electrons in the target and on the ion velocity.

As the ion velocity decreases, its effective charge also decreases as it captures electrons. The stopping power initially increases less rapidly with decreasing energy, before reaching a maximum and then starting to decrease. The stopping power maximum, often called the Bragg peak [7], is usually found close to the Thomas–Fermi velocity $Z_1^{2/3} v_0$.

Semiempirical models use a fractional effective charge of the partially stripped ion, defined as $Z_1^* = \gamma Z_1$, where γ depends on the ion velocity and ion species. Through the use of this fractional effective charge, the Bethe formula can be used in this intermediate velocity regime near the stopping power maximum. The same effective charge concept is used in semiempirical models to obtain the stopping power of heavy ions by scaling it to the stopping power of protons at the same velocity.

At low ion velocities, from around $0.1 v_0$ to around $Z_1^{2/3} v_0$, the Bethe–Bloch model breaks down as the inner shell target electrons no longer contribute to the energy loss and the probability of the neutralization of the projectile increases. The theory of Lindhard et al., developed in the 1950s and 1960s [7], is based on elastic scattering of the free target electrons by the screened projectile, and it predicts that the stopping power is approximately proportional to ion velocity.

At very low velocities, energy loss via energy transfer to the target nuclei — that is, nuclear stopping power — starts to dominate and becomes the largest contribution to the total stopping power. This is particularly important for heavy ion projectiles because the relative contribution of nuclear stopping to the total stopping increases with the mass of the ion. Ziegler et al. presented an analytical expression for the nuclear stopping power of any material for any ion, derived from the Ziegler, Biersack and Littmark (ZBL) universal interatomic potential [11].

Other effects are treated in the literature, such as shell [15], Barkas [16], Bloch–Sørensen [17] and Fermi density effect [14] corrections. It is stressed that even the most sophisticated theories and models do not calculate, from first principles, the stopping power of any target material for any ion at any velocity with the same accuracy, on average, as semiempirical models such as SRIM. In IBA data analysis, the semiempirical formulations of stopping powers are almost always used.

To calculate the stopping power of a compound, the Bragg rule is usually employed. The compound stopping power is taken as the weighted average of the elemental stopping powers. There are strong deviations between experiments and stopping powers obtained this way, around 10–20% near the Bragg peak for solid compounds of light and heavy elements, such as oxides and nitrides, and light organic gases. For some given compound materials, SRIM includes a correction to the Bragg rule.

Nevertheless, as there are fewer measurements of the stopping power of compounds than that of elemental materials, the Bragg rule is almost universally used in IBA data analysis. In fact, IBA data analysis codes have not, until now, had the capability of using molecular stopping powers. A clear improvement is the capability to use experimental tabulated stopping power values for known compounds in data analysis codes, and one of the outcomes of this work was that one such code, NDF [18], now includes that capability.

2.3. SOFTWARE AND DATABASES OF STOPPING POWERS

2.3.1. Experimental data

The literature on experimental stopping power data, including the range of ions in matter, is vast. The literature starts in the 1910s, but the majority of work dates from the 1980s and later, when IBA techniques became established as standard analytical techniques. Many datasets were only published in graphical form, and some of them were published in papers whose main subject was not stopping power. It is difficult to find the stopping power of a given ion of a given material only by searching the literature.

Ziegler et al. (see Ref. [19] and references therein) has collected many datasets and included them in the SRIM database. The data are not given in numerical form, but plots are shown on the SRIM web site[5] with references to the original publications.

Paul has also collected a large database of experimental stopping power values, first published in the work of Paul and Schinner [20, 21]. The database has fewer datasets than SRIM, particularly for protons and alpha particles, but all of the data are given numerically and can, therefore, be directly used by other researchers. The data are available from the web site of the IAEA Nuclear Data Section[6], which started to maintain and develop the original database of Paul in 2015.

---

[5] www.srim.org

[6] www-nds.iaea.org/stopping/

2.3.2. Computer programs

Many computer programs calculate stopping powers in the energy range useful for IBA. Several of them are freely available (under specific conditions of usage) [7] and some of them are listed in Table 3. Some are based on first principles; others are semiempirical and rely on the experimental data to produce an interpolative scheme that can calculate the stopping power of any material for any ion, even for ion–target combinations for which no experimental data are available.

The most widely used software is SRIM. Its calculations and models have changed over time and are sometimes updated. Users are, thus, advised to download the latest version from the SRIM web site. SRIM is used by new generation data analysis codes such as SIMNRA [26] and NDF [18]. NDF can also use other software, such as MSTAR [20], or experimental tabulated data [27], including for elements and for compounds, avoiding the need to use the Bragg rule when a given compound is known to be present.

2.3.3. Accuracy of stopping power software

Paul and Schinner have extensively studied, using statistical methods, the reliability of stopping power tables and programs. This included protons and alpha particle beams, heavy ions, and elemental and compound materials (see Ref. [5] and the references therein). Their very careful and extensive published

TABLE 3. SOME AVAILABLE PROGRAMS FOR THE CALCULATION OF STOPPING POWER

Program	Web site	Main source
SRIM	www.srim.org	[11, 19]
ASTAR	www.nist.gov/pml/data/star/index.cfm	[14]
PSTAR	www.nist.gov/pml/data/star/index.cfm	[14]
MSTAR	www-nds.iaea.org/stopping/	[20, 21]
ATIMA	www-linux.gsi.de/~weick/atima/	[22]
CASP	www.casp-program.org	[23]
GEANT4	geant4.web.cern.ch/geant4/	[24, 25]

work also provides the reliability of the stopping power of a given material for a given ion in each energy range.

Their main conclusion has been that, on the whole, SRIM describes the experimental data as well as, or better than, any other software. For the ion–target combinations for which it is available, MSTAR is at least as good as SRIM and can even be better in some cases.

For protons and alpha beams, the average accuracy of SRIM was found to be around 6–7% for solids and 3–4% for gaseous targets. This was in the entire energy range for which measurements are available, including very low energies for which experiments are difficult. Considering only the typical energy range of interest for IBA, the average accuracy of SRIM was found to be better, for instance, 3% for ^{4}He in the 1–10 MeV/nucleon range [5]. For heavier ions, the accuracy is somewhat worse. For instance, for ions with a Z_2 between 19 and 92 in solid compounds, the average accuracy was found to be 10.7% [5].

The SRIM web site includes stated accuracy values for the stopping power for hydrogen, helium, lithium and heavier ions. These values are shown in Table 4 for elemental solid targets. This is not the same analysis as conducted by Paul [5], as it is based on a different dataset and the numbers can vary slightly. Furthermore, the accuracy values presented by Paul are calculated standard deviations, whereas the values presented by Ziegler [11, 19] are the average of individual absolute deviations.

In addition to the average accuracy values, the number of data points that match the SRIM calculation within 5% and within 10% are given. Considering, for example, the stopping power for hydrogen ions, the average accuracy is 4%, but 26% of all data deviate from SRIM by more than 5%, and 13% deviate by more than 10%. As a result, the actual accuracy of SRIM is, in some cases, much worse than the average accuracy stated.

For compounds, the accuracy is worse, also because the Bragg rule is often assumed, and large deviations (commonly 10–20%) near the stopping power maximum are often observed in insulating compounds, particularly in oxides and nitrides of heavy elements.

The SRIM database is very sparse for ions heavier than lithium. In fact, for the 89 ions from berylium to uranium, only about as many measurements exist altogether as do for hydrogen. For many ion–target combinations, no data are available, and the SRIM calculations are then a pure interpolation, informed only by data for other systems. This lack of experimental data is certainly one of the reasons for the poorer accuracy of the calculation of stopping powers for heavy ions.

TABLE 4. ACCURACY OF SRIM-2010 CALCULATION OF STOPPING POWERS OF ELEMENTAL SOLID TARGETS

Ion	Number of data points in database	Average accuracy (%)	Data points within 5% (%)	Data points within 10% (%)
Hydrogen	8 300	4.0	74	87
Helium	6 500	3.9	76	89
Lithium	1 400	4.8	72	83
Berylium–Uranium	9 000	5.8	58	82
All	25 200	4.6	69	86

2.4. EXPERIMENTAL METHODS FOR DETERMINATION OF STOPPING POWERS

Different methods for experimental determination of stopping powers have been presented in the literature. In particular, International Commission on Radiation Units and Measurements Report 49 [14] has a comprehensive and detailed description of experimental methods used until 1993.

The most obvious method is also the most widely used: measuring the energy of a beam of known initial energy after it crosses a thin film of known thickness of the material under study. The stopping power of the film material for the beam ion is the ratio between the energy loss in the film and the film thickness, for an energy taken to be the average energy of the beam in the film. Many refinements of this basic experiment are possible and have been developed and applied. The most important are outlined in the following subsections. Several of them have been used in the experiments reported in this publication.

Other methods to measure stopping powers have also been developed and applied and are reported in the literature. Some of these methods are also explained in the following subsections, and emphasis is placed on the bulk sample method because it was extensively used by two of the participating laboratories.

There are many variations of these and other methods, and the list presented is not exhaustive.

2.4.1. Transmission in thin films of a monoenergetic beam

In its simplest form, the measurement of stopping powers in a transmission method follows directly from Fig. 2, used in the definition of stopping power. The thin foil can be a multielemental compound, and in that case, it is the stopping power of the compound that is measured.

The foil thickness Δx has to be thin enough that the energy loss is very small compared with the initial beam energy. Ideally, the energy loss ΔE should be around or smaller than 1%. The stopping power is therefore:

$$S(E) = \frac{\Delta E}{\Delta x} \tag{6}$$

where E is normally taken as the average between the initial beam energy and the final energy after transmission:

$$E = E_0 - \Delta E/2 \tag{7}$$

For large energy losses, it is to be expected that the stopping power is not constant in the foil and that this approximation loses validity. This is the main reason the foil needs to be thin.

The sources of uncertainty include the uncertainty in the determination of the energy of the beam before and after transmission through the foil, which is normally obtained by fitting a Gaussian function to the beam energy profile, as well as the uncertainty in the energy calibration of the detection system. For multielemental foils, the actual composition of the foil is also an issue.

However, the largest source of uncertainty in this method is usually the thickness of the foil, which is directly reflected in the uncertainty of the final result. The thickness has to be known or determined by some other method. If that other method determines a thickness, then the density of the foil has to be known in order to obtain the stopping cross-section, which is the most useful quantity for IBA techniques. If an IBA method is used to determine the areal density of the foil, for instance using a different beam, then the uncertainty in the stopping power of the foil for that other beam is propagated to the uncertainty of the areal density determined and, thus, to the uncertainty of the stopping cross-section determined. Either way, it is difficult to produce such thin foils that are homogeneous in thickness. The foil thickness inhomogeneity is then a further source of uncertainty that is often not taken into account, which is one of the reasons that different stopping power measurements of the same material for the same ion very often disagree by much more than the respective stated uncertainties [28].

In the late 1980s, Mertens published a review on how to measure absolute stopping cross-sections by transmission methods [28], in which he described some effects that can affect the measurements, and how to minimize them by adopting careful procedures. Some further issues that he mentioned were sputtering of the foil material under the beam and foil contraction (whereby the thickness of the foil can increase in the region of the beam spot). Target texture effects can also occur in polycrystalline materials due to local channelling in microcrystalline regions. For small energy losses, outgassing is also an issue. Similarly to when a foil is introduced into a vacuum chamber and is analysed for the first time, an additional energy loss of up to 1 keV can be observed.

Finally, it is clear that, for a given beam energy, each experiment provides the stopping power at one energy only. In general, knowledge of the stopping power in a fairly large energy range is required, and the beam energy has to be changed to determine the stopping power for one energy value at a time. As the stopping power can change by a large factor over the energy range required, several foils, with different thickness values, may be required.

2.4.2. Transmission in thin films: Continuous range of energies

Trzaska et al. proposed in Ref. [29] and developed in Ref. [30] a new approach to energy loss measurements, whereby the stopping power could be determined over a large energy range in a single experiment. The set-up allowed the production of several incident ions simultaneously, thus enabling the stopping power of a given material for several ions to be obtained in a single experiment. Furthermore, several foils of the same material could be measured in the same run and by selecting different foil thicknesses, the overall reliability of the results could be improved.

A schematic diagram of a TOF energy set-up for the measurement of stopping powers in a continuous range of energies is shown in Fig. 4. A monoenergetic beam strikes a thick scatterer. The beam that is scattered towards the detection system has a wide energy spectrum, from zero to the maximum energy allowed by kinematics. The energy width of this spectrum is maximized by using a thick scatterer made of a high Z element, such as gold.

The energy spectrum of the forward scattered beam is measured by the energy detector, with and without the foil. The TOF $t_2 - t_1$ is also measured, in coincidence. A schematic representation of the expected results is shown in Fig. 5.

The energy measurement is often made with a surface barrier detector. Surface barrier detectors have a non-linear response caused by the pulse height defect, which comes from the detector dead layer and non-ionizing energy loss in the detector [31, 32]. This non-linear response leads to a non-linear calibration of

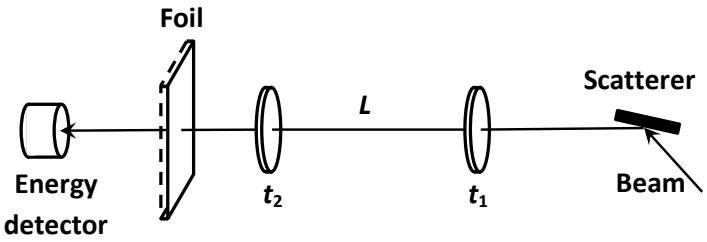

FIG. 4. Schematic diagram of a time of flight energy set-up for the measurement of stopping powers in a continuous range of energies.

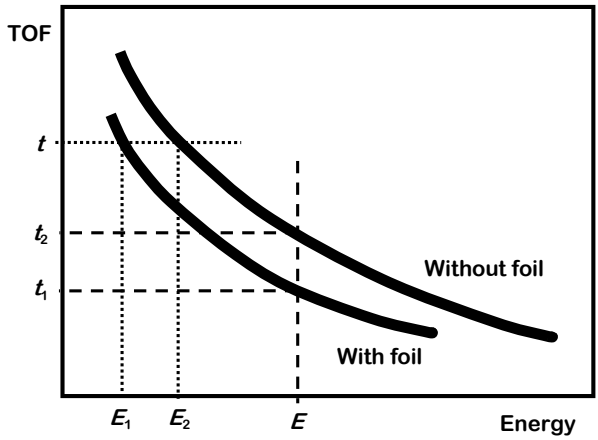

FIG. 5. A schematic representation of a typical time of flight versus energy plot, with and without the presence of the foil for which the stopping power is to be determined.

the energy channel. The TOF channel does not suffer from this problem and can be used to determine the energy:

$$E = \frac{m}{2}\left(\frac{d}{t}\right)^2 \tag{8}$$

where

m is the mass of the particle;
d is the flight length;

and t is the TOF.

Thus, the experiment without the foil is a direct calibration of the energy channel. In any case, the time channel almost always has a better resolution than the energy channel and is, therefore, normally used to also determine the energy.

A beam particle with initial energy corresponding to TOF, t, is now considered. Without the foil, the measurement in the energy channel is E_2, which matches t according to Eq. (8). With the foil, the measured energy is E_1, and the difference between E_1 and E_2 is the energy ΔE lost in the foil:

$$\Delta E = E_2 - E_1 \tag{9}$$

For a foil of thickness x, the stopping power of the foil material for the given beam is then:

$$S\left(E_{\mathrm{av}}\right) = \Delta E / t \tag{10}$$

where E_{av} is the average of the energy with and without the foil:

$$E_{\mathrm{av}} = \left(E_1 + E_2\right)/2 \tag{11}$$

One variation of this method is to take the TOF values t_1 and t_2 for a given detected energy E with and without foil. In this case:

$$\Delta E = E_2 - E_1 = \frac{m}{2}\left[\left(\frac{d}{t_2}\right)^2 - \left(\frac{d}{t_1}\right)^2\right] \tag{12}$$

With this method, the stopping cross-section is determined simultaneously for the entire energy range covered by the incident beam. Equation (8) or (12) is evaluated for all pairs, (E_1, E_2) or (t_1, t_2), respectively.

This is a transmission method, and the sources of uncertainty mentioned in Section 2.4.1 are also present. One further source of uncertainty is the calibration of the time channel, which is, however, often more accurate than the energy channel.

One unavoidable problem is that the same foil thickness is not ideal for the entire energy range, and for some beam energies, E_1 and E_2 can become so far apart from each other that the stopping cross-section cannot be considered to be almost constant inside the foil anymore. In this case, E_{av} is also only a crude representation of the energy at which the stopping cross-section is determined.

The timing detectors are often thin films crossed by the beam. In this case, the energy lost by the beam in the two films must be calculated, and this depends

on how well known the thickness of the films is, which is a further source of uncertainty. The pulse height defect in the films must also be taken into account.

2.4.3. Fitting of transmission data

One alternative method of analysing TOF transmission data to obtain a continuous range of energies is by using a fitting procedure. Equation (1) can be written in integral form to obtain a relationship between E_1 and E_2 and the stopping power:

$$\int_{E_1}^{E_2} \frac{\mathrm{d}E}{S(E)} = x \tag{13}$$

It is assumed that the thickness of the foil, x, is known, and that (E_1, E_2) pairs are determined experimentally as described above. The only unknown in Eq. (13) is, then, the stopping power, $S(E)$, which is varied in a fitting process until the best agreement with the data is obtained.

The stopping power curve, $S(E)$, can be parameterized, which has the advantage that a physically acceptable shape is obtained (i.e. one single maximum) and that only a limited number of fitting parameters is required. For instance, the ZBL parameterization with eight parameters a_1–a_8 [11], used in early formulations of SRIM, can be used:

$$S(E) = (SL \times SH) / (SL + SH) \tag{14}$$

where

$$SL = a_1 V^{a_2} + a_3 V^{a_4}$$

$$SH = \frac{a_5}{V^{a_6}} \ln\left(\frac{a_7}{V} + a_8 V\right)$$

$$V = \frac{E}{m}$$

The simpler parameterization proposed by Konac et al. [33] is also common:

$$S(E) = a_0 E^{a_1} \frac{1 + a_2 E}{1 + a_3 E + a_4 E^2} \tag{15}$$

Finally, a completely free form can be adopted for the stopping power curve that is fitted. This has the advantage that no a priori constraints are imposed on the shape of the stopping power curve. This can also be seen as a disadvantage, because unrealistic shapes of the stopping power curve may be derived — for instance, with more than one maximum or with inflexion points — that, according to current theoretical and experimental knowledge, should not exist.

2.4.4. Other implementations of the direct transmission method

Other implementations of the direct transmission method have been presented and used to measure stopping cross-sections. First, it is noted that the TOF can be replaced by a different detection system, such as a $\Delta E - E$ system or a Bragg ionization chamber [34]. The energy measurement with these systems is non-linear, and the accuracy obtained is normally lower.

Liguori Neto et al. [35] presented an alternative method that used only a surface barrier detector. The primary beam is scattered by a thick target made of a single heavy element. This secondary beam, having a broad energy spectrum, is detected with a particle detector in front of which the stopper foil can be introduced. The spectra $Y(E)$ and $Y'(E)$, without and with the stopper foil, respectively, are recorded. An ion of energy E, which, if it traverses the absorber foil, is detected with energy $E' = E - \Delta E$ should be considered. The objective is to, from $Y(E)$ and $Y'(E)$, identify pairs of E and E', to obtain the energy loss ΔE. The link between E and E' is given by the integrals of the spectra:

$$\int_{E}^{\infty} Y(E)\mathrm{d}E = \int_{E'}^{\infty} Y'(E)\mathrm{d}E \tag{16}$$

In practice, the upper integral limits can be placed just above the high energy edge of the spectra. By solving Eq. (16) for different values of E and obtaining the matching value E' in each case, a continuous curve is obtained. The accuracy depends on the accuracy of the fluence measurement (which does not need to be absolute; it can be relative), which can be made by placing a second particle detector from which a reference integrated yield can be used for normalization of the beam fluence in both cases. In comparison with the TOF coincidence tagging method described in Section 2.4.2, this method has the advantage of using a much simpler set-up (no coincidence or TOF telescope are needed), but it is also more sensitive to non-linearities in the energy detector.

To overcome the problems of self-supporting films, a workaround is sometimes used: the stopper material is deposited or attached directly to the energy detector [36]. If the detector is only partially covered and the incoming beam hits both the covered and the uncovered surfaces, some ions lose energy in the stopper, but others do not. A value for the energy loss is obtained by measuring

this energy difference. Again, the main difficulty usually arises from the precise determination of the thickness of the stopper as well as from non-linearities of the particle detector for heavy ions.

An enhancement of the basic direct transmission method has been proposed by Ribas et al. [37]. It consists of using a thin scatterer to produce a secondary ion beam of recoils that is used for the transmission experiment and simultaneously for the detection of the primary ions that produced the recoil. This is done by placing another detector at the appropriate scattering angle. In this way, the coincidence spectrum allows most of the background to be rejected and the energy of the recoils to be related before passing the stopper with the energy of the scattered ions.

A similar approach, for very low energies, has been introduced by Bergsmann et al. [38]. In this case, two TOF branches are used and the beam is chopped and alternately directed to each branch. One is used for a traditional transmission experiment; the other is used to continuously check the beam energy. This set-up reduces the effects of the beam energy fluctuations, which is particularly important when measuring very small energy losses (comparable to beam energy fluctuations), such as those of dilute gases.

2.4.5. Backscattering measurements from thin films

A thin film of the material to be studied is deposited on a bulk substrate, as in the resonance energy shift method. In this case, a standard RBS experiment is performed for a given beam energy. The energy width of the signal of one film element — that is, the difference in the energy of particles scattered off that element from the surface of the film and from the interface with the substrate — depends on the energy loss on the way in and on the way out. If the film is sufficiently thin, the mean energy approximation [39] can be used to calculate the energy for which the stopping cross-section is determined.

This method is similar to the transmission methods discussed above, in that it also uses the energy loss in a thin film. Figure 6 shows a simple schematic representation of the method. If the stopping power were constant throughout, the following would be obtained:

$$S(E) = \frac{E_1 - E_2}{x\left(\frac{K}{\sin\theta_1} + \frac{1}{\sin\theta_2}\right)} \tag{17}$$

where K is the kinematic factor [7].

However, this method can only be applied in such a straightforward way using Eq. (17) when the kinematic factor is high and, consequently, the energy of the beam is similar on the way in and on the way out [40]. In practice, Eq. (17) is not used directly, and different approaches are normally taken. One such approach is to perform the experiment shown in Fig. 6, at two different angles of incidence or detection (either tilting the sample or using two detectors simultaneously), and to use the surface energy approximation:

$$E_1 - E_2 = x\left(\frac{K\,S(E_0)}{\sin\theta_1} + \frac{S(KE_0)}{\sin\theta_2}\right) \tag{18}$$

With two different geometries, a system of two equations and two unknowns, $S(E_0)$ and $S(KE_0)$, is obtained.

Another approach is to measure the energy difference when only the outgoing path of the ions is changed. In this case, either two detectors are installed or two experiments are performed with the sample tilted symmetrically to either side with respect to the beam. This is usually called the symmetrical scattering signal shift method.

The experiment shown in Fig. 7 should be considered. The key is that the scattering angle is the same for both outgoing trajectories and, therefore, the energy at the beginning of these trajectories is exactly the same. However, since the beam direction is not normal to the surface, the length of the outgoing trajectories depends on their relative angles to the surface normal (θ_1, θ_2). The stopping power can be directly calculated as the quotient between the difference in energies and the difference in outgoing paths:

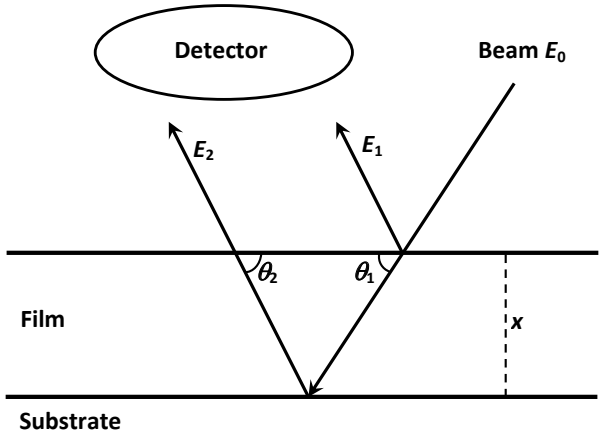

FIG. 6. Schematic representation of a simple backscattering experiment for determining the stopping power of a thin film.

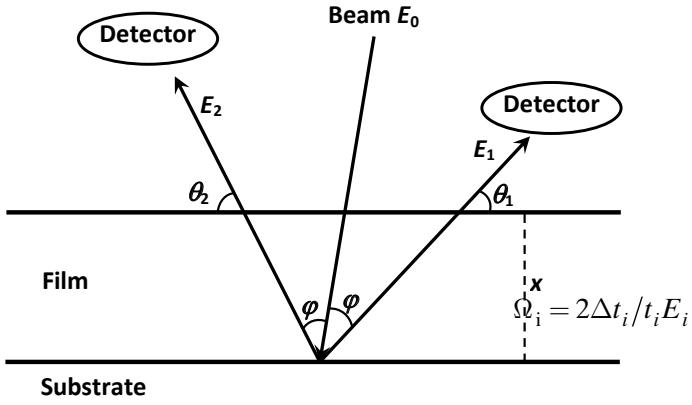

FIG. 7. Schematic representation of a backscattering experiment with detection at symmetrical scattering angles.

$$S\left(\overline{E}\right) = \frac{E_1 - E_2}{\left(\frac{1}{\sin\theta_1} - \frac{1}{\sin\theta_2}\right)} \tag{19}$$

where the stopping is evaluated at the average exit energy $\overline{E} = \left(E_1 + E_2\right)/2$.

2.4.6. Bulk sample method

Most experimental stopping power data have been obtained with the transmission methods described above. However, the results critically depend on the accurate characterization of the thin foils. The foils are not only difficult to procure with the required thickness and physical stability under the beam in a vacuum but often suffer from thickness inhomogeneity, pinholes and other structural problems. For instance, the foils must be amorphous in order to avoid accidental channelling. Furthermore, while it is relatively simple to measure foil thickness, in stopping experiments, it is necessary to know the areal density rather than the thickness, and conversion between the two quantities is often done by assuming bulk density for the foil.

One alternative to using thin foils is to measure the RBS spectra of bulk samples. The spectra depend on the sample, which is assumed to be known (a strong effort to characterize the sample's composition and impurity content may be needed); on the experimental conditions, which are known with given uncertainties; and on fundamental data such as stopping power or scattering cross-section. If everything else is known, the height and shape of the RBS spectra depend on the stopping power.

This is experimentally easy to do and avoids the problems associated with foils. However, in order to compare the experimental spectra with the expected spectra, assuming a given stopping power, the method requires an assumption that theoretical spectra can be calculated accurately.

Different variations of this method have been employed occasionally. Lennard et al. [41] used only the surface yield of bulk signals, for which simulations are less dependent on the capability to include physical models of phenomena such as plural and multiple scattering, or straggling. Lin et al. [42] used entire RBS energy spectra. In both cases, a fit was made using a parameterized stopping power. The method has also been used to measure stopping power in channelling conditions [43].

When RBS spectra are used beyond the surface energy, the height and shape of the data depend on the energy loss both on the way in and on the way out. That is, the yield depends on the stopping power at two different sets of energies. To remove the ambiguity, it is necessary to collect a set of several spectra for different initial beam energies. All the spectra must then be analysed in a self-consistent manner, that is, with the same energy dependent stopping power curve and with the same experimental parameters besides beam energy.

In a systematic approach to this method, the uncertainties of the experimental parameters must be taken into account to derive realistic uncertainties for the stopping power values determined. Bayesian inference with the Markov chain Monte Carlo (MCMC) method [44] is the method of choice. The mathematical formalism of Bayesian inference and of the MCMC method is beyond the scope of this publication. The actual procedure consists of treating the energy dependent stopping power curve as a free parameter, through the use of a parameterization such as those given in Eqs (14) or (15). Experimental parameters also vary, constrained to values within their uncertainties.

A series of simulations is generated, each for slightly different values of the experimental parameters and of the stopping power curve, but all of them consistent with the data, taking into account counting statistics. This series of simulations is in fact a Markov chain which, given well defined conditions, provides the stopping power curve together with its confidence limits, that is, its uncertainty.

This method depends on the quality of the theoretical simulations performed. It was implemented by Barradas et al. [18] in the standard code for IBA data analysis, NDF, a new generation code that includes advanced physical models of the most important effects that influence the yield and shape of RBS data [45]. The code analyses all the spectra simultaneously, with the same stopping curve, ensuring that a self-consistent solution is retrieved.

This method can be applied to any RBS spectrum, including from bulk samples, where the information is contained in the height and shape of the

spectrum. The method can also be applied to RBS spectra from thin samples, where the energy width of the signals can also be used if the film thickness is known. In this case, the traditionally used term ‘bulk sample method’ can be misleading, since thin films are used.

2.4.7. Other fitting methods

Niemann et al. [46] analysed, using RBS, samples with marker layers located at well known depths. The energy associated with the signal of each marker was recorded. Given known depth values, a parameterized stopping power was treated as a fit parameter to obtain agreement between the calculated and measured marker energy values. This method has the advantage that only energy loss need be calculated during the analysis and that the RBS spectra need not be simulated. Also, experimental parameters, such as beam fluence and detector solid angle, do not influence the results. However, this method requires very particular samples with appropriate markers that are often not available.

Pascual-Izarra et al. presented a refinement of this method that used a simulated annealing fitting algorithm, as well as a Bayesian inference procedure for the calculation of the uncertainties associated with the stopping power curves determined, and applied it to several systems [47, 48]. The method requires samples with marker layers or other appropriate features.

2.4.8. Resonance energy shift method

In this method, a known sharp resonance in the scattering cross-section of a given ion in a given element is used. A bulk substrate containing that element is used, and a thin film of the material to be studied is deposited onto that substrate. The resonance energy varies with or without the thin film; it is shifted to lower values with the thin film present. The difference is the energy lost by the beam in the film.

Besides the usual problems associated with using thin films, this method can only be used for specific beams at specific energies, where there is a resonance that can be used, and is, thus, limited in scope.

2.4.9. Inverted Doppler shift attenuation method

Doppler shift attenuation is a method used in nuclear physics to determine the lifetime of excited nuclear states, which emit a gamma ray with a characteristic energy on de-excitation. If the nucleus is moving, that energy is Doppler shifted, and the energy shift depends on the lifetime of the excited state and on the velocity of the nucleus. As the nucleus is slowing down in a material,

the Doppler shift will change. If the lifetime is known, the stopping power can be determined [49].

This inverted Doppler shift attenuation method is appropriate for many ion species in the energy range suitable for IBA because the lifetime of many known excited nuclear states matches the timescale in which ions with velocities normally found in IBA experiments slow down in materials.

The data analysis can be complex. The primary nuclear reaction that produces the excited nuclei often leads to the coexistence of many different excited states and these levels often decay into each other. Furthermore, the excited nuclei have a distribution of initial velocities and directions, which change further because of straggling. Monte Carlo methods have been proposed to deal with these issues [50], but the results obtained have been criticized for not always matching data from other sources [51].

In particular, the stopping powers determined depend on the lifetime of the excited states used. These lifetimes, however, have almost always been determined with Doppler shift attenuation by assuming a given stopping power of a given material for the species in question. The uncertainty of the stopping power used to determine the lifetime is then propagated to the accuracy of all stopping powers determined using inverted Doppler shift attenuation with that given lifetime.

3. PARTICIPATING LABORATORIES

3.1. UNIVERSITY OF HELSINKI, FINLAND

Division of Materials Physics,
Department of Physics,
University of Helsinki,
P.O. Box 43 (Pietari Kalmin katu 2),
00014 University of Helsinki, Finland
www.physics.helsinki.fi/tutkimus/mat/english/research/

The ion beam based activities of the University of Helsinki, Department of Physics, take place within two laboratories: the Ion Beam Analysis Laboratory and the Laboratory for Nanomaterials. The facilities incorporated and the research carried out therein are briefly described in the following subsections.

3.1.1. Ion Beam Analysis Laboratory

The Helsinki Ion Beam Analysis Laboratory centres its research activities on the interaction of energetic ions with solid matter, focusing, in particular, on the physical processes that take place during and after ion irradiation. These include:

— Interaction and energy loss of energetic ions in solids;
— Ion irradiation induced effects on the structure of matter;
— Interactions between defects, host atoms and implanted atoms;
— Diffusion and solubility of impurity atoms;
— Fabrication of novel materials;
— Analysis of implanted and irradiated materials.

The laboratory also houses experimental facilities for the IBA, modification and fabrication of materials, including:

— TAMIA, a 5 MV tandem accelerator, which is mainly used for:
    • Accelerator mass spectrometry;
    • ERDA;
    • In situ irradiation and positron annihilation spectroscopy or electrical characterization of materials at variable temperatures;
    • Rutherford backscattering.
— KIIA, a 500 kV implanter for:
    • Rutherford backscattering including channelling.
— A sputtering device for serial sectioning of radiotracer implanted diffusion samples.

3.1.2. Laboratory for Nanomaterials

The Laboratory for Nanomaterials employs cluster and ion beams in the modification, synthesis, characterization and functionalization of nanosystems and nanostructured materials. The following experimental techniques are available:

— Ion implantation;
— Cluster deposition — Facility for Nanostructures Deposition;
— Dual e-beam and ion sputter deposition system;
— Ion beam dry etching facility for nanostructuring and downsizing;
— Atomic force microscopy (AFM) or scanning tunnelling ion microscopy (STIM);
— Low energy electron diffraction;

— Auger electron spectroscopy;
— Low energy ion deposition (under development);
— Ultra-high vacuum variable temperature AFM or STIM;
— Cryogen-free dilution refrigerator system (~10 mK);
— Furnaces for sample annealing (up to 1500ºC);
— Equipment for terahertz spectroscopy.

The facility central to this project is the ERDA system, which is shown in Figs 8 and 9. The slightly modified set-up employed in the heavy ion stopping force measurements is shown in Fig. 9. The set-up houses a sample holder with positions for four samples, which is located before the energy detector.

3.1.3. Experimental conditions

This section details the experimental conditions used for the stopping power measurements made at the University of Helsinki.

Energy loss measurements were also conducted with alpha particles emitted by an ^{214}Am source. These results were used in deducing the prepared oxide film thicknesses. Thus, the extracted stopping force data are actually values relative to those of alpha particles (except for silicon nitride (Si_3N_4), for which the 100 nm thickness value provided by the manufacturer was employed). To calculate the sample film thicknesses from the measured alpha particle energy loss values, the Bragg rule and the SRIM stopping power values for the elemental targets were used.

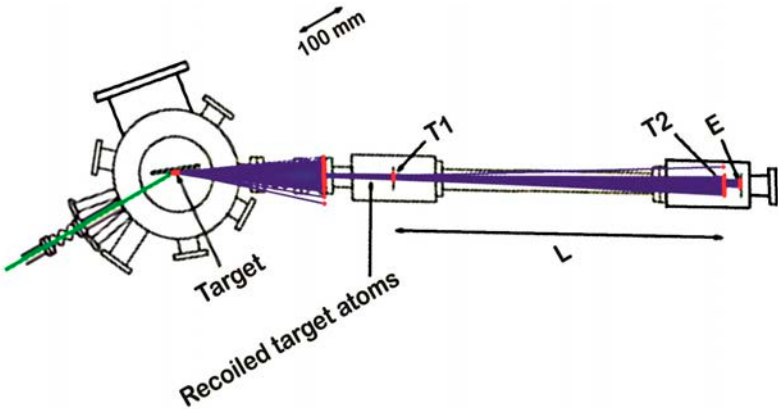

FIG. 8. Layout of the elastic recoil detection analysis facility at the University of Helsinki. (Reproduced courtesy of the University of Helsinki.)

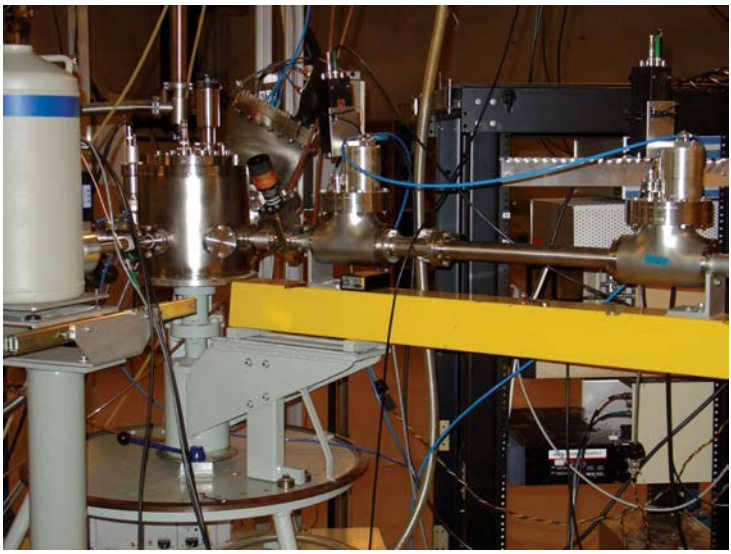

FIG. 9. Photograph of the University of Helsinki elastic recoil detection analysis facility, showing the time of flight arm. (Reproduced courtesy of the University of Helsinki.)

For the stopping power measurements, the TOF–ERDA set-up shown in Fig. 10 was used [52]. The timing gates were carbon foils, the flight length was 684 mm, and the energy detector was an Ortec Ultra series ion implanted detector. The sample foils were placed before the energy detector. The primary ions, produced in the 5 MV tandem accelerator TAMIA, were forward scattered by elemental bulk targets either of germanium or rhenium. The ions and their initial energies, together with the energy range actually probed and useful for the stopping power measurements, are given in Table 5.

The time calibration of the TOF detector was performed using a standard TOF–ERDA measurement of several bulk samples, namely silicon, C_2F_4, germanium, aluminium oxide (Al_2O_3) and cobalt, and by measuring the high energy edges of several recoils (carbon, oxygen, fluorine, aluminium, silicon, cobalt, germanium). The high energy edge of the time signal of different elements was determined, and a linear time calibration was fitted. Energy loss in the first timing gate was taken into account. The time resolution of TOF was 150 ps (full width at half maximum (FWHM)) for 5.2 MeV alpha particles from the ^{214}Am source.

The set-up housed a sample holder with positions for four samples. This made it possible to measure energy loss simultaneously for three samples and to calibrate the energy detector accurately from the same heavy ion ERDA spectrum by comparing the TOF signals and the energy signals obtained without a stopping

foil. In the procedure, energy loss in the carbon foil of the second timing gate was taken into account. The systems studied and the beam energies used are given in Table 1.

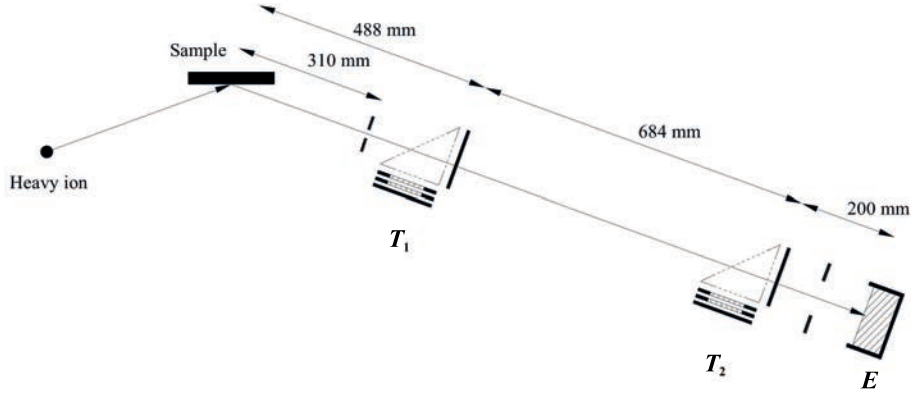

FIG. 10. Geometry employed in the time of flight–E–elastic recoil detection analysis stopping force measurements at the University of Helsinki. (Reproduced courtesy of the University of Helsinki.)

TABLE 5. PHYSICAL PARAMETERS RELATED TO THE STOPPING FORCE MEASUREMENTS AT THE UNIVERSITY OF HELSINKI

Ion	Initial ion energy (MeV)	Energy region for stopping values (MeV)
^{12}C	20	~0.8–18.2
^{16}O	20	~0.8–17.6
^{35}Cl	40	~1.4–36.5
^{79}Br	53	~3.5–43.0
^{127}I	53	~5.0–37.4

3.2. INSTITUTO SUPERIOR TÉCNICO, PORTUGAL

Instituto Superior Técnico/University of Lisbon,
Estrada Nacional 10,
2686-953 Sacavém, Portugal
c2tn.tecnico.ulisboa.pt

The ion beam based activities of the Instituto Superior Técnico take place in the Accelerator and Radiation Technologies Laboratory of the Instituto Superior Técnico Campus Tecnológico e Nuclear. The facilities incorporated and the research carried out therein are briefly described in the following.

3.2.1. Ion Beam Laboratory

The Ion Beam Laboratory is devoted to research and applications of ion beams in materials characterization and materials synthesis. The physical processes involved in IBA are also studied, with a strong effort in the experimental determination of stopping powers and scattering cross-sections. Several groups use the facilities available in different main areas of study, including:

— Materials science;
— Earth and environmental sciences;
— Cultural heritage;
— Life and health sciences;
— Nuclear physics;
— Materials for fusion.

The experimental facilities of the laboratory are schematically shown in Fig. 11 and include:

— A 2.5 MV Van de Graaff accelerator, which is mainly used for:
  - Rutherford backscattering;
  - ERDA;
  - Particle induced X ray emission (PIXE);
  - Particle induced gamma ray emission (PIGE);
  - Nuclear reaction analysis.
— An ion microprobe connected to the Van de Graaff accelerator, which includes:
  - A standard microbeam analysis chamber;
  - An external beam set-up.
— A 3 MV tandem accelerator, which is mainly used for:

- High resolution PIXE;
- Accelerator mass spectrometry.

— An X ray diffraction laboratory with several set-ups, including:
  - A high resolution line;
  - A high temperature set-up;
  - A commercial Brucker D-8 spectrometer.

All the experiments undertaken at the Instituto Superior Técnico for this publication were performed with a 'universal chamber' installed in one beamline of the Van de Graaff accelerator. This beamline had two experimental chambers. The one used is shown schematically in Fig. 12, and the inside of it is shown in Fig. 13.

The beam is defined by two collimators, located 2.15 m apart, leading to a low angular dispersion. The final collimator, which defines the beam shape, is rectangular with a height of 0.6 mm and a variable width, which in this work was fixed at 0.6 mm. The beam fluence is measured, to an accuracy of 2%, with a transmission Faraday cup that periodically intercepts the primary beam.

The chamber has three detectors, which can be used simultaneously. One is an annular detector around the beam, which has poor energy resolution. A movable detector is normally located at forward scattering angles and is used for ERDA experiments. The third detector was used in this work; it is located under the beam in the so-called Cornell geometry, at a 160º scattering angle.

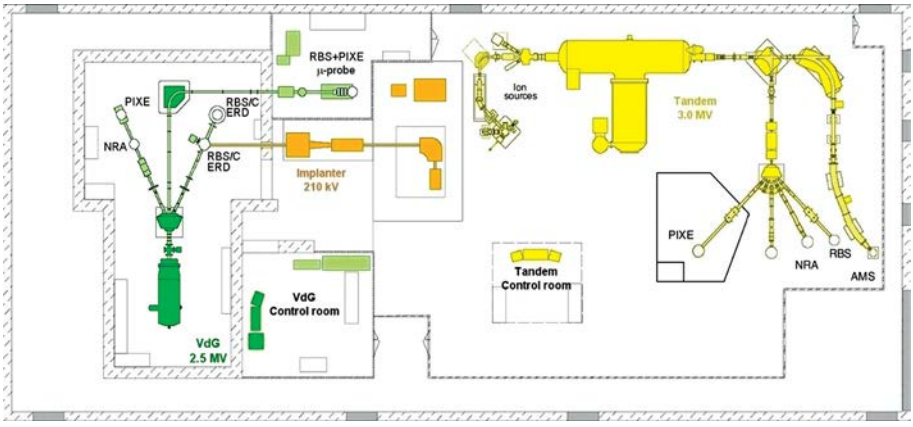

FIG. 11. Scheme of the ion beam experimental hall at the Instituto Superior Técnico. NRA — nuclear reaction analysis; C — channelling; VdG — Van de Graaff; AMS — accelerator mass spectrometry. (Reproduced courtesy of Laboratório de Aceleradores e Tecnologias de Radiação, Instituto Superior Técnico.)

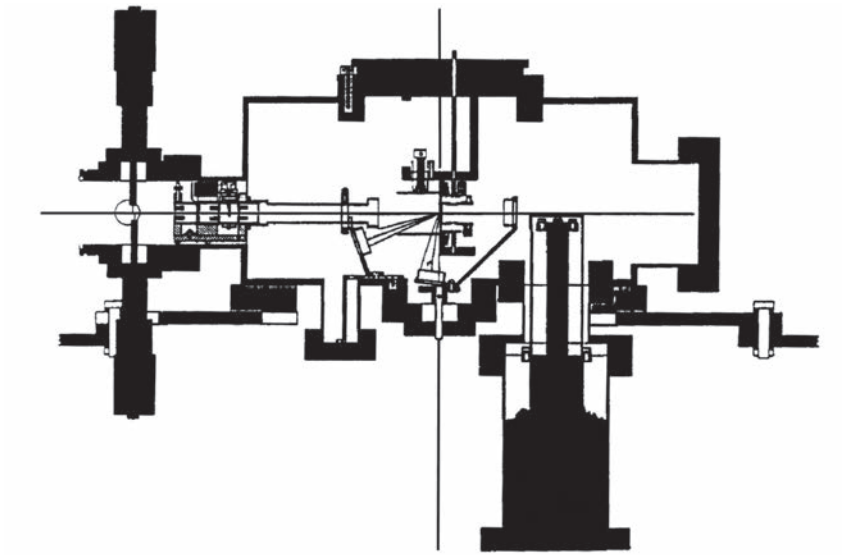

FIG. 12. Scheme of the Instituto Superior Técnico ion beam analysis universal chamber. (Reproduced courtesy of the Instituto Superior Técnico.)

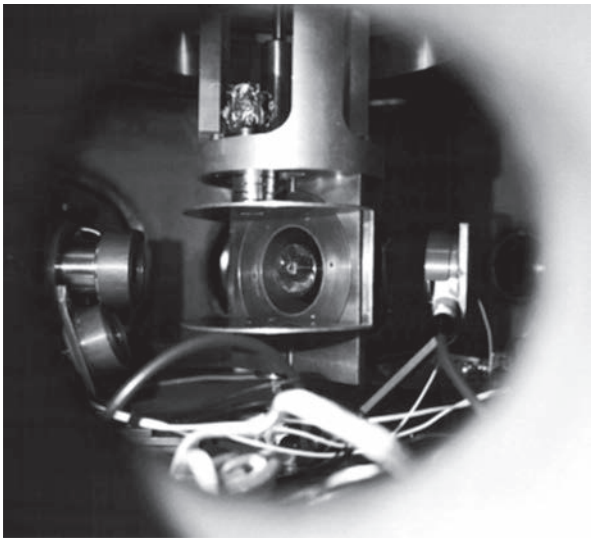

FIG. 13. Inside the Instituto Superior Técnico ion beam analysis universal chamber. (Reproduced courtesy of the Instituto Superior Técnico.)

The samples are inserted into the chamber without breaking the vacuum, leading to pressures below 10^{-7} mbar during experiments. The sample holder is connected to a two-axis goniometer, defining the angle of incidence with a precision of 0.02º.

3.2.2. Experimental conditions

All the stopping power measurements were made with a ^{4}He beam using the universal chamber shown in Fig. 12. The detector located at a 160º scattering angle was used for the data analysis. In experiments in which a new annular detector had been recently introduced and the energy resolution was acceptable, the annular detector was also used. After some months of intensive use (two to three shifts per day, five to seven days per week), the energy resolution of this detector degrades to levels not suitable for applications where accuracy is a foremost concern.

Experiments were undertaken in the range of beam energies that could be accessed by the Van de Graaff accelerator. For a given system, the electronics settings were not changed, so the energy calibration was the same for all the beam energies.

The experiments were made at a 7º angle of incidence, and during each experiment, the sample was continuously rotated to avoid accidental channelling.

The systems studied and the beam energies used are given in Table 1.

3.3. RUĐER BOŠKOVIĆ INSTITUTE, CROATIA

Laboratory for Ion Beam Interactions,
Division of Experimental Physics,
Ruđer Bošković Institute,
P.O. Box 180 (Bijenička 54)
10000 Zagreb, Croatia
www.irb.hr/eng/Research/Divisions-and-Centers/
Division-of-Experimental-Physics/Laboratory-for-ion-beam-interactions

The ion beam based activities of the Ruđer Bošković Institute take place in the Laboratory for Ion Beam Interactions. The facilities incorporated and the research carried out therein are briefly described in the following subsections.

3.3.1. Laboratory for Ion Beam Interactions

The accelerator centre operates two tandem accelerators and their associated experimental beamlines, this being the largest and most complex experimental facility in Croatia. Its purpose is to perform basic and interdisciplinary research based on the interaction of ion beams with matter, and to characterize and modify properties of matter, with an emphasis on nanostructure research. The research areas involve:

— Interaction and slowing down of energetic ions in solids (including measurements of non-Rutherford cross-sections, stopping powers and PIGE cross-sections);
— IBA methods (PIXE, PIGE, RBS, nuclear reaction analysis and STIM);
— Modification of materials using MeV ions;
— High energy ion implantation;
— Molecular imaging using heavy ions (MeV secondary ion mass spectrometry);
— Ion beam fabrication and ion beam induced charge characterization of silicon and diamond detectors.

Applications of IBA methods in biomedicine, the environment and research of cultural heritage objects is an important part of the work performed at the Ruđer Bošković Institute. The experimental facilities of the laboratory include (Fig. 14):

— A 6 MV tandem Van de Graaff accelerator with two ion sources (sputtering and alphatros) and the following beamlines:
    • Ion microprobe;
    • High resolution PIXE and high energy ion implantation beamline;
    • Nuclear reactions scattering chamber;
    • TOF–ERDA beamline;
    • IAEA beamline (PIXE/RBS/PIGE);
    • Channelling–RBS (dual beamline).
— A 1 MV Tandetron with a duoplasmatron ion source (sputtering source under installation):
    • External beam PIXE;
    • Scattering chamber for PIXE/PIGE/RBS for air pollution monitoring;
    • Line connected with a dual beamline.

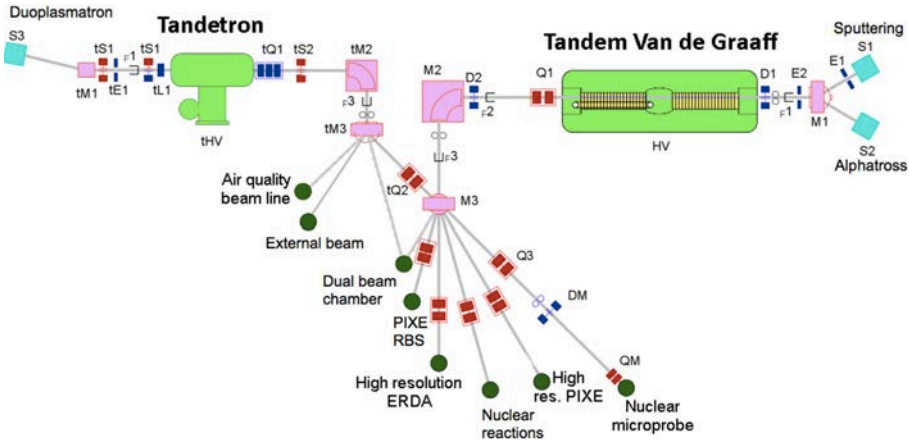

FIG. 14. Layout of the Ruđer Bošković Institute accelerator facility. (Reproduced courtesy of the Ruđer Bošković Institute.)

3.3.2. Experimental conditions

For the measurements undertaken in the framework of this project, the 6 MV tandem Van de Graaff accelerator and TOF–ERDA beamline were used (Fig. 15). The accelerator energy calibration was performed using the narrow 991.88 keV resonance in $^{27}Al(p, \gamma)^{28}Si$ and the neutron threshold reaction $^{7}Li(p, n)^{7}Be$ at 1880.6 keV.

The beamline used for the experiments is equipped with a TOF–ERDA spectrometer and with three particle detectors for RBS. These are located at backward angles of 118º, 150º and 165º. The experimental geometry is shown in Fig. 16. Stopping power measurements with the bulk sample method (see Section 2.4.6) were made with ^{7}Li, ^{11}B, ^{12}C, ^{16}O and ^{35}Cl ions. The systems studied and the beam energies used are given in Table 1.

3.4. UNIVERSITY OF JYVÄSKYLÄ, FINLAND

Accelerator Laboratory,
Department of Physics,
University of Jyväskylä,
P.O. Box 35 (Survontie 9),
40014 University of Jyväskylä, Finland
www.jyu.fi/accelerator/

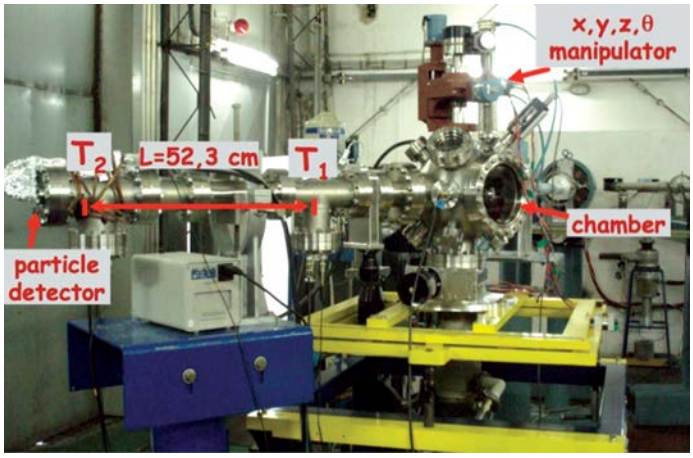

FIG. 15. Time of flight–E–elastic recoil detection analysis beamline at the Ruđer Bošković Institute. (Reproduced courtesy of the Ruđer Bošković Institute.)

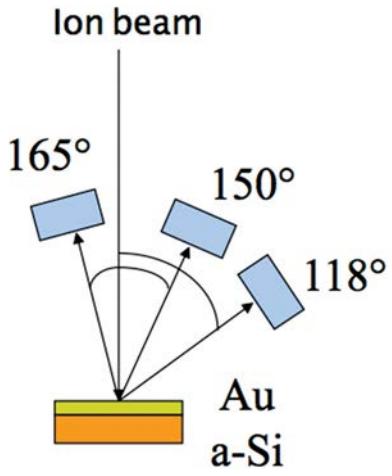

FIG. 16. Geometry employed at the Ruđer Bošković Institute in the stopping force measurements using thick targets. (Reproduced courtesy of the Ruđer Bošković Institute.)

The ion beam based activities of the University of Jyväskylä, Department of Physics, take place within the Accelerator Laboratory, which has one tandem accelerator (Pelletron) for materials research and two cyclotrons mainly for nuclear physics research. The facilities incorporated and the research carried out therein are briefly described in the following subsections.

3.4.1. Pelletron Laboratory

The areas of research within the Pelletron Laboratory are ion–matter interactions and their exploitation in IBA, ion beam modification and ion beam lithography. For IBA, the research focuses on the development of new high performance detectors, digitizing data acquisition systems and the development of IBA software. The ion beam modification focuses mainly on the fabrication of nano- and microsized ion tracks by means of energetic heavy ion beams from a cyclotron. Central to ion beam lithography is the fabrication of nano- and microfluidic high aspect ratio structures to polymers, quartz and glasses.

The experimental facilities of the laboratory (Fig. 17) include:

— A 1.7 MV Pelletron tandem accelerator with three ion sources (radiofrequency ion source for helium, sputtering ion source for heavy elements and multicusp ion source for high hydrogen currents), which is mainly used for:
  - Heavy ion ERDA;
  - Ion beam lithography using a programmable proximity aperture lithography set-up;
  - RBS;
  - PIXE;
  - Ion beam irradiation within the energy range of 0.2–15 MeV.
— A sputtering device for serial sectioning of radiotracer implanted diffusion samples (used for samples implanted at the IGISOL (Ion Guide Isotope Separation On-Line) facility).
— A scanning electron microscope.
— A 3D profilometer.

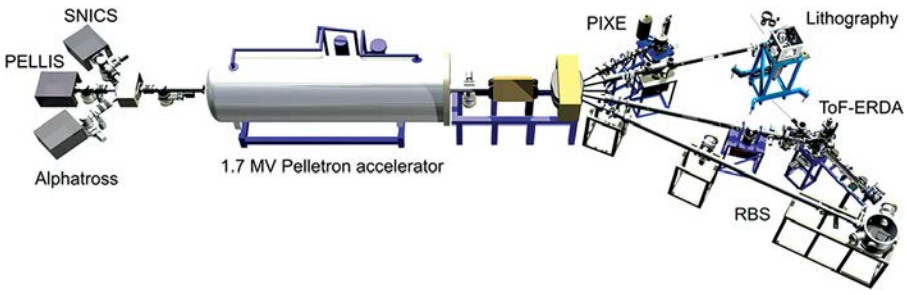

FIG. 17. Layout of the Jyväskylä Pelletron Laboratory. (Reproduced courtesy of the University of Jyväskylä.)

The key instrument constructed during this project is the TOF–ERDA set-up (Fig. 18). It can be used for depth profiling thin films down to a thickness of 5 nm or less and, with its gas ionization detector for energy measurement, even heavy masses at low energies down to 3–4 MeV can be separated from each other.

3.4.2. Experimental conditions

The 1.7 MV Pelletron was used. The end station was designed around a six axis goniometer. The detection system was a TOF–energy (TOF–E) telescope with good detection efficiency for hydrogen, higher than 90% for helium and higher than 99.5% for carbon, as shown in Fig. 19.

The timing resolution was measured for helium and hydrogen ions having energies of 4.8 MeV and 0.6 MeV, respectively, and scattered from a thin gold layer onto a silicon dioxide (SiO_2)–silicon wafer, as shown in Fig. 20. The timing resolution reached was 155 ps for helium (FWHM).

A gas ionization detector was built at the University of Jyväskylä and tested in measurements with low energy incident ions. The measured performance of this detector was superior in comparison with a silicon detector, and a good mass resolution could be obtained for a ^{35}Cl beam for energies as low as 3 MeV.

The data acquisition was realized in list mode, and a data stamp with an accuracy of 25 ns was given for each event. Coincident events were determined off-line.

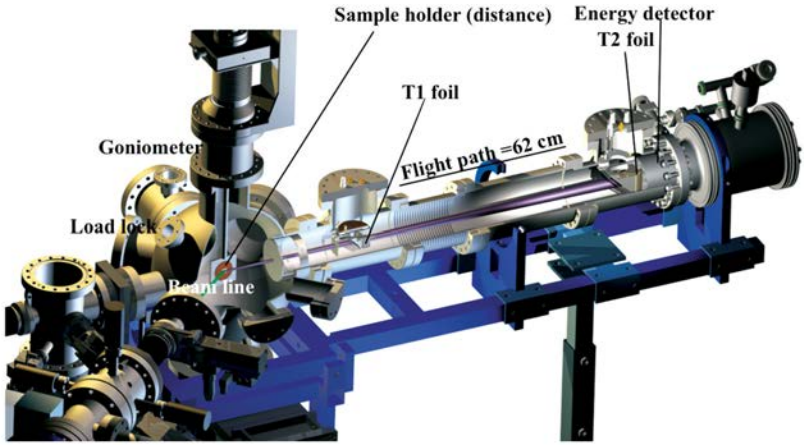

FIG. 18. Jyväskylä time of flight–E–elastic recoil detection analysis measurement set-up with a gas ionization detector installed for energy measurement. (Reproduced courtesy of the University of Jyväskylä.)

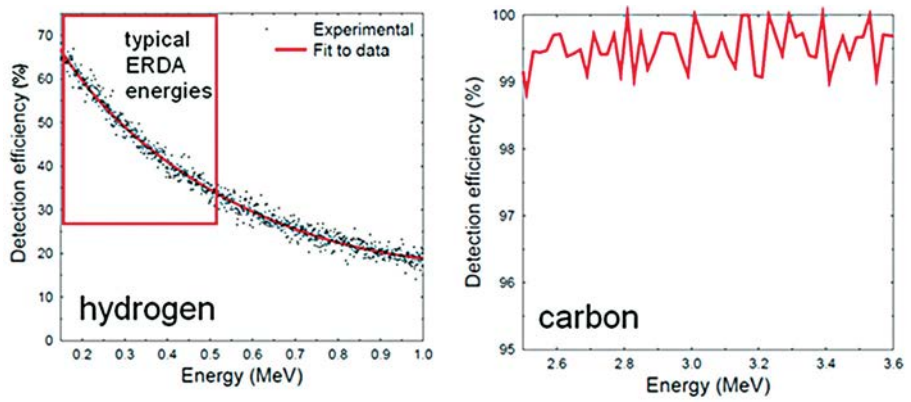

FIG. 19. Detection efficiency of the University of Jyväskylä time of flight detector with respect to the energy detector as a function of energy for hydrogen and carbon. The typical hydrogen energy region is marked for hydrogen. (Reproduced courtesy of the University of Jyväskylä.)

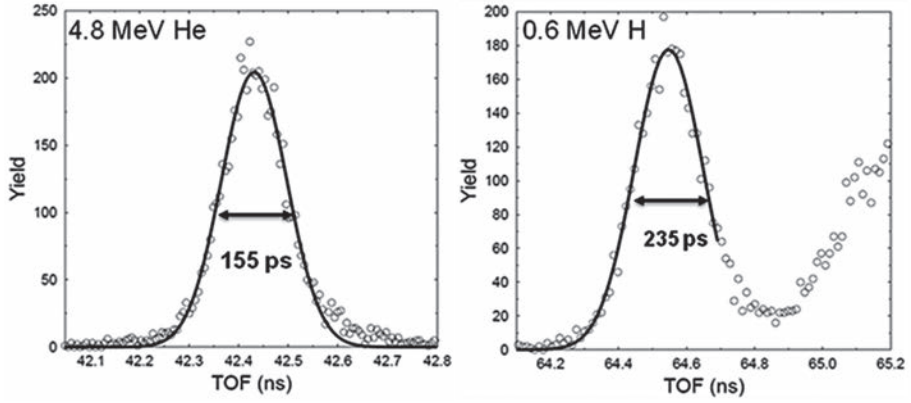

FIG. 20. Time of flight spectra for helium and hydrogen scattered from a thin gold layer. (Reproduced courtesy of the University of Jyväskylä.)

Stopping forces were measured by the transmission technique (see Section 2.4.1): the incident beam was scattered from a 1 nm gold layer onto a silicon substrate, and this scattered beam either went through the stopping medium under study or was scattered directly to the TOF–E telescope. A schematic view of the set-up is shown in Fig. 21 together with a photo of the sample holder containing both the gold scatterer and the Si_3N_4 membrane sample (see Section 4.1).

The energy spectra for scattered ions were calculated from the TOF spectra, which have a highly linear response for the entire energy range and the advantage

of leading to a much better energy resolution than if the signal of the energy detector were used. Examples of low energy ^{12}C and higher energy ^{35}Cl spectra, from which the energy loss was determined, are shown in Fig. 22. The systems studied and the beam energies used are given in Table 1.

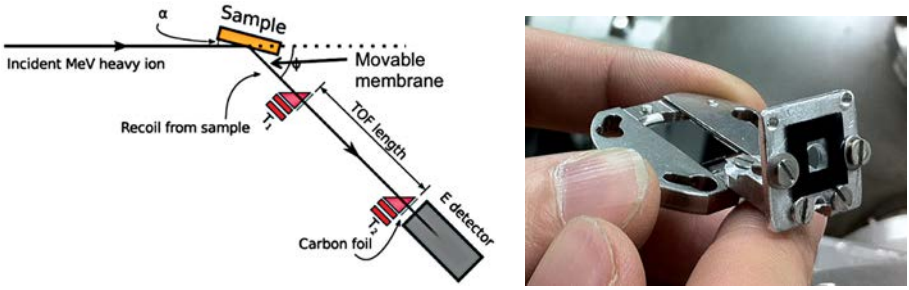

FIG. 21. Experimental set-up used at the University of Jyväskylä for stopping measurements (left) and photograph (right) of the sample holder containing both a silicon wafer sample with a thin gold layer at the surface for scattering the incident beam and a Si_3N_4 window. The window can be moved to the path of scattered incident ions by rotating the sample holder in a vacuum. (Reproduced courtesy of the University of Jyväskylä.)

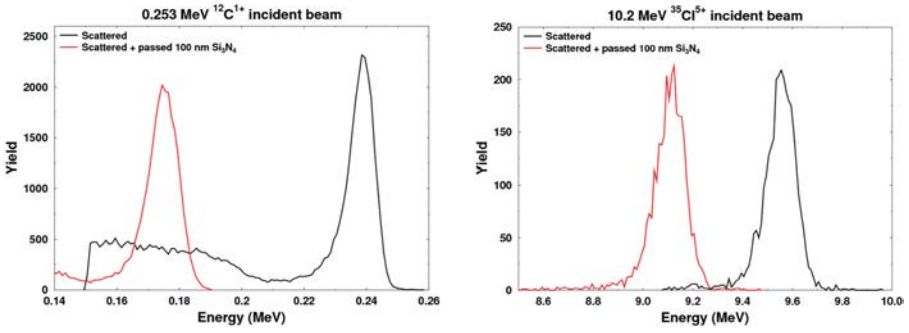

FIG. 22. Energy spectra for scattered 0.253 MeV ^{12}C (left) and 10.215 MeV ^{35}Cl (right) incident ions with (red line) and without (black line) 100 nm thick Si_3N_4. (Reproduced courtesy of the University of Jyväskylä.)

3.5. iTHEMBA LABORATORY FOR ACCELERATOR BASED SCIENCES

iThemba Laboratory for Accelerator Based Sciences,
Private Bag 11,
WITS 2050,
Johannesburg, Gauteng, South Africa
www.tlabs.ac.za/

The iThemba Laboratory for Accelerator Based Sciences (LABS) is a non-profit national research institution of the National Research Foundation of South Africa. It is highly multidisciplinary, as it is dedicated to physical, medical and biological sciences. The laboratory is based at two sites 1600 km apart, one in Cape Town and the other in Johannesburg. The main lines of research pursued are:

— Nuclear physics and materials research;
— Radiation therapy and cancer research;
— Production of unique radioisotopes.

3.5.1. Research activities in Johannesburg

Research at the Johannesburg site, where most of the CRP work reported here was carried out, is based around a refurbished 6 MV tandem accelerator that can produce a wide range of ion beams. Figure 23 shows the tandem tank, viewed from the injection side. Figure 24 is a view from the extraction side showing a 90º bending magnet and a beam switching magnet for directing the beam to the various beamlines. A user driven environmental isotope laboratory is also installed at Johannesburg, providing analytical services to research activities in:

— Isotope hydrology–water resources assessment;
— Pollution studies;
— Archaeometry;
— Medical and biological research.

The tandem accelerator is dedicated to research on low energy nuclear physics and IBA. The laboratory is open to scientists and postgraduate students from local universities, who can pursue their research activities using the facilities provided at iThemba LABS.

FIG. 23. The 6 MV iThemba LABS tandem accelerator viewed from the injection side. (Reproduced courtesy of iThemba LABS.)

FIG. 24. A view of the iThemba LABS 90° bending magnet (foreground) and the beam switching magnet of the tandem accelerator. (Reproduced courtesy of iThemba LABS.)

3.5.2. Ion beam analysis

The main analytical techniques used in materials research with IBA at iThemba LABS are micro-PIXE, (proton) RBS and heavy ion ERDA. The accelerator uses an 860C sputter ion source as well as an additional source for He^{+} RBS analyses. The research activities developed include:

— Depth profiling of transition metal based ceramics for applications in thin hard coatings;
— Analysis of 'smart' optical coatings;
— Impurity diffusion studies of nuclear materials;
— Elemental distribution in atmospheric aerosols for power plant monitoring;
— Imaging mineral phases in geological samples using micro-PIXE;
— Proton irradiation effects on diamond and graphite materials;
— Energy loss and energy loss straggling in ceramic materials.

The last point in the list is the result of the laboratory's participation in this CRP and is expected to continue beyond the CRP.

3.5.3. Experimental conditions

The technique used in the energy loss measurements at iThemba LABS was heavy ion ERDA. The main element of the set-up is an in-house built mass dispersive TOF spectrometer. The timing detectors, 60 cm apart, are carbon foil based microchannel plates. A passivated implanted planar silicon energy detector is located after the second time detector. The scattering angle is 30º to the incident beam direction, as shown in Fig. 25. The insert is a picture of the carbon foil

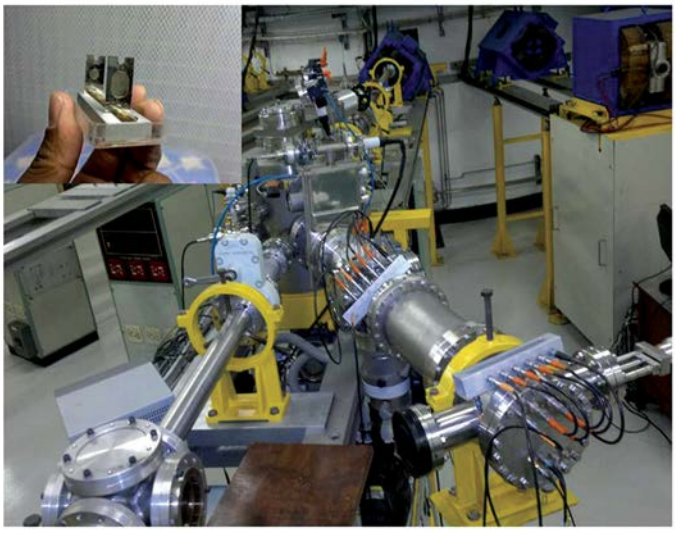

FIG. 25. The iThemba LABS heavy ion elastic recoil detection analysis beam line showing the time of flight detector telescope at 30º to the incident beam direction. The insert shows the carbon foil mountings for the timing detectors. (Reproduced courtesy of iThemba LABS.)

mountings for the timing detectors. The methods adopted for the measurement of the energy loss and straggling are described in Section 2.4.2.

Energy loss experiments can be made both for the primary beam scattered off a suitable heavy target element and for recoil ions ejected from the target. In both cases, the incident beam has a continuous range of energies, which offers the possibility of measuring stopping power values over a range of energies in a single run.

The stopper foil is perpendicular to the incoming beam path to avoid geometrical considerations (see Fig. 4). The foil holder is located between the second time detector and the passivated implanted planar silicon detector. It can be moved in and out of the beam path without breaking the vacuum.

The systems studied and the beam energies used are given in Table 1.

3.6. UNIVERSITÄT DER BUNDESWEHR MÜNCHEN, GERMANY

Institute for Applied Physics and Metrology — LRT2,
Universität der Bundeswehr München,
Werner-Heisenberg-Weg 39,
85577 Neubiberg, Germany
www.unibw.de/lrt2

The Institute for Applied Physics and Metrology of the Universität der Bundeswehr München focuses on applications based on three main experimental facilities:

— Scanning positron microscopy with positron annihilation;
— Scanning nuclear microbeam SNAKE, including hydrogen microscopy and directed irradiation of living cells with single ions;
— ERDA with a Q3D magnetic spectrograph.

The ion beam based activities of the institute take place at the 15 MV tandem accelerator of the Maier-Leibnitz Laboratory in Garching, close to Munich. The facilities incorporated and the research carried out therein are briefly described in the following subsections.

3.6.1. Tandem laboratory of the Maier-Leibnitz Laboratory

The accelerator laboratory is operated by the Ludwig Maximilian University of Munich and the Technical University of Munich. It performs basic

and interdisciplinary research concerning the interactions of ion beams with matter, nuclear physics, ion irradiation and IBA. These areas involve:

— Interaction of energetic ions in matter (energy loss, straggling, sputtering);
— IBA methods (ERDA, RBS, coincident proton–proton scattering, PIXE, PIGE and STIM);
— Modification of materials using MeV ions;
— Accelerator mass spectrometry;
— Irradiation of human cells (medical applications);
— Irradiation of new nuclear fuel material.

The institute is part of the European Union FP7 project SPIRIT and provides transnational access. Within the transnational access scheme, scientists from the European Union and associated countries can apply for beam time at any of the beamlines dedicated to IBA and cell irradiation.

The experimental facilities of the laboratory include (Fig. 26):

— A Q3D magnetic spectrograph (for nuclear physics and high resolution ERDA and RBS);
— A microbeam SNAKE (cell irradiation, proton–proton scattering, PIXE, PIGE and RBS);
— A gas filled magnet for accelerator mass spectrometry;
— Various irradiation stages;
— Different beamlines for nuclear physics experiments.

3.6.2. Experimental conditions

The work presented in this publication used the Q3D magnetic spectrograph at the Munich tandem accelerator [53], which is shown schematically in Fig. 27. The Q3D magnetic spectrograph has a large dispersion ($dE/(E dx) \approx 2 \times 10^{-4}$/mm), an excellent intrinsic resolution ($\Delta E/E = 2 \times 10^{-4}$), together with a large solid angle of detection (with a maximum value of up to 14.3 msr). Furthermore, the kinematical shift can be corrected up to the fourth order with a magnetic multipole element. In routine operation, the kinematic shift is corrected up to the third order only, leading to an overall energy resolution of 7×10^{-4}, even when a 5 msr solid angle is used [54]. An uncorrected kinematical shift would lead to a 6% energy spread at a 15° mean scattering angle. The multipole element is adjusted to focus the recoil ions scattered from a certain depth as well as possible in a given position on the focal plane of the Q3D. The ions are thus identified, and their position is measured, as shown in Fig. 27.

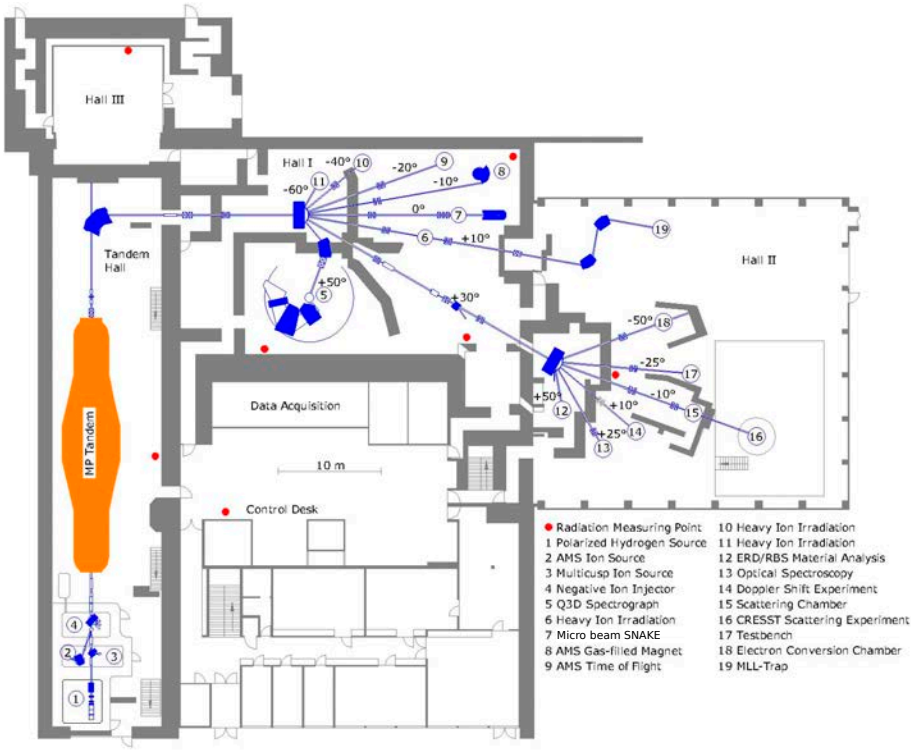

FIG. 26. Layout of the Munich accelerator facility. (Reproduced courtesy of the Universität der Bundeswehr München.)

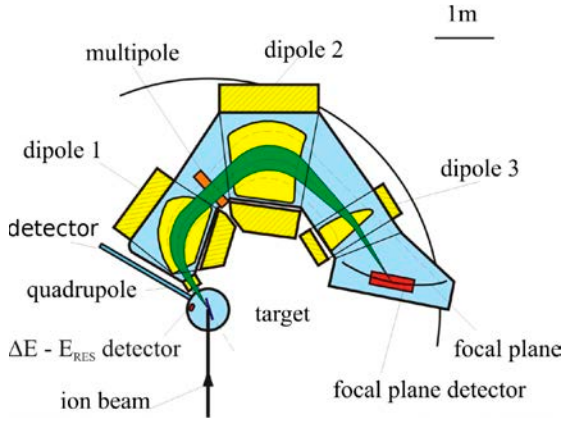

FIG. 27. Schematic drawing of the high resolution elastic recoil detection analysis set-up at the Munich Q3D magnetic spectrograph. (Reproduced courtesy of the Universität der Bundeswehr München.)

Thin foil targets are mounted for the stopping measurements perpendicular to the incident beam. After passing the thin foils, the energy loss of the ion beam is analysed with the Q3D spectrograph at a 0º scattering angle.

The systems studied and the beam energies used are given in Table 1.

4. MANUFACTURE AND PROCUREMENT OF TARGETS

A key issue in the experimental determination of stopping power is the availability of adequate targets. These must be very well characterized. In particular, in transmission or thin film experiments, the thickness and areal density of the target must be well known, as they directly influence the results obtained. Surface roughness, the presence of impurities and the exact stoichiometry in multielemental targets are also important parameters.

Three substrate materials were chosen for the preparation of the actual samples to be employed in the stopping force measurements: Si_3N_4, carbon foils and glassy carbon. Thin self-supporting Si_3N_4 foils were purchased in two sizes and two thicknesses (30 and 100 nm). Carbon foils with an areal density of 5 μg/cm^2 were purchased as an alternative thin backing for the films to be studied. Glassy carbon was used as a thick low-mass substrate. Atomic layer deposition (ALD) was used to grow Al_2O_3 and tantalum pentoxide (Ta_2O_5) films on all three sample types.

4.1. Si_3N_4 MEMBRANES

Commercially available Si_3N_4 membranes were acquired [55]. Membrane thicknesses of 30 and 100 nm were selected, both having surface areas of 4 mm × 4 mm and 5 mm × 5 mm. The manufacturer provided the following technical information:

— The stated membrane thicknesses are nominal values, and the real thickness values can deviate up to 10%.
— There is a possible batch to batch variation on the order of 3–4%. For a mean value of 100 nm, the batch may vary within approximately 97–103 nm, but the variation is probably smaller.
— Within a batch, adjacent wafers are very similar in thickness.

— The variation across a single wafer is usually better than 1%, and membranes for a single order are supplied from a single batch.
— Across a single membrane, even at 5 mm × 5 mm, the thickness variation will be much better than 1%.
— The membrane roughness should not be considerably worse than 0.5 nm.

These parameters are ideally suited for energy loss measurements and for use as substrates in the deposition of thin films of other materials, provided that the actual areal density of the membranes used is measured.

4.2. Al_2O_3 AND Ta_2O_5 ON Si_3N_4 AND ON CARBON FOILS

The Al_2O_3 and Ta_2O_5 samples were grown on the Si_3N_4 membranes by the ALD technique at the University of Helsinki, Laboratory of Inorganic Chemistry. The growth temperature was 250°C, and the employed facility was a Picosun SUNALE R-150 reactor.

In the preparation process, special attention was paid to eliminate ALD layer growth on the membrane backside, which would have triggered complications in the analysis of the measurement results. The following approaches were selected: (a) the Si_3N_4 membrane was placed on a polished silicon wafer, expecting that the back side would make a good seal, and (b) the membrane was wrapped in aluminium foil.

All 5 mm × 5 mm × 30 nm thick membranes broke during the ALD depositions, likely because of the stress arising from one sided depositions. Most 4 mm × 4 mm × 30 nm thick membranes also broke. The best combination of the size and substrate thickness was 4 mm × 4 mm × 100 nm. The samples prepared on the Si_3N_4 membranes are listed in Table 6. The thickness values given are based on the calibration of the deposition rate and are indicative only.

The samples were distributed to all the laboratories participating in this work. Two Si_3N_4 membranes, 100 and 30 nm thick, as well as an Al_2O_3 and a Ta_2O_5 sample, were selected for the stopping power measurements. Their composition and areal density were measured with ERDA at the Munich Q3D magnetic spectrograph with a 150 MeV ^{127}I beam. A $\Delta E - E$ detection system was used at a 38º scattering angle. The results are given in Table 7.

Carbon foils with an areal density of 5 μg/cm^2 were used to deposit, with ALD, foils of Al_2O_3 and Ta_2O_5. They were mounted on stainless steel supports that had a 5 mm diameter opening. The samples prepared are presented in Table 8.

The following samples were deposited on glassy carbon substrates:

— Al_2O_3, thickness: 221–249 nm;
— Ta_2O_5, thickness: 185–198 nm.

4.3. FOIL TARGETS ON CARBON BACKING

A set of foil targets was prepared at the Technical University of Munich. The thickness of the foils was chosen to achieve an energy loss less than 2% of the initial energy. The areal density of the carbon backings was in the range of 4–5 μg/cm^2. Carbon, aluminium, nickel, gold, Al_2O_3, silicon and hafnium foils were produced.

4.4. ZrO_2, Al_2O_3 AND SiO_2 ON Si_3N_4 FOILS

Al_2O_3 and silica (SiO_2) films were produced by electron beam deposition onto Si_3N_4 foils at the Materials Department of iThemba LABS. Commercially available zirconia (ZrO_2) foils were acquired and mounted on steel frames, each with a circular aperture 0.8 cm in diameter. The samples are listed in Table 9.

The topography of the foils was mapped using AFM, scanning over areas of up to 20 μm × 20 μm at a time. Several regions on each foil were scanned.

TABLE 6. SAMPLES PREPARED ON THE Si_3N_4 MEMBRANES

Window area (mm)	Si_3N_4 membrane thickness (nm)	Material	Thickness (nm)
4 × 4	30	Al_2O_3	32.6
4 × 4	100	Al_2O_3	117–135
4 × 4	100	Al_2O_3	104–114
4 × 4	100	Al_2O_3	32.6
4 × 4	100	Ta_2O_5	88–99
5 × 5	100	Ta_2O_5	97–99
5 × 5	100	Al_2O_3	107–116
5 × 5	100	Al_2O_3	32.6

TABLE 7. ELEMENTAL COMPOSITION OF THE Si_3N_4 BASED SAMPLES

Sample		Hydrogen	Carbon	Nitrogen	Oxygen	Aluminium	Silicon	Tantalum
100 nm Si_3N_4	Coverage (at./cm^2)	1.338×10^{16}	1.596×10^{15}	3.597×10^{17}	8.377×10^{15}	n.a.[a]	3.021×10^{17}	n.a.
	Statistical error (at./cm^2)	8.365×10^{14}	5.321×10^{14}	7.873×10^{15}	1.185×10^{15}	n.a.	6.563×10^{15}	n.a.
30 nm Si_3N_4	Coverage (at./cm^2)	7.162×10^{15}	1.179×10^{15}	7.839×10^{16}	7.577×10^{15}	n.a.	6.544×10^{16}	n.a.
	Statistical error (at./cm^2)	4.990×10^{14}	3.730×10^{14}	2.997×10^{15}	9.188×10^{14}	n.a.	2.491×10^{15}	n.a.
100 nm Si_3N_4 + 30 nm Al_2O_3	Coverage (at./cm^2)	1.785×10^{16}	5.569×10^{15}	3.193×10^{17}	2.599×10^{17}	1.605×10^{17}	2.989×10^{17}	n.a.
	Statistical error (at./cm^2)	6.767×10^{14}	6.961×10^{14}	5.196×10^{15}	4.622×10^{15}	3.503×10^{15}	4.573×10^{15}	n.a.
100 nm Si_3N_4 + 100 nm Ta_2O_5	Coverage (at./cm^2)	9.025×10^{16}	6.980×10^{15}	3.273×10^{17}	4.281×10^{17}	n.a.	3.042×10^{17}	1.452×10^{17}
	Statistical error (at./cm^2)	2.271×10^{15}	1.163×10^{15}	7.852×10^{15}	8.855×10^{15}	n.a.	6.887×10^{15}	2.968×10^{15}

[a] n.a.: not applicable.

TABLE 8. SAMPLES PREPARED ON 5 μg/cm^2 CARBON FILMS

Material	Thickness (nm)
Al_2O_3	117–135
Al_2O_3	104–114
Al_2O_3	32.6
Ta_2O_5	88–99
Ta_2O_5	25–35

TABLE 9. SAMPLES PREPARED AT iTHEMBA LABS

Material	Areal density (μg/cm^2)	Roughness (nm)
ZrO_2	331	3.0
Si_3N_4	22.8	0.3
Al_2O_3	38.4	0.5
SiO_2	27.9	0.6

Figure 28 shows a typical AFM image of the Al_2O_3 foil on Si_3N_4, from which the roughness of the foil surface was estimated. A measure of the surface roughness helps to determine the significance of the topographic variations in the measurement of the foil thickness.

4.5. SAMPLES FOR THE BULK SAMPLE METHOD

The samples used for the bulk sample method are listed in Table 10. In all cases, a thin gold marker layer was deposited on top of the samples by evaporation.

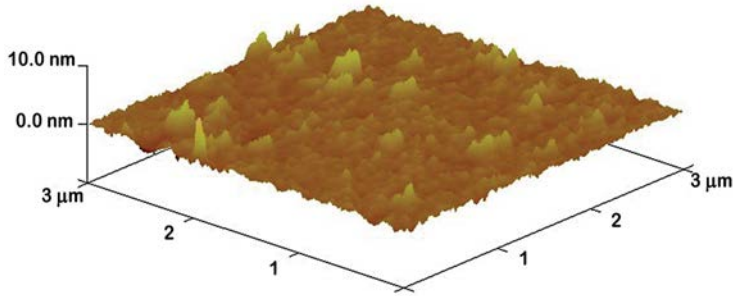

FIG. 28. Atomic force microscopy image of a 3 µm × 3 µm region of the Al_2O_3 foil on Si_3N_4. The average roughness of the foil surface was determined to be 0.48 nm, 0.5% of the foil thickness. (Reproduced courtesy of iThemba LABS.)

TABLE 10. SAMPLES USED FOR THE BULK SAMPLE METHOD

Sample	Sample production method
a-Si	Silicon self-amorphized by implanting silicon at the temperature of liquid nitrogen, with 5×10^{15} at./cm^2 at 340 keV and 5×10^{15} at./cm^2 at 100 keV. This leads to an amorphous silicon layer 300 nm thick.
Glassy carbon/TiO_2	Unbalanced pulsed direct current reactive magnetron sputtering, from a high purity titanium target in an argon–oxygen atmosphere.
Sapphire/InN 400 nm	Molecular beam epitaxy.
Sapphire/GaN 200 nm	Molecular beam epitaxy.
Si/Ta_2O_5 190 nm	ALD at 250ºC.

5. CALCULATION OF UNCERTAINTIES

5.1. CONCEPTS AND METHODS

The Guide to the Expression of Uncertainty in Measurement (GUM) [56] is a publication prepared by the Joint Committee for Guides in Metrology of the International Bureau of Weights and Measures and sets the standard for

the evaluation of uncertainties. Reference [56] provides clear definitions of the concepts involved as well as standard recognized methods to deal with them.

The precision of a measurement is a measure of the closeness of the results of repeated measurements of the same quantity in the same specified conditions. This is very closely connected to the concepts of repeatability and reproducibility. Precision is usually given numerically as a standard deviation.

Accuracy expresses how close the measured value of a given quantity is to the true value. Except for fundamental constants, the value of which is defined, the true value of a quantity is not knowable. Furthermore, a very high precision measurement (e.g. an RBS spectrum with very high counting statistics) can have very low accuracy if there are large systematic errors (e.g. in the determination of the beam fluence).

The uncertainty of a measurement is the dispersion of the values assigned to a given quantity. It is usually given numerically as a standard deviation together with a stated coverage probability. Uncertainty includes components of statistical as well as of systematic origin.

Sources of uncertainty are divided in two groups. Type A uncertainties can be calculated as the standard deviation of the results obtained in a series of measurements. This is the case, for instance, for statistical uncertainty. Type B uncertainties can also be characterized by a standard deviation, but they are based on user experience or other information. In practice, the user has to make a more informal estimate of the probable measurement error.

For instance, the result of the measurement of the stopping power of one material for one ion often depends on the stopping power of the same material for a different ion, or of a different (reference) material. The uncertainty of the new measurement must include the uncertainty of the reference stopping power, which may be unknown or unreliable (e.g. if the original measurement assigned as ‘uncertainty’ only the statistical uncertainty). In this case, one could assign as the uncertainty of the reference stopping power, for instance, the average accuracy of SRIM for similar cases or a value coming from the deviation between SRIM and the experimental stopping power of the reference material. This would be a type B uncertainty.

The uncertainty budget is specified by GUM as a formal approach to the systematic evaluation of the uncertainty of a measurement. It is the statement of a measurement uncertainty, of the components of that measurement uncertainty, and of their calculation and combination. This concept was described, with special reference to IBA, by Sjöland et al. [57] and is also described in the chapter on pitfalls of the Handbook of Modern Ion Beam Analysis [58].

The GUM uncertainty framework described above has some limitations, in particular in the presence of non-linear behaviour between input parameters and results, and of strong correlations between parameters. In such cases, one

practical alternative to the GUM uncertainty framework to estimate uncertainty is to use Bayesian inference with Monte Carlo methods [59]. This is the basis of the bulk sample method already described in Section 2.4.6.

All the uncertainties in this work are given with a coverage factor of $k = 1$; that is, they are one standard deviation, except where otherwise stated.

As a final note, the uncertainty budgets presented are not completely equivalent to each other, as the sources of uncertainty listed in each one are not always all the same. The reason is that the experimental set-ups and the experiments undertaken are not equivalent; furthermore, in some cases, the uncertainty of some experimental parameters has been determined by the researcher, thus allowing for a more detailed estimation. For instance, the beam and system energy spread results from several phenomena, and an estimate can lump all of them into a single value. However, if one of its sources (e.g. the terminal voltage uncertainty or the maximum temperature induced energy drift) is known, then it can be discriminated separately in the uncertainty budget.

5.2. MEASUREMENTS MADE AT THE UNIVERSITÄT DER BUNDESWEHR MÜNCHEN

This section presents several uncertainty budgets for different experiments performed at the Universität der Bundeswehr München.

The uncertainty budget for the determination of the areal density of the Si_3N_4 based foils made at the Munich Q3D magnetic spectrograph is given first separately. The reason is that these samples were used by several participating laboratories to measure the stopping power for different ions.

An uncertainty budget is not presented for each stopping power measurement (i.e. for each ion–target combination) because, in many cases, they are very similar. Representative cases are given in detail.

5.2.1. Areal density of Si_3N_4 membranes

The uncertainty budget for the determination of the areal density of a Si_3N_4 membrane, nominally 100 nm thick, at the Munich Q3D magnetic spectrograph is summarized in Table 11.

An ERDA experiment was performed at the Munich Q3D magnetic spectrograph using a 150 MeV ^{127}I beam. A $\Delta E - E$ detection system was used at a 38º scattering angle. The results are shown in Table 7.

The Q3D spectrograph has an ion beam energy spread and detector resolution that together combine to $\Delta E/E = 4 \times 10^{-4}$ (FWHM). The scattering cross-section

depends on the ion energy with $1/E^2$, and the corresponding uncertainty in the areal density determined is 0.04%, which is the first term in the uncertainty budget.

An absolute measurement of the composition and areal density of the sample requires a precise knowledge of the scattering angle, of the solid angle of the detector and of the beam fluence. In this case, the experiment was instead relative to a known target. The Munich group has done extensive work on energy loss on carbon foils, including the determination of the stopping power for 60 MeV ^{58}Ni with an accuracy of 0.8% [60]. The areal density of a reference carbon foil can be determined by measuring the energy loss of 60 MeV ^{58}Ni in transmission geometry at normal incidence. Then, the same carbon foil is measured with ERDA under exactly the same conditions as the actual sample of interest. In this way, the scattering angle and solid angle do not contribute to the uncertainty. The beam fluence does contribute, first when the carbon foil is measured with ERDA and a second time when the actual sample is measured. The beam current is measured with a rotating wire loop in the beam line. The stability and accuracy of this measurement is, for the currents used, around 0.5%. This value enters the uncertainty budget twice, once for the carbon measurement and once for the Si_3N_4 measurement. The 0.8% uncertainty in the stopping power of 60 MeV ^{58}Ni in carbon is also included. A 0.04% contribution from the uncertainty in the beam energy when measuring the carbon reference material with ERDA is also included.

The uncertainty attributable to the counting statistics is 2.48%, which is the total value including all the elements present.

Pile-up is a non-linear effect that can significantly change the measured yield for high beam currents and high count rates. In this experiment, the beam current was kept at very low values, with a dead time of practically 0%.

A type B uncertainty is included because of the data analysis. The value quoted of 0.83% was derived from an IAEA intercomparison of IBA software [3] for ^{4}He ERDA. A similar study for heavy ion ERDA has not been undertaken to date. The data analysis in this experiment was not performed with a code, since the yield can be directly converted to an areal density. However, the problems involved in data analysis codes are the same: effects, such as multiple and plural scattering and even very small roughness values, interfere with the results obtained, and their effect on the yield is not completely known. So, in a direct yield to *Nt* conversion, all these effects are not taken into account (or even if they are, the issue remains). The GUM prescription of making an informal estimate of the probable measurement error was followed, in which all these effects were lumped in with the 0.83% code uncertainty derived for ^{4}He ERDA.

The Rutherford cross-section needs to be corrected for electron screening effects. The screening model of Andersen et al. [61] was used in the actual data analysis. However, other models can be used, for instance by calculating the cross-section from assumed interatomic potentials [11]. The analytical code

TABLE 11. UNCERTAINTY BUDGET FOR DETERMINATION OF THE 100 nm Si_3N_4 AREAL DENSITY

Source of uncertainty	Uncertainty (%)
Beam energy spread $\Delta E/E = 4 \times 10^{-4}$ (FWHM)	0.04
Counting statistics (total, added for all elements present)	2.48
Accuracy of current measurement in measurement of sample	0.5
Uncertainty in *Nt* of reference material attributable to beam energy spread	0.04
Accuracy of current measurement in measurement of carbon reference foil	0.5
Pile-up uncertainty	≈0
Standard uncertainty (precision)	2.58
Scattering angle: relative measurement	0
Stopping power of ^{60}Ni in carbon, used to determine reference material carbon *Nt*	0.8
Code uncertainty	0.83
Rutherford cross-section: screening model	0.87
Total combined standard uncertainty (accuracy)	2.96
Layer thickness inhomogeneity (from manufacturer)	1
Total combined standard uncertainty for stopping (accuracy)	3.1

NDF [18] and the Monte Carlo code Corteo [62] were used to calculate the screened cross-section for different screening options, for the conditions of this experiment. Perhaps surprisingly, there was a fairly large scattering of the results, as shown in Fig. 29, and an extra uncertainty arising from the screening model of 0.87% was calculated.

When using this to calculate stopping power from measurements with different Si_3N_4 membranes, an extra uncertainty of 1% from the layer thickness inhomogeneity must also be added.

In any case, it is clear that in this experiment it is the counting statistics that dominate the final total uncertainty.

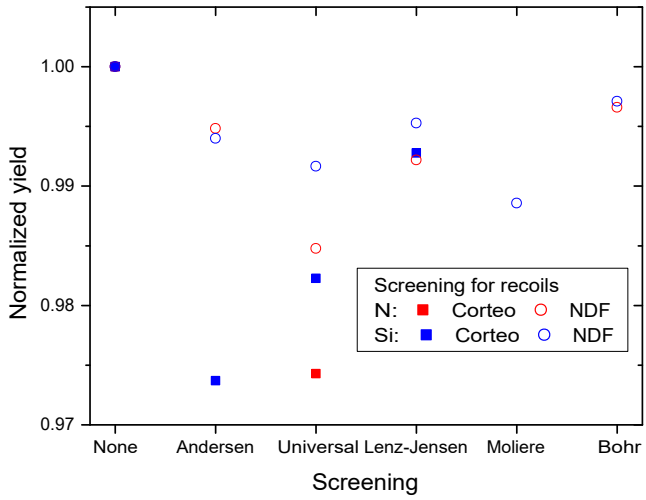

FIG. 29. Normalized yield for 150 MeV ^{127}I ions on a 100 nm Si_3N_4 membrane for different electron screening models, calculated with NDF and Corteo.

The uncertainty budget for the Si_3N_4 membrane, nominally 30 nm thick, is almost identical. The only contributing term that is different is the counting statistics, which is 4.56%. This leads to a precision of 4.61%; an accuracy of 4.83%; and an accuracy for stopping calculations, including the layer thickness inhomogeneity, of 4.9%. As in the previous case, the counting statistics dominate the total uncertainty.

5.2.2. Areal density of Al_2O_3 on Si_3N_4

The uncertainty budget for the determination made in Munich of the areal density of the Al_2O_3 foil grown on the 100 nm Si_3N_4 membrane is summarized in Table 12. Almost all the terms are the same as for the Si_3N_4 membrane, with the same justification. In cases of the inhomogeneity of the Al_2O_3 layer thickness, the same 1% as for the Si_3N_4 substrate was assumed.

One extra term arose from the impurity content in the Al_2O_3 foil. The Si_3N_4 membrane already had a certain impurity content, mostly hydrogen, carbon and oxygen. In the Al_2O_3/Si_3N_4 sample, in principle it was not known how the impurities were distributed. It was assumed that the Si_3N_4 backing had the same impurity content as determined for the stand-alone Si_3N_4 membrane. Half the carbon and oxygen content of the stand-alone Si_3N_4 membrane was taken as the uncertainty in the areal density of the Al_2O_3 foil. Hydrogen was not included because it had almost no effect on the stopping power.

TABLE 12. UNCERTAINTY BUDGET FOR DETERMINATION OF THE Al_2O_3 FOIL AREAL DENSITY

Source of uncertainty	Uncertainty (%)
Beam energy spread $\Delta E/E = 4 \times 10^{-4}$ (FWHM)	0.04
Counting statistics (total, added for all elements present)	2.26
Accuracy of current measurement in measurement of sample	0.5
Uncertainty in *Nt* of reference material attributable to beam energy spread	0.04
Accuracy of current measurement in measurement of carbon reference foil	0.5
Pile-up uncertainty	≈0
Impurity content	1.2
Standard uncertainty (precision)	2.65
Scattering angle: relative measurement	0
Stopping power of ^{60}Ni in carbon, used to determine reference material carbon *Nt*	0.8
Code uncertainty	0.83
Rutherford cross-section: screening model	0.87
Total combined standard uncertainty (accuracy)	3.07
Layer thickness inhomogeneity, assumed to be equal to Si_3N_4	1
Total combined standard uncertainty for stopping (accuracy)	3.2

The actual areal density considered, excluding the impurity content as determined for the stand-alone Si_3N_4 membrane, is 420.5×10^{15} at./cm^2.

5.2.3. Areal density of Ta_2O_5 on Si_3N_4

The uncertainty budget for the determination made in Munich of the areal density of the Ta_2O_5 foil grown on the 100 nm Si_3N_4 membrane is summarized in

Table 13. All the terms are the same as for the Al_2O_3 foil on the Si_3N_4 membrane, with the same justification.

Again, in this case, the accuracy reached is determined by the counting statistics, with all other sources having a smaller combined contribution to the final value. However, it was noted that the contributions attributable to the data analysis (code uncertainty) and to the Rutherford cross-section (screening model) alone would lead to an uncertainty of 1.2%. Therefore, that is the limit that could be achieved unless progress on those two aspects were made.

TABLE 13. UNCERTAINTY BUDGET FOR DETERMINATION OF THE Ta_2O_5 FOIL AREAL DENSITY

Source of uncertainty	Uncertainty (%)
Beam energy spread $\Delta E/E = 4 \times 10^{-4}$ (FWHM)	0.04
Counting statistics (total, added for all elements present)	2.36
Accuracy of current measurement in measurement of sample	0.5
Uncertainty in *Nt* of reference material attributable to beam energy spread	0.04
Accuracy of current measurement in measurement of carbon reference foil	0.5
Pile-up uncertainty	≈0
Impurity content	0.9
Standard uncertainty (precision)	2.62
Scattering angle: relative measurement	0
Stopping power of ^{60}Ni in carbon, used to determine reference material carbon *Nt*	0.8
Code uncertainty	0.83
Rutherford cross-section: screening model	0.87
Total combined standard uncertainty (accuracy)	2.99
Layer thickness inhomogeneity, assumed to be equal to Si_3N_4	1
Total combined standard uncertainty for stopping (accuracy)	3.2

5.2.4. Stopping power of Si_3N_4 for 60 MeV nickel

This uncertainty budget is for the energy loss measurement made in Munich for the Si_3N_4 100 nm membrane with a 60 MeV nickel beam. The uncertainty budget for the areal density of the membrane is given in Section 5.2.1.

First, the uncertainty of the energy at which the stopping power is determined was ascertained (Table 14). The first component is the uncertainty in the energy calibration of the magnet, which includes a possible energy drift from experiment to experiment. Without detailed knowledge about these issues, 5 keV was taken as an upper limit in these experiments, but the real value is probably smaller. This is a systematic uncertainty.

The second component is the beam and energy spread, which is is 4×10^{-4} at FWHM. For 60 MeV, the corresponding standard deviation is 10 keV.

A third component is the uncertainty in the determination of the energy of the transmitted beam. The measured energy loss width was 54.5 keV, but this value is a measure of the energy straggling, not an uncertainty of the actual beam energy. The mean and mode (most probable value) of an energy distribution can usually be determined with a much higher accuracy than can its width [63]. One issue is that, for non-symmetrical distributions, the mean and the mode do not coincide, and there is some ambiguity about which value should be taken. In this case, this was a minor issue as the energy distribution of the transmitted beam was very nearly Gaussian shaped. The fit of a Gaussian to the energy distribution yielded an uncertainty for the mean of 5 keV or less, and this is the value that was used.

The largest contribution is, however, the actual energy loss in the Si_3N_4 membrane, which was 943.7 keV. That is, the initial beam energy was 60 MeV, the final beam energy was 69.0563 MeV, and the stopping power determined is an average value over this energy range. The average energy in the membrane, 59.5281 MeV, can be taken as the energy for which the stopping power is determined, and a 943.7 keV energy loss can be taken as the FWHM of this energy. The corresponding standard deviation is 402 keV.

The uncertainty budget for the stopping power value is given in Table 15. The precision of the experiment is given by the beam and system energy spread and by the uncertainty in the estimation of the energy of the transmitted beam, relative to the actual energy loss. The uncertainty is obtained by including the uncertainty in the areal density of the Si_3N_4 membrane, which was calculated in Section 5.2.1.

It is clear that the total uncertainty is dominated by the uncertainty of the areal density of the Si_3N_4 membrane.

The actual value of the stopping cross-section determined is $943.7 \times 10^3/685.2 = 1377$ eV/(10^{15} at./cm^2).

TABLE 14. UNCERTAINTY BUDGET FOR ENERGY AT WHICH STOPPING POWER IS DETERMINED FOR 60 MeV NICKEL ON 100 nm Si_3N_4 (MUNICH)

Source of uncertainty	Uncertainty (keV)
Beam and system energy spread $\Delta E/E = 4 \times 10^{-4}$ (FWHM)	10
Uncertainty in estimation of energy of transmitted beam	5
Total energy loss in the foil (divided by 2.35 to obtain sigma)	402
Standard uncertainty (precision)	402
Beam energy: uncertainty in calibration of magnet	5
Total combined standard uncertainty (accuracy)	402

TABLE 15. UNCERTAINTY BUDGET FOR THE STOPPING POWER OF Si_3N_4 FOR 60 MeV NICKEL (MUNICH)

Source of uncertainty	Uncertainty
Total energy loss in foil	943.7 keV
Beam and system energy spread $\Delta E/E = 4 \times 10^{-4}$ (FWHM)	10 keV
Uncertainty in estimation of energy of transmitted beam	5 keV
Total energy uncertainty as percentage of energy loss in foil	1.2%
Standard uncertainty (precision)	1.2%
Uncertainty in areal density of foil	3.1%
Total combined standard uncertainty (accuracy)	3.3%

The effects mentioned by Mertens [28] that can affect the result of an energy loss measurement, such as sputtering of the foil material under the beam, foil contraction, target texture effects in polycrystalline materials and outgassing, are not included in the uncertainty budget presented, because even an informal estimate is extremely difficult to make. One alternative would be to replace all those effects with the standard deviation of heavy ion stopping data with respect

to SRIM in this velocity range, which it could be argued is akin to an average uncertainty of stopping power measurements in general. For heavier ions (Z of 19–92) in solid compounds in the 0.25–2.5 MeV/nucleon velocity range, this standard deviation is 9.2% [5]. Taking this value would, however, ignore the details of this particular experiment and the care taken in the procedures adopted, including the low beam current and the low total beam fluence.

5.2.5. Stopping power of Al_2O_3 (on Si_3N_4) for 60 MeV nickel

This uncertainty budget is for the energy loss measurement made in Munich for an Al_2O_3 foil on a 100 nm Si_3N_4 membrane with a 60 MeV nickel beam. The uncertainty budget for the areal density of the foil is given in Section 5.2.2.

First, the uncertainty of the energy at which the stopping power is determined was ascertained (Table 16). The same sources of uncertainty as for Si_3N_4 are present. A further component is the uncertainty attributable to the energy loss in the Si_3N_4 membrane.

The energy loss in the Si_3N_4 membrane can be calculated by scaling the energy loss in the stand-alone Si_3N_4 membrane studied in Section 5.2.4. This was 943.7 keV for an areal density of 685.1×10^{15} at./cm^2. The areal density of the Si_3N_4 membrane of the Al_2O_3/Si_3N_4 sample is 641.5×10^{15} at./cm^2 (assuming the same amount of impurities as in the stand-alone Si_3N_4). This scaling leads to a calculated energy loss in the Si_3N_4 membrane of 883.6 keV. There is a 3.3% uncertainty, as calculated in Section 5.2.4, which is 29 keV.

However, this calculation assumes that the beam energy is the same, but in the case of the Al_2O_3/Si_3N_4 sample, the beam already crossed the Al_2O_3 layer, losing some energy. The total energy loss in the Al_2O_3/Si_3N_4 sample was 1488.2 keV. At a first approximation, the energy loss in the Al_2O_3 layer was 1488.2 keV – 884 keV = 604.2 keV. Then, the energy inciding on the Si_3N_4 layer was 60 MeV – 0.6042 MeV = 59.3958 MeV. The energy dependence, as calculated with SRIM, can be used to correct the energy loss in the Si_3N_4. A value of 882.7 keV instead of 883.6 keV was obtained. The 3.3% uncertainty is also 29 keV. The energy loss in the Al_2O_3 layer becomes 1488.2 keV – 882.7 keV = 605.5 keV.

The uncertainty budget for the actual stopping power measurement is given in Table 17. It is similar to the one for the stand-alone Si_3N_4 membrane, but it also has an extra component because of the uncertainty in the energy loss in the Si_3N_4. This arises from the uncertainties in the beam and system energy spread, the estimation of the energy of the transmitted beam and the energy loss in the Si_3N_4. Adding the three terms in quadrature, 31.1 keV is obtained, which is 5.2% of the energy loss in the Al_2O_3.

The largest contribution to the total uncertainty is the uncertainty in the energy loss in the Si_3N_4 membrane.

The actual value of the stopping cross-section determined is $605.5 \times 10^3/420.5 = 1440$ eV/(10^{15} at./cm^2).

TABLE 16. UNCERTAINTY BUDGET FOR ENERGY AT WHICH STOPPING POWER IS DETERMINED FOR 60 MeV NICKEL ON Al_2O_3 (MUNICH)

Source of uncertainty	Uncertainty (keV)
Beam and system energy spread $\Delta E/E = 4 \times 10^{-4}$ (FWHM)	10
Uncertainty in estimation of energy of transmitted beam	5
Total energy loss in the foil (divided by 2.35 to obtain sigma)	257
Uncertainty of energy loss in the Si_3N_4 membrane	29
Standard uncertainty (precision)	259
Beam energy: uncertainty in calibration of magnet	5
Total combined standard uncertainty (accuracy)	259

TABLE 17. UNCERTAINTY BUDGET FOR THE STOPPING POWER OF Al_2O_3 FOR 60 MeV NICKEL (MUNICH)

Source of uncertainty	Uncertainty
Energy loss in Al_2O_3 foil	605.5 keV
Beam and system energy spread $\Delta E/E = 4 \times 10^{-4}$ (FWHM)	10 keV
Uncertainty in estimation of energy of transmitted beam	5 keV
Uncertainty of energy loss in the Si_3N_4 membrane	29 keV
Total energy uncertainty as percentage of energy loss in foil	5.2%
Standard uncertainty (precision)	5.2%
Uncertainty in areal density of Al_2O_3 foil	3.2%
Total combined standard uncertainty (accuracy)	6.1%

5.2.6. Stopping power of Ta_2O_5 (on Si_3N_4) for 60 MeV nickel

This uncertainty budget is for the energy loss measurement made in Munich for a Ta_2O_5 foil on a 100 nm Si_3N_4 membrane with a 60 MeV nickel beam. The uncertainty budget for the areal density of the foil is given in Section 5.2.3.

The uncertainty of the energy at which the stopping power is determined is given in Table 18.

Following the same method as for Al_2O_3, the energy loss in the Si_3N_4 is 900.1 keV. This has a 3.3% uncertainty, as calculated in Section 5.2.4, which is 30 keV. The energy loss in the Ta_2O_5 layer becomes 2126.6 keV – 900.1 keV = 1226.5 keV

The uncertainty budget for the actual stopping power measurement is given in Table 19. It is similar to the one for the stand-alone Si_3N_4 membrane, but it also has an extra component attributable to the uncertainty in the energy loss in the Si_3N_4. This extra component arises from the uncertainties in the beam and system energy spread, in the estimation of the energy of the transmitted beam and in the energy loss in the Si_3N_4. Adding the three terms in quadrature, 32.0 keV is obtained, which is 2.6% of the energy loss in the Ta_2O_5.

The uncertainty in the energy loss in the Si_3N_4 membrane and the uncertainty in the Ta_2O_5 areal density are similar.

The actual value of the stopping cross-section determined is $1226.5 \times 10^3/647.2 = 1895$ eV/(10^{15} at./cm^2).

TABLE 18. UNCERTAINTY BUDGET FOR ENERGY AT WHICH STOPPING POWER IS DETERMINED FOR 60 MeV NICKEL ON Ta_2O_5 (MUNICH)

Source of uncertainty	Uncertainty (keV)
Beam and system energy spread $\Delta E/E = 4 \times 10^{-4}$ (FWHM)	10
Uncertainty in estimation of energy of transmitted beam	5
Total energy loss in the foil (divided by 2.35 to obtain sigma)	539
Uncertainty of energy loss in the Si_3N_4 membrane	30
Standard uncertainty (precision)	540
Beam energy: uncertainty in calibration of magnet	5
Total combined standard uncertainty (accuracy)	540

TABLE 19. UNCERTAINTY BUDGET FOR THE STOPPING POWER OF Ta_2O_5 FOR 60 MeV NICKEL (MUNICH)

Source of uncertainty	Uncertainty
Energy loss in Ta_2O_5 foil	1226.5 keV
Beam and system energy spread $\Delta E/E = 4 \times 10^{-4}$ FWHM)	10 keV
Uncertainty in estimation of energy of transmitted beam	5 keV
Uncertainty of energy loss in the Si_3N_4 membrane	30 keV
Total energy uncertainty as a percentage of energy loss in foil	2.6%
Standard uncertainty (precision)	2.6%
Uncertainty in areal density of Ta_2O_5 foil	3.2%
Total combined standard uncertainty (accuracy)	4.1%

Compared with the Al_2O_3 measurement given in Section 5.2.5, the larger energy loss in the Ta_2O_5 layer leads to a smaller uncertainty in the stopping cross-section value, which is compensated by a larger uncertainty in the energy at which the stopping cross-section is determined.

5.2.7. Stopping power of Al_2O_3 (on carbon) for 60 MeV nickel

This uncertainty budget is for the energy loss measurement made in Munich for an Al_2O_3 foil deposited on a carbon foil, with a 60 MeV nickel beam. Several foils were deposited on carbon backings, and energy loss experiments for several ions were performed. This uncertainty budget is representative of the different experiments for samples deposited in Munich.

The uncertainty of the energy at which the stopping power is determined is given in Table 20. In comparison with the previous uncertainty budgets, the contribution attributable to the estimation of the energy of the transmitted beam is larger, which is caused by the asymmetry of the energy distribution (Fig. 30).

A 5 μg/cm^2 carbon areal density was assumed, with an uncertainty of 3.2% (the same assumption as for the sample on Si_3N_4). The experimental values for the stopping power of carbon for nickel in this energy range show a deviation of around 10% relative to SRIM (see the data in Paul's compilation [64]), and this value is taken as the uncertainty attributable to the carbon stopping power.

TABLE 20. UNCERTAINTY BUDGET FOR ENERGY AT WHICH STOPPING POWER IS DETERMINED FOR 60 MeV NICKEL ON Al_2O_3/CARBON (MUNICH)

Source of uncertainty	Uncertainty (keV)
Beam and system energy spread $\Delta E/E = 4 \times 10^{-4}$ (FWHM)	10
Uncertainty in estimation of energy of transmitted beam	20
Total energy loss in the foil (divided by 2.35 to obtain sigma)	635
Average energy loss in carbon backing: 49 keV/(μg/cm^2)	245
Uncertainty in areal density of carbon backing	8
Uncertainty attributable to carbon stopping power	24.5
Carbon backing thickness inhomogeneity (roughness)	49
Total uncertainty in energy loss attributable to carbon backing	55
Standard uncertainty (precision)	637
Beam energy: uncertainty in calibration of magnet	5
Total combined standard uncertainty (accuracy)	637

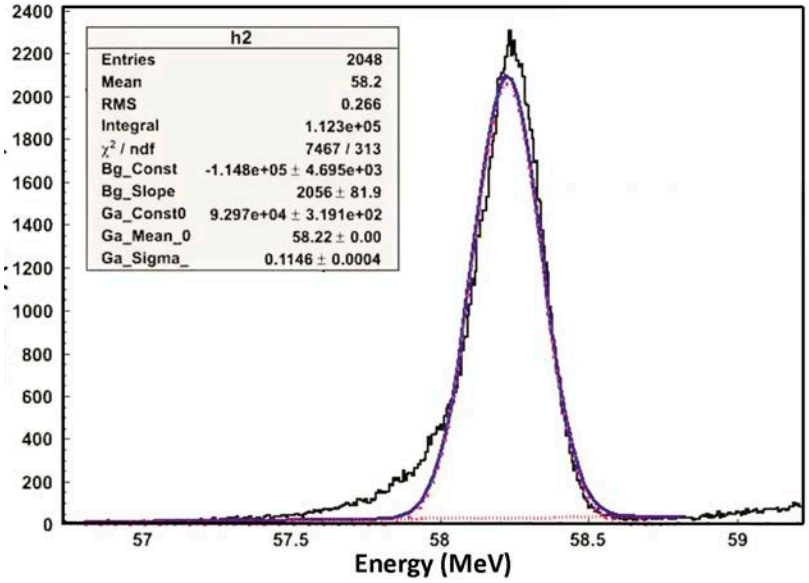

FIG. 30. Energy profile of a 60 MeV Ni beam after passing through a foil with 30.9 μg/cm^2 Al_2O_3 on 4.9 μg/cm^2 carbon. (Reproduced courtesy of the Universität der Bundeswehr München.)

TABLE 21. UNCERTAINTY BUDGET FOR THE STOPPING POWER OF Al_2O_3/CARBON FOR 60 MeV NICKEL (MUNICH)

Source of uncertainty	Uncertainty
Energy loss in Al_2O_3 foil	1.5 MeV
Beam and system energy spread $\Delta E/E = 4 \times 10^{-4}$ (FWHM)	10 keV
Uncertainty in estimation of energy of transmitted beam	20 keV
Uncertainty of energy loss in the carbon foil	55 keV
Total energy uncertainty as percentage of energy loss in foil	4.0%
Standard uncertainty (precision)	4.0%
Uncertainty in areal density of Al_2O_3 foil	3.2%
Total combined standard uncertainty (accuracy)	5.1%

Finally, a roughness (layer thickness inhomogeneity) of 1 μg/cm^2 carbon is assumed, which is conservative. The use of a microslit to reduce the beam current means that the beam spot is small and probes only a small part of the sample.

The uncertainty budget for the actual stopping power measurement is given in Table 21. It can be seen that the uncertainty in the energy loss in the Al_2O_3 foil and the uncertainty in the Al_2O_3 areal density contribute in a similar way to the total uncertainty.

5.3. MEASUREMENTS MADE AT iTHEMBA LABS

In this section, several uncertainty budgets for different experiments undertaken at iThemba LABS are presented.

An uncertainty budget is not presented for each stopping power measurement (i.e. for each ion–target combination), because in many cases they are very similar. Representative cases are given in detail.

5.3.1. Stopping power of Si_3N_4 for 3.6–8.7 MeV silicon

This uncertainty budget is for the energy loss measurement made at iThemba LABS for the 100 nm Si_3N_4 membrane for silicon in the energy range of 3.6–8.7 MeV. The corresponding uncertainty budget for the areal density was

given in Section 5.2.1. This uncertainty budget is representative of the different experiments with other ions.

The uncertainty of the energy at which the stopping power is determined is given in Table 22. One particularity is that the experiment is not for one single beam energy, but for a wide range of energies, and the uncertainty is not constant. It must be calculated for each energy.

First, the uncertainty in the calibration of the magnet or system is taken as the width of the resonances used (around 1 keV at 5.802 MeV for the $^{27}Al(p, n)^{27}Si$ reaction, or 0.017%). A 10 keV beam and system energy spread are then included, as is another 10 keV attributable to the estimation of the energy of the transmitted beam. Part of this 10 keV comes from the timing uncertainty in the TOF system, as detailed in Section 5.3.2, and it includes the uncertainty in the flight path length. The uncertainty in the scattering angle leads to an uncertainty in the initial beam energy via the kinematic factor of the recoil produced by the primary beam.

Finally, the term attributable to the energy loss in the foil changes from 109 keV at 3.6 MeV to 150 keV at 8.7 MeV.

The calculations were made for the entire energy range, and the results are shown in Fig. 31. The solid line shown is a fit to the data that can be used as the uncertainty for any energy within the range of the experiment.

The uncertainty budget for the actual stopping power values is given in Table 23 and is shown in Fig. 32.

TABLE 22. UNCERTAINTY BUDGET FOR ENERGY AT WHICH STOPPING POWER IS DETERMINED FOR SILICON ON Si_3N_4 (iTHEMBA LABS)

Source of uncertainty	Uncertainty
Beam and system energy spread	10 keV
Uncertainty in estimation of energy of transmitted beam	10 keV
Total energy loss in the foil (divided by 2.35 to obtain sigma)	Variable with energy 109 keV at 3.6 MeV to 150 keV at 8.7 MeV
Standard uncertainty (precision)	Variable with energy 109 keV at 3.6 MeV to 150 keV at 8.7 MeV
Beam energy: uncertainty in calibration of magnet or system	0.017%
Scattering angle	0.32%
Total combined standard uncertainty (accuracy)	Variable with energy 110 keV at 3.6 MeV to 152 keV at 8.7 MeV

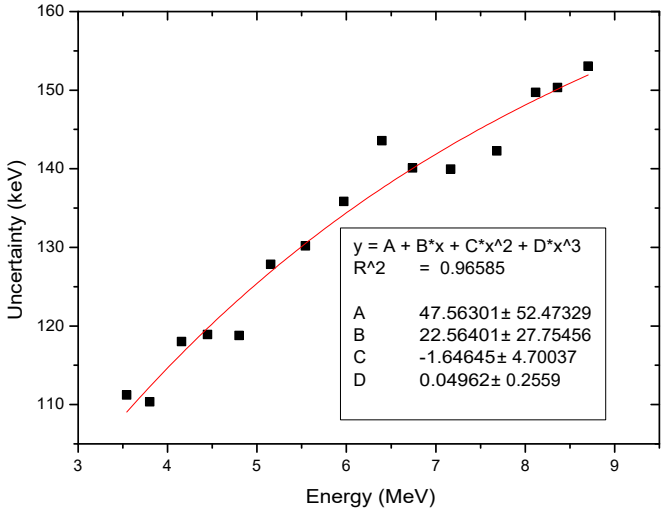

FIG. 31. iThemba LABS: Total uncertainty in the determination of the energy at which the stopping power values were determined for the 100 nm Si_3N_4 membrane.

TABLE 23. UNCERTAINTY BUDGET FOR DETERMINATION OF STOPPING POWER FOR SILICON ON Si_3N_4 (iTHEMBA LABS)

Source of uncertainty	Uncertainty
Beam and system energy spread	10 keV
Uncertainty in estimation of energy of transmitted beam	10 keV
Standard uncertainty (precision)	5.5% at 3.6 MeV to 4.0% at 8.7 MeV
Uncertainty in areal density of foil	3.1%
Total combined standard uncertainty (accuracy)	6.3% at 3.6 MeV to 5.1% at 8.7 MeV

5.3.2. Stopping power of Al_2O_3 for 3.9–17.2 MeV silicon

The stopping power of Al_2O_3 for 3.9–17.2 MeV silicon was measured at iThemba LABS. This section details how the uncertainty of the measurement was determined. The sample used was not the sample that was characterized at the

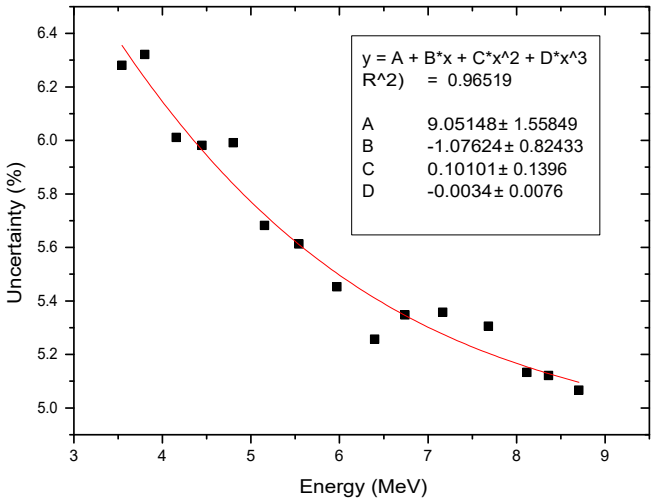

FIG. 32. iThemba LABS: Total uncertainty in the determination of the Si_3N_4 stopping power for silicon.

Munich Q3D magnetic spectrograph, for which the uncertainty budget was given in Section 5.2.2; it was the sample prepared at iThemba LABS, as described in Section 4.4.

In this case, the areal density was measured by RBS with a 1.60 MeV $^4He^{2+}$ beam. The spectrum collected is shown in Fig. 33, together with a simulation made with the code SIMNRA [26], which took part in the IAEA intercomparison of IBA software [3].

The uncertainty budget for the areal density of the foil is given in Table 24. The foil roughness was measured with AFM (Fig. 28). The 1% thickness non-uniformity value was provided by the manufacturer.

The beam energy spread and energy calibration influence the result via the scattering cross-section. An uncertainty in the beam energy of 2 keV leads to a 0.25% uncertainty in the Rutherford cross-section.

The counting statistics were calculated for the total yield of each signal, taking the backgrounds into account. The combined uncertainty is the uncertainty for the aluminium and oxygen signals, weighted by their concentrations.

The electronics calibration uncertainty influences the result via the gain used in the analysis, which leads to a different energy scale, affecting the cross-section in deeper layers of the foil. If the pulse height defect of the detector is not explicitly taken into account, an accuracy in the gain better than 1% cannot normally be obtained [58]; this situation leads to an uncertainty in the calculated yield of around 0.1%.

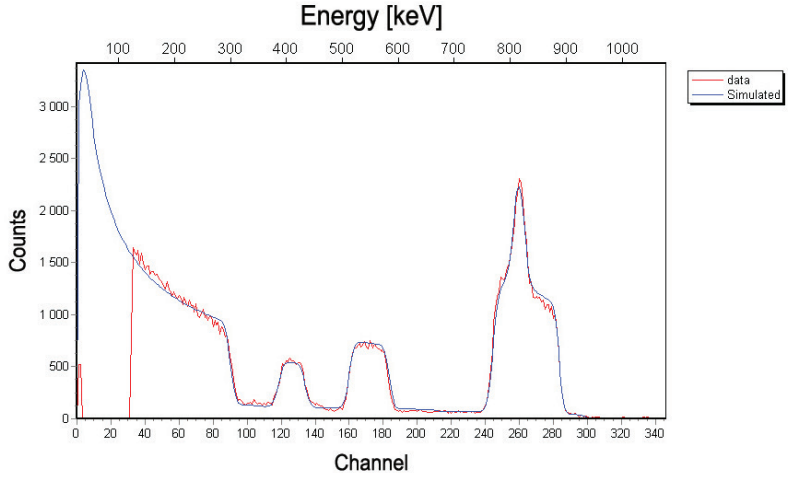

FIG. 33. Rutherford backscattering spectroscopy spectrum of the Al_2O_3 on Si_3N_4 foil with a SIMNRA simulation overlay. (Reproduced courtesy of iThemba LABS.)

TABLE 24. UNCERTAINTY BUDGET FOR DETERMINATION OF THE Al_2O_3 FOIL AREAL DENSITY (iTHEMBA LABS)

Source of uncertainty	Uncertainty (%)
Foil surface roughness	0.5
Foil thickness non-uniformity	1
Beam energy calibration and spread	0.25
Counting statistics: oxygen signal	0.90
Counting statistics: aluminium signal	0.64
Counting statistics: combined	0.80
Electronics calibration uncertainty	0.1
Standard uncertainty (precision)	1.4
^{4}He in Al_2O_3 stopping power uncertainty	4.3
Scattering angle	0.12
Detector resolution	1
Code uncertainty	0.21
Rutherford cross-section	0.17
Total combined standard uncertainty (accuracy)	4.6

The stopping power uncertainty was taken to be half the spread in experimental data for this system at the stopping maximum [64].

The detector resolution affects the result because the aluminium and silicon signals are heavily superimposed onto each other, and to distinguish one from the other requires an extremely precise fitting of the interface between the two signals. Even a small change in the detector resolution can lead to significant changes in the areal density determined, as shown in the chapter on pitfalls of the Handbook of Modern Ion Beam Analysis [58].

The scattering angle affects the scattering cross-section. An uncertainty of 0.2% in the angle was considered.

The code uncertainty is the value obtained in the IAEA intercomparison of IBA software for ^{4}He RBS [3].

The calculations of electron screening are not completely accurate, and different models lead to slightly different cross-sections. This was shown in Fig. 29 for a 150 MeV ^{127}I beam on Si_3N_4. Similar calculations were made for 1.6 MeV ^{4}He.

It is clear that the final uncertainty is dominated by systematic factors, in particular the contribution of the uncertainty of the ^{4}He stopping power for Al_2O_3. Collecting more data or having better statistics would not lead to a significant improvement of the results.

The uncertainty budget for the energy at which the stopping power values are determined is given in Table 25. The uncertainty depends on the energy, so the example given is for one of the lowest initial beam energies, 5.67 MeV.

The uncertainties given for the energy as measured with and without the sample (E_1 and E_2) are attributable to the fit error of the time signals, as shown in Fig. 34. The time signals can be fitted with an error of around 0.05 ns, which is excellent considering that the spacing between points is one order of magnitude larger than that. The resulting timing uncertainty in the energy is around 0.1%.

The energy loss in the Si_3N_4 membrane can be calculated for the exit energy. However, there is a non-negligible energy loss in the membrane, and the stopping power is not constant. One alternative might be to calculate the energy loss for the stopping power at the top of the membrane or for the average energy of the beam in the membrane.

The energy loss in the Si_3N_4 membrane leads to two more components in the budget. One is attributable to the uncertainty in the Si_3N_4 stopping power for silicon, and the other is attributable to the uncertainty in the Si_3N_4 areal density.

Finally, the scattering angle also contributes to the uncertainty.

This procedure was repeated for two more points, one in the mid-energy range and one in the high energy range. The results are shown in Fig. 35. The fitted function allows the determination of the uncertainty in the entire energy range.

TABLE 25. UNCERTAINTY BUDGET FOR ENERGY AT WHICH STOPPING POWER IS DETERMINED FOR SILICON ON Al_2O_3 (iTHEMBA LABS)

Source of uncertainty	Uncertainty
Beam and system energy spread	10 keV
Uncertainty in E_1 (from Gaussian fit)	8.2 keV (0.14%)
Uncertainty in E_2 (from Gaussian fit)	4.6 keV (0.09%)
Total energy loss in the foil (divided by 2.35 to get sigma)	179 keV
Standard uncertainty (precision)	179 keV
Beam energy: uncertainty in calibration of magnet or system	0.017% (1 keV at 5.7 MeV)
Uncertainty of energy loss in Si_3N_4 attributable to energy at which stopping is calculated	4 keV
Uncertainty of energy loss in Si_3N_4 attributable to uncertainty of Si_3N_4 stopping power	17.3 keV (5.9% of 293 keV lost in Si_3N_4)
Uncertainty of energy loss in Si_3N_4 attributable to uncertainty of Si_3N_4 areal density	9.1 keV (3.1% of 293 keV lost in Si_3N_4)
Scattering angle	0.32% (18.1 keV at 5.7 MeV)
Total combined standard uncertainty (accuracy)	181 keV at 5.672 MeV

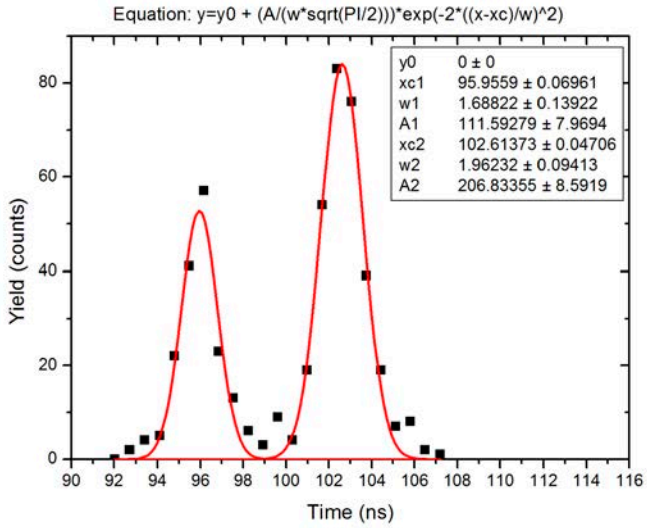

FIG. 34. iThemba LABS: Fitting of the time signal for an initial beam energy of 5.67 MeV for the Al_2O_3 foil on Si_3N_4.

The uncertainty budget for the actual stopping power values is given in Table 26. The uncertainty depends on energy, so the example given is for an initial beam energy of 5.67 MeV.

Several of the components were already present in the uncertainty budget for the energy at which the stopping power is determined. The reason is that any uncertainty in the energy lost in the film affects both the average energy of the beam inside the film and the calculation of stopping power.

Thus, the precision of the measurement is given by the beam and system energy spread, and by the uncertainty in the determination of the energy before and after crossing the foil. This is in total (adding the three terms in quadrature) 13.7 keV or 3.3% of the 420 keV energy loss in the Al_2O_3 foil.

The uncertainties in the calibration of the magnet and of the scattering angle do not contribute, in first order, to the uncertainty in the stopping power, because they lead to the same difference in the energy of the beam, both with and without the foil.

The uncertainty in the energy lost in the Si_3N_4 is, however, propagated to the uncertainty of the energy lost in the Al_2O_3 foil and, therefore, to the stopping power determined.

Two main factors affect the calculation of the energy lost in the Si_3N_4 membrane. The first is the uncertainty in its areal density, which was calculated as 3.1% in Section 5.2.1. For a calculated energy loss in the Si_3N_4 membrane

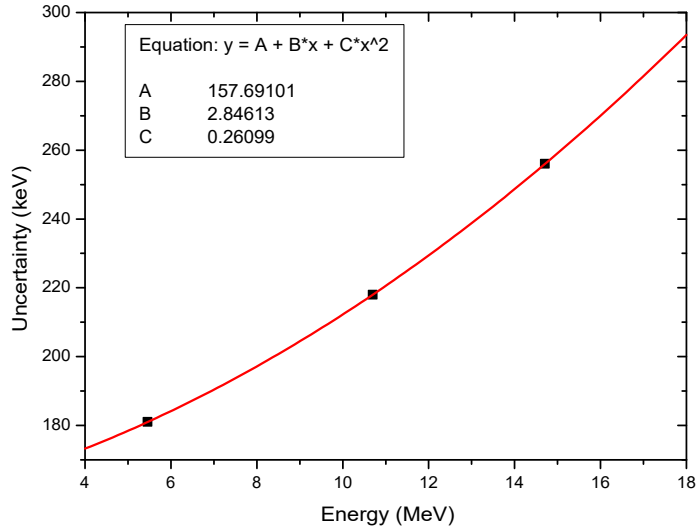

FIG. 35. iThemba LABS: Total uncertainty in the determination of the energy at which the stopping power values were determined for the Al_2O_3 foil on Si_3N_4.

TABLE 26. UNCERTAINTY BUDGET FOR DETERMINATION OF STOPPING POWER FOR SILICON ON Al_2O_3 (iTHEMBA LABS)

Source of uncertainty	Uncertainty
Beam and system energy spread	10 keV
Uncertainty in E_1 (from Gaussian fit)	8.2 keV (0.14%)
Uncertainty in E_2 (from Gaussian fit)	4.6 keV (0.09%)
Standard uncertainty (precision)	3.3%
Uncertainty of energy loss in Si_3N_4 attributable to energy at which stopping is calculated	4 keV
Uncertainty of energy loss in Si_3N_4 attributable to uncertainty of Si_3N_4 stopping power	17.3 keV (5.9% of 293 keV lost in Si_3N_4)
Uncertainty of energy loss in Si_3N_4 attributable to uncertainty of Si_3N_4 areal density	9.1 keV (3.1% of 293 keV lost in Si_3N_4)
Uncertainty in areal density of Al_2O_3	4.6%
Total combined standard uncertainty (accuracy)	7.35%

of 293 keV, this is 9.1 keV. The second is that the stopping power of Si_3N_4 for silicon has an uncertainty of 5.9%, as calculated in Section 5.3.1. This amounts to 17.3 keV. Finally, there is a smaller 4 keV component, from the uncertainty of energy loss in Si_3N_4 attributable to the energy at which stopping is calculated. This adds up to 20 keV or 4.7% of the 420 keV energy loss in the Al_2O_3 foil.

Finally, the last term is the uncertainty of the Al_2O_3 areal density, which is 4.6% as calculated above.

The total combined uncertainty is then 7.35%. Comparing this value to the precision of the experiment, 3.3%, it is clear that it is systematic sources of uncertainty that dominate the accuracy of the final result. A lower uncertainty cannot be obtained by improving the precision of the experiment, for instance by improving the accuracy of the time and energy detection system, or by a more accurate calibration of the accelerator. The only way to significantly improve the final accuracy is to have a more accurate value for the stopping power of Si_3N_4, as well as a more accurate value for the areal density of the Si_3N_4. This reflects the fact that a self-sustaining Al_2O_3 foil with an appropriate thickness is very difficult to obtain and, thus, needs to be deposited onto the Si_3N_4 membrane. Even with a very careful experiment, as reported here, this leads to the sizeable uncertainty calculated.

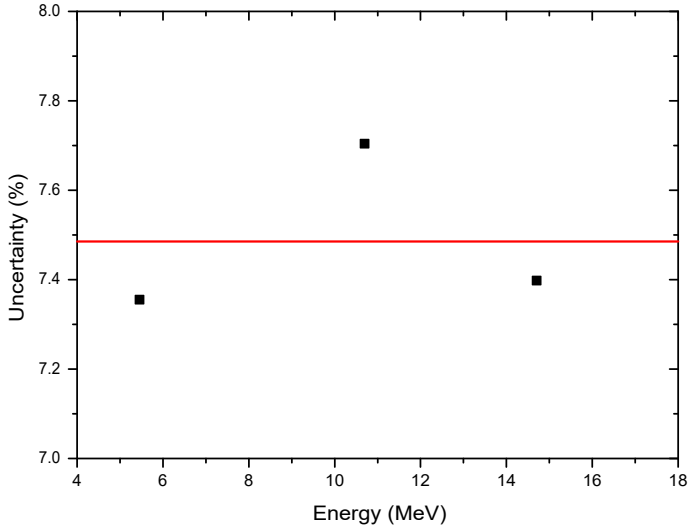

FIG. 36. iThemba LABS: Total uncertainty in the determination of the Al_2O_3 stopping power for silicon. The line is the average of the three points.

This procedure was repeated for two more points, one in the mid-energy range and one in the high energy range. The results are shown in Fig. 36. The differences are small and mainly caused by the fitting of the time signals, which have varying fit errors. The line is the average of the three points, around 7.5%, which can be taken for the entire energy range.

5.4. MEASUREMENTS MADE AT THE UNIVERSITY OF HELSINKI

The measurements made at the University of Helsinki provide a continuous stopping power curve, based on a transmission experimental method. However, the data analysis is undertaken in a different way to the other groups that used thin foils in transmission geometry, because it is based on a fitting method, as outlined in Section 2.4.3. In particular, a truly continuous stopping power curve is obtained because it is a continuous curve that is fitted.

In this case, it makes no sense to calculate an uncertainty at which each stopping value is determined. The uncertainty of the beam energy instead has an influence on the uncertainty of the actual values of the stopping power, through the dependence of the stopping power on the beam energy. Where the stopping power changes rapidly with energy, an uncertainty in the energy leads to a comparatively large uncertainty in the stopping power; where the stopping power

is nearly constant, the uncertainty in the energy has practically no effect on the uncertainty in the stopping power.

5.4.1. Stopping power of Si_3N_4 for carbon

The stopping power of Si_3N_4 for carbon was measured at the University of Helsinki. This section details how the uncertainty in the stopping power attributable to the uncertainty in the beam energy was calculated. This is shown in Table 27. The uncertainty in the actual beam energy that comes from the beam energy spread plus the calibration of the Tandem, plus any energy drift, can be considered as 5 keV.

The uncertainty from the time resolution is 1% for low energies and 2% for high energies in the energy range of 0.6–13 MeV. There are several causes, such as the difference between the mode, median and mean, as well as the fitting process itself. A simple linear interpolation between those two time resolution uncertainty values was made. The uncertainty in the determination of the TOF propagates to the energy of the beam with and without foil; it is a few kiloelectronvolts in each case, with values depending on the beam energy.

The uncertainty in the calibration of the magnet is 0.05%. A 0.15º uncertainty in the 40º recoil angle leads to a ≈0.05% uncertainty in the kinematic factor, which is very small. There is a further 0.29% uncertainty from the 2 mm in 684 mm uncertainty of the flight distance, *d*.

The result is given in Fig. 37 as a function of the beam energy. The dominating term is the uncertainty in the flight distance.

The energy lost in the Si_3N_4 is shown in Fig. 38, and its derivative is shown in Fig. 39. For instance, at 2 MeV, it is 13.8 keV/MeV. Thus, a 10.6 keV uncertainty in the beam energy leads to an uncertainty of $13.8 \times 0.0106 = 0.15$ keV in the energy loss at that energy, which is 219 keV, or a 0.07% uncertainty in the stopping power determined. This calculation can be made for all energies, and the result is the uncertainty in the stopping power attributable to the uncertainty in the beam energy as a function of energy, which is shown in Fig. 40. It is clear that this contribution is only significant at low energies and, even then, it is small.

Then, the uncertainty in the energy determination was considered, again 5 keV for the beam energy spread, plus the uncertainty stemming from the time resolution. This step does not mean that these factors were considered twice. In the paragraph above, the influence of beam energy spread and time resolution on the stopping power uncertainty, attributable to the energy at which the stopping power is calculated, was estimated, and it was concluded that it was not significant. Now, the uncertainty in the actual energy lost by the beam in the foil is considered. As a percentage of the energy lost in the foil, this is significant, as shown in Fig. 41.

The dashed curve in Fig. 42, which can be considered to be the precision of the experiment, was obtained by adding the uncertainty of the actual energy lost by the beam in the foil to the contribution of the uncertainty of the energy at which the stopping power is determined (Fig. 40). However, the process of fitting the stopping power curve also has an associated uncertainty, coming from the fit itself

TABLE 27. UNCERTAINTY BUDGET FOR ENERGY FOR CARBON ON Al_2O_3 (UNIVERSITY OF HELSINKI)

Source of uncertainty	Uncertainty
Beam and system energy spread	5 keV
Uncertainty in E_1	3.8 keV at 5 MeV
Uncertainty in E_2	3.8 keV at 5 MeV
Standard uncertainty (precision)	7.3 keV
Beam energy: uncertainty in calibration of magnet or system	0.05%
Recoil angle (0.15º in 40º)	0.05%
Flight distance, *d* (2 mm in 684 mm)	0.29%
Total combined standard uncertainty (accuracy)	16.7 keV at 5 MeV

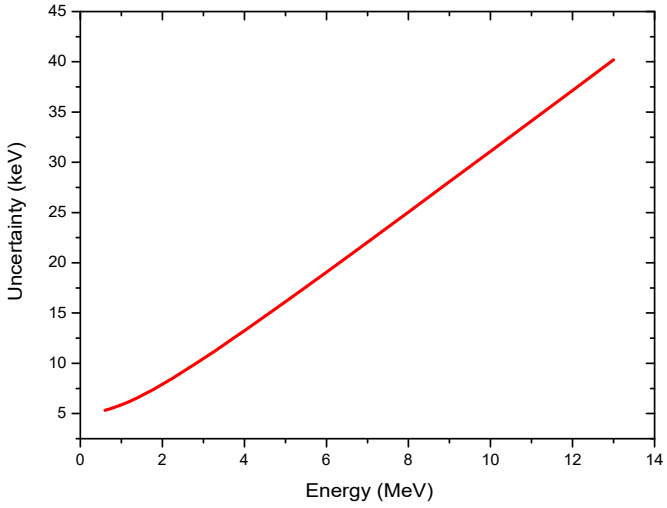

FIG. 37. University of Helsinki: Uncertainty in the beam energy of a ^{12}C beam on Si_3N_4.

and from the shape of the curve that is used. This error is estimated as 3%, and the solid line shown in Fig. 42 is obtained by adding this value to the previous curve. This is the final standard uncertainty, and it considers all sources of uncertainty.

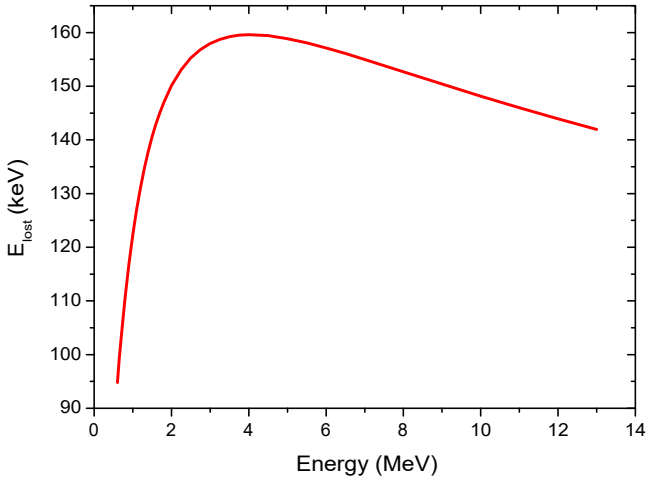

FIG. 38. University of Helsinki: Energy lost by a ^{12}C beam on Si_3N_4.

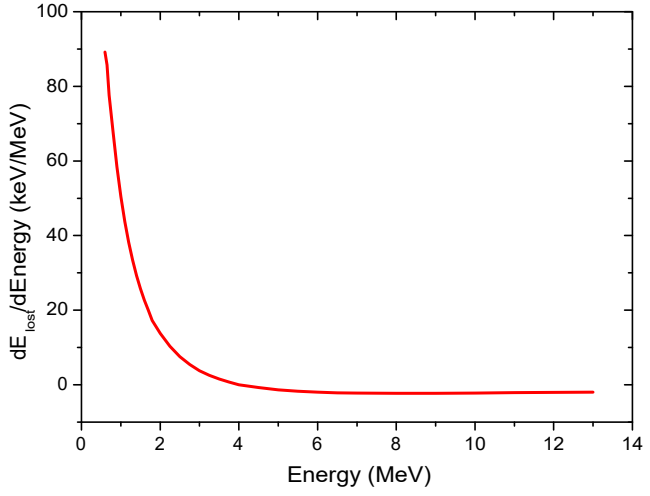

FIG. 39. University of Helsinki: Derivative of energy lost by a ^{12}C beam on Si_3N_4 with respect to the beam energy.

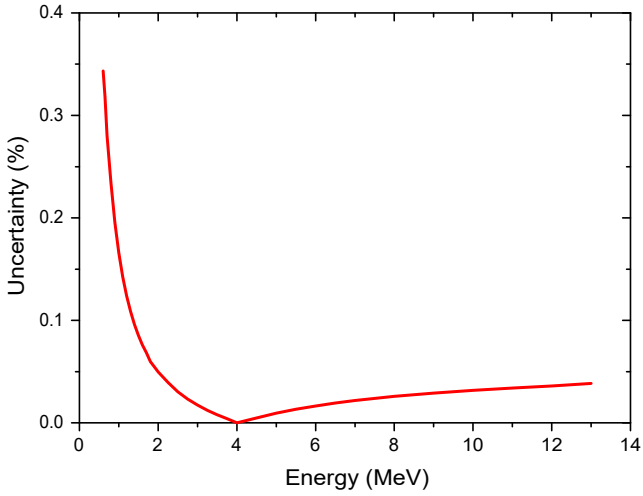

FIG. 40. University of Helsinki: Uncertainty in the stopping power of Si_3N_4 for ^{12}C attributable to the uncertainty in the energy at which the stopping is calculated.

5.4.2. Stopping power of Al_2O_3 for carbon

The stopping power of Al_2O_3 for carbon was measured at the University of Helsinki. This section details how the uncertainty of the measurement was determined. The main difference from the previous case is that the uncertainty in the energy lost in the Si_3N_4 membrane contributes to the uncertainty in the stopping power measured. As the Si_3N_4 membrane is thicker than the Al_2O_3 foil, a small relative uncertainty in the energy loss in the Si_3N_4 membrane leads to a sizeable absolute uncertainty, which is a large fraction of the energy loss in the Al_2O_3 foil.

A simple estimate of this effect can easily be made. Between 1 and 13 MeV, the stopping powers of Si_3N_4 and Al_2O_3 for carbon, as calculated with SRIM, are equal within 3%. Therefore, the ratio between the energy lost in the Si_3N_4 and in the Al_2O_3 is simply given by the ratio of their areal densities, which according to Table 7 is 1.53. That is, a 1% uncertainty in the energy lost in the Si_3N_4 leads to a 1.53% uncertainty in the energy lost in the Al_2O_3.

Following the procedure outlined in Section 5.4.1, the uncertainty of the stopping power of Al_2O_3 for ^{12}C is derived, including the uncertainty in the energy loss in the Si_3N_4 membrane, and is shown in Fig. 43.

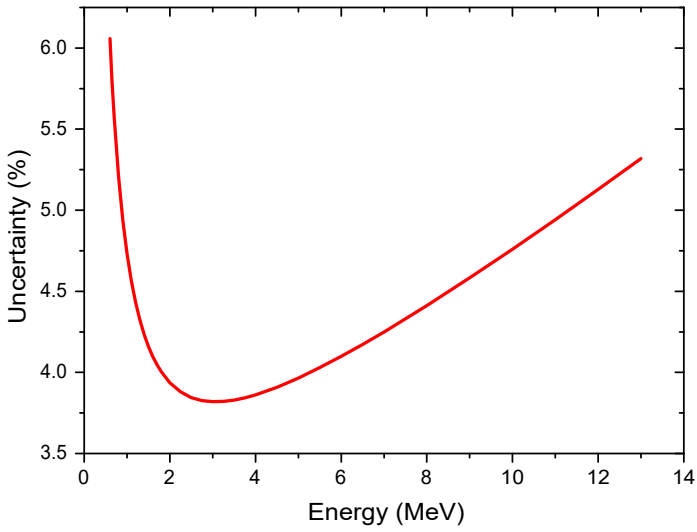

FIG. 41. University of Helsinki: Uncertainty in the stopping power of Si_3N_4 for ^{12}C attributable to the uncertainty in the energy lost by the beam in the foil.

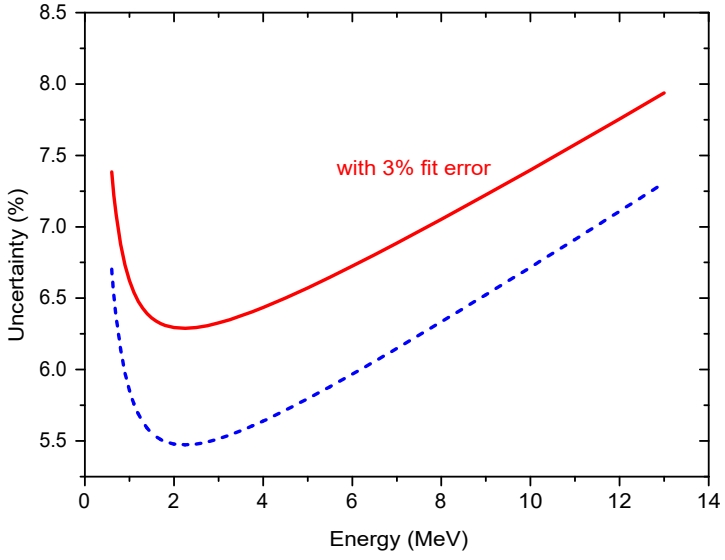

FIG. 42. University of Helsinki: Accuracy of the stopping power of Si_3N_4 for ^{12}C.

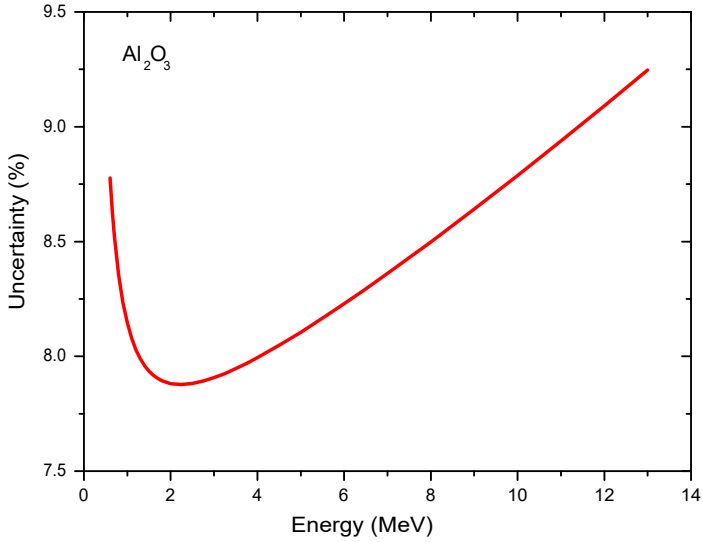

FIG. 43. University of Helsinki: Accuracy of the stopping power of Al_2O_3 for ^{12}C.

5.5. MEASUREMENTS MADE AT THE UNIVERSITY OF JYVÄSKYLÄ

In this section, several uncertainty budgets for different experiments made at the University of Jyväskylä are presented.

An uncertainty budget is not presented for each stopping power measurement (i.e. for each ion–target combination), because in many cases they are very similar. Representative cases are given in detail.

5.5.1. Stopping power of Si_3N_4 for 0.2–8.2 MeV carbon

The stopping power of Si_3N_4 for carbon was measured at the University of Jyväskylä. This section details how the uncertainty of the measurement was determined. This uncertainty budget is for the energy loss measurement made at the University of Jyväskylä for a 100 nm Si_3N_4 membrane for carbon in the energy range of 0.2–8.2 MeV. The corresponding uncertainty budget for the areal density was given in Section 5.2.1. This uncertainty budget is representative of the different experiments with other ions.

The uncertainty of the energy at which the stopping power is determined is given in Table 28 for a 4.91 MeV beam energy. The experiment is not for one single beam energy but for a wide range of energies, and the uncertainty is not constant. It must be calculated for each energy.

TABLE 28. UNCERTAINTY BUDGET FOR ENERGY AT WHICH STOPPING POWER IS DETERMINED FOR CARBON ON Si_3N_4 (UNIVERSITY OF JYVÄSKYLÄ)

Source of uncertainty	Uncertainty
System energy spread	5 keV
Terminal voltage uncertainty, 2 kV	4 keV at 4.91 MeV
Uncertainty in estimation of energy of beam	3.6 keV at 4.91 MeV
Total energy loss in the foil (divided by 2.35 to obtain sigma)	Variable with energy 65 keV at 4.91 MeV
Standard uncertainty (precision)	Variable with energy 65 keV at 4.91 MeV
Beam energy: uncertainty in calibration of magnet or system	0.33%
Scattering angle	0.91%
Flight path length	0.32%
Total combined standard uncertainty (accuracy)	Variable with energy 82 keV at 4.91 MeV

First, the uncertainty in the calibration of the magnet or system was taken as the width of the resonance used (around 10 keV at 3.04 MeV for the $^{16}O(\alpha, \alpha)^{16}O$ reaction, or 0.33%). This is a systematic uncertainty. In these experiments, a system energy spread of 5 keV was considered. A terminal voltage uncertainty of 2 kV was then included. The uncertainty in the beam energy depends on the charge state, so it increases for higher energies.

The uncertainty in the estimation of the energy of the transmitted beam was calculated by fitting all the energy signals with and without the Si_3N_4 membrane. A joint half Gaussian function was used, and both the fit error and the difference in calculated mean and mode of the distributions were considered.

The uncertainty in the scattering angle led to an uncertainty in the initial beam energy via the kinematic factor of the recoil produced by the primary beam. An uncertainty of 1 mm in the d = 623 mm flight path length was considered. The calculations were made for the entire energy range, and the results are shown in Fig. 44.

The uncertainty budget for the determination of the Si_3N_4 stopping power for ^{12}C ions, as measured at the University of Jyväskylä, is given in Table 29 for a 4.91 MeV beam energy and is shown in Fig. 45.

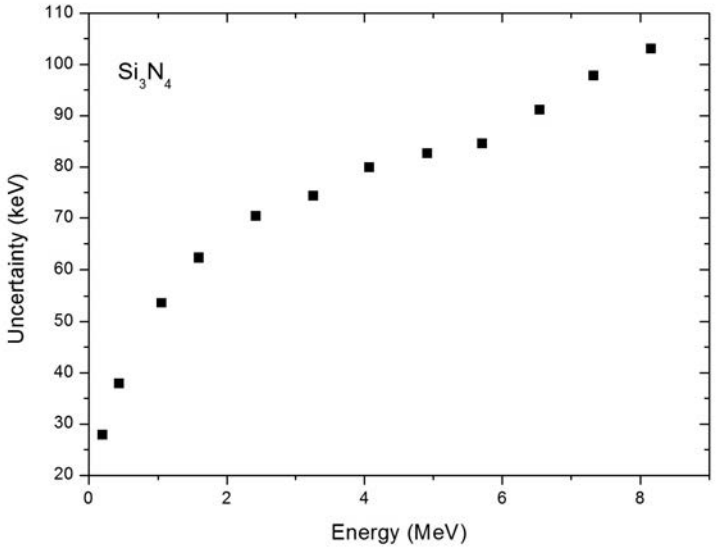

FIG. 44. University of Jyväskylä: Total uncertainty in the determination of the energy at which the stopping power values were determined for the 100 nm Si_3N_4 membrane.

TABLE 29. UNCERTAINTY BUDGET FOR DETERMINATION OF STOPPING POWER FOR CARBON ON Si_3N_4 (UNIVERSITY OF JYVÄSKYLÄ)

Source of uncertainty	Uncertainty
System energy spread	5 keV
Terminal voltage uncertainty, 2 kV	4 keV at 4.91 MeV
Uncertainty in estimation of energy of beam	3.6 keV at 4.91 MeV
Standard uncertainty (precision)	Variable with energy 3.5% (7.3 keV) at 4.91 MeV
Uncertainty in areal density of foil	3.1%
Total combined standard uncertainty (accuracy)	Variable with energy 5.7% at 4.91 MeV

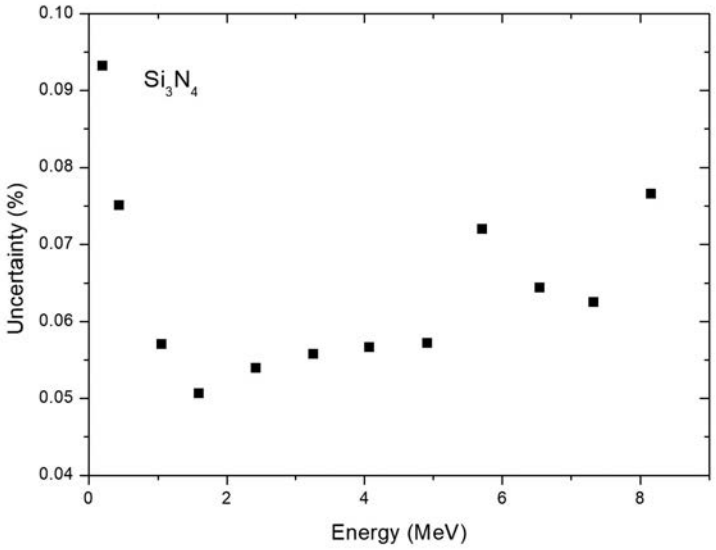

FIG. 45. University of Jyväskylä: Uncertainty in the stopping power values for carbon in the 100 nm Si_3N_4 membrane.

The beam and system energy spread, as well as the uncertainty in the estimation of the energy of the beam, led to an uncertainty in the energy loss. Together they totalled 7.3 keV, which was 4.8% of the 153.4 keV energy loss.

Then, the uncertainty of the areal density of the membrane was included, leading to a final total combined uncertainty of 5.7% at 4.91 MeV.

5.5.2. Stopping power of Al_2O_3 for 0.2–8.2 MeV carbon

The stopping power of Al_2O_3 for carbon was measured at the University of Jyväskylä. This section details how the uncertainty of the measurement was determined. This uncertainty budget is for the energy loss measurement made at the University of Jyväskylä for the Al_2O_3 foil (deposited on the Si_3N_4 membrane) for carbon in the energy range 0.5–6.5 MeV. The corresponding uncertainty budget for the areal density was given in Section 5.2.2. This uncertainty budget is representative of the different experiments with other ions.

The uncertainty budget for the energy at which the stopping power is determined is given in Table 30. It has all the terms already included in the uncertainty budget for the Si_3N_4 membrane given in Table 28, but calculated for Al_2O_3 where appropriate. It has extra terms because of the uncertainty of the energy loss in the Si_3N_4 membrane.

TABLE 30. UNCERTAINTY BUDGET FOR ENERGY AT WHICH STOPPING POWER IS DETERMINED FOR CARBON ON Al_2O_3 (UNIVERSITY OF JYVÄSKYLÄ)

Source of uncertainty	Uncertainty
System energy spread	5 keV
Terminal voltage uncertainty, 2 kV	4 keV at 4.9 MeV
Uncertainty in estimation of energy of beam	2.1 keV at 4.9 MeV
Total energy loss in the foil (divided by 2.35 to obtain sigma)	Variable with energy 41 keV at 4.9 MeV
Standard uncertainty (precision)	Variable with energy 65 keV at 4.9 MeV
Beam energy: uncertainty in calibration of magnet or system	0.33%
Scattering angle	0.91%
Flight path length	0.32%
Uncertainty of energy loss in Si_3N_4 attributable to energy at which stopping is calculated	2 keV
Uncertainty of energy loss in Si_3N_4 attributable to uncertainty of Si_3N_4 stopping power	5 keV
Uncertainty of energy loss in Si_3N_4 attributable to uncertainty of Si_3N_4 areal density	4.5 keV
Total combined standard uncertainty (accuracy)	Variable with energy 65 keV at 4.9 MeV

The energy loss in the Si_3N_4 membrane can be calculated for the exit energy. However, there is a non-negligible energy loss in the membrane, and the stopping power is not constant. One alternative might be to calculate the energy loss for the stopping power at the top of the membrane, or for the average energy of the beam in the membrane.

The energy loss in the Si_3N_4 membrane leads to two more components in the budget. One is attributable to the uncertainty in the Si_3N_4 stopping power for silicon and the other is attributable to the uncertainty in the Si_3N_4 areal density.

The calculations were made for the entire energy range, and the results are shown in Fig. 46.

The uncertainty budget for the determination of the Al_2O_3 stopping power for ^{12}C ions, as measured at the University of Jyväskylä, is given in Table 31 for 4.9 MeV beam energy and is shown in Fig. 47. Most of the components that

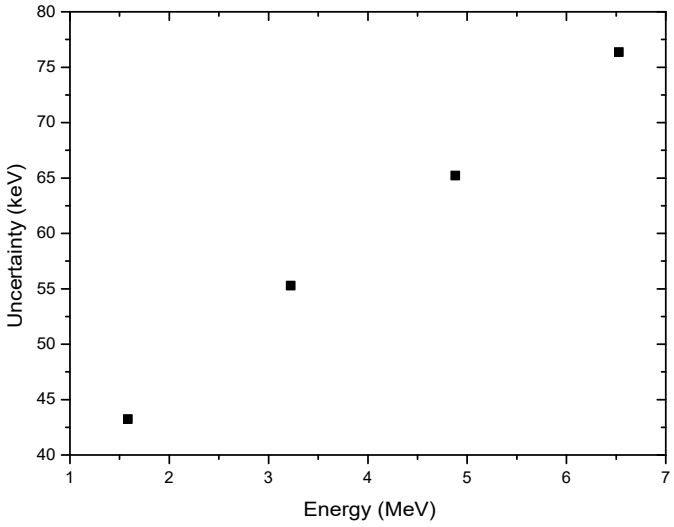

FIG. 46. University of Jyväskylä: Total uncertainty in the determination of the energy at which the stopping power values were determined for the Al_2O_3 foil.

TABLE 31. UNCERTAINTY BUDGET FOR DETERMINATION OF STOPPING POWER FOR CARBON ON Al_2O_3 (UNIVERSITY OF JYVÄSKYLÄ)

Source of uncertainty	Uncertainty
System energy spread	5 keV
Terminal voltage uncertainty, 2 kV	4 keV at 4.9 MeV
Uncertainty in estimation of energy of beam	2.1 keV at 4.9 MeV
Standard uncertainty (precision)	Variable with energy 9.0% (6.7 keV) at 4.9 MeV
Uncertainty in areal density of foil	3.2%
Uncertainty of energy loss in Si_3N_4 attributable to energy at which stopping is calculated	2 keV
Uncertainty of energy loss in Si_3N_4 attributable to uncertainty of Si_3N_4 stopping power	5 keV
Uncertainty of energy loss in Si_3N_4 attributable to uncertainty of Si_3N_4 areal density	4.5 keV
Total combined standard uncertainty (accuracy)	Variable with energy 12.8% at 4.9 MeV

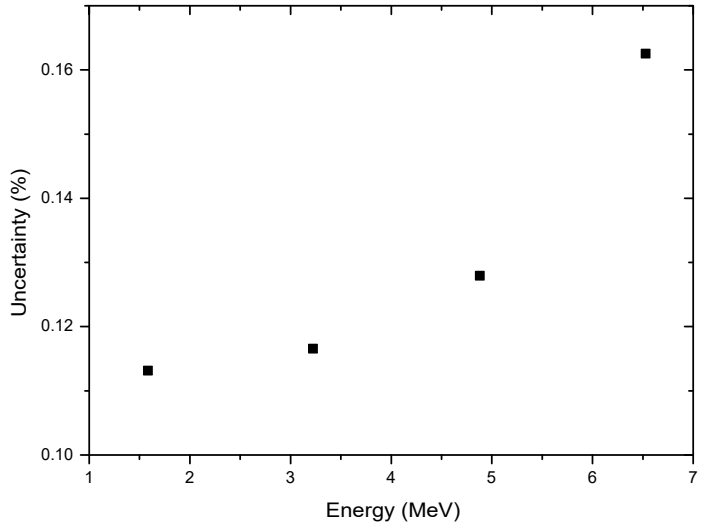

FIG. 47. University of Jyväskylä: Uncertainty in the stopping power values as determined for carbon in the Al_2O_3 foil.

contribute to the uncertainty were already present in the uncertainty budget for Si_3N_4 (see Table 29).

There are, however, further contributions to the uncertainty, coming from the uncertainty in the energy loss in the Si_3N_4 membrane. This propagates directly to the uncertainty in the energy lost in the Al_2O_3 foil. As the energy loss in the Si_3N_4 accounts for most of the total energy loss, an uncertainty of around 7% in the energy lost there leads to an uncertainty of almost 20% in the Al_2O_3 stopping power. This 7% uncertainty in the energy lost in the Si_3N_4 membrane comes mostly from the uncertainty in the Si_3N_4 stopping power, as determined in this work.

The uncertainty for the same system, measured with a similar technique at iThemba LABS, was determined to be around 7.5% (see Section 5.3.2). This lower value arises from the fact that, in that case, a different sample was used for which the Al_2O_3 areal density was much larger. The uncertainty in the energy loss in the Si_3N_4 membrane was, therefore, a much smaller fraction of the energy loss in the Al_2O_3 foil, resulting in a smaller final uncertainty in the stopping power determined.

5.6. MEASUREMENTS MADE WITH THE BULK SAMPLE METHOD

The bulk sample method was used by the Instituto Superior Técnico and Ruđer Bošković Institute groups. It is based on an analysis of RBS spectra with Bayesian inference [65] with the MCMC method, which is a valid alternative to the GUM framework of elaborating detailed uncertainty budgets [59]. A basic description of the methods used is given here. A more complete description of the application of Bayesian inference to IBA can be found in Ref. [66].

An RBS spectrum can be viewed as coming from deterministic processes, such as those involved in beam propagation, scattering and detection. These processes depend on parameters, some of which are controlled by the experimentalist, such as those relating to the experimental conditions (e.g. beam energy, scattering angle, detection system used and its characteristics). Some parameters are known from prior information, for instance, a known sample composition (e.g. pure silicon). Some of the parameters relate to quantities about which it would be of interest to learn. In this case, such a quantity is the stopping power curve $S(E)$. The RBS spectrum also contains non-deterministic components, which constitute the experimental noise.

Bayesian inference is a way to combine all these elements with the analytical simulation of RBS spectra into a single statistical model to infer information about the parameters of interest. Independent Poisson noise is assumed on the RBS yield. The stopping power curve shape is constrained to realistic values by assuming the parameterization given by Eq. (14), with a uniform unbounded distribution on the a_1–a_8 parameters.

Computation is done with an MCMC algorithm, according to the Metropolis–Hastings criterion [67]. The mean stopping power curve is calculated, as well as confidence intervals given, by the standard deviation. During the MCMC procedure, all the other parameters can vary freely within their stated uncertainties. In practice, many simulations are made, all with a different stopping power curve generated randomly, but all leading to simulations consistent with the data within the experimental uncertainties. The other parameters, such as the energy calibration, the angle of scattering, the angle of incidence, the beam energy, the system energy resolution and the beam fluence–solid angle product, also change randomly during the calculation. With this procedure, their uncertainties are propagated to the final uncertainty of the stopping power curve.

In a bulk sample, the only information that can be used to infer the stopping power is the height of the spectrum [41]; therefore, the accuracy of the beam fluence–solid angle product is directly propagated to the accuracy of the final result. In several experiments, particularly those performed with heavy ions, the beam fluence was either not known or its uncertainty was very large. Several of

the samples used in this work were actually films on a given substrate, where the energy width of the signals also provided information on the energy loss.

Nevertheless, in all cases, a thin gold layer was deposited on top of the samples. Its areal density was determined with ^{4}He RBS, in a set-up in which the beam fluence–solid angle product was known with an accuracy of 2% [68]. This value (together with other sources of uncertainty in the ^{4}He RBS experiment) is propagated to the uncertainty in the stopping powers determined from the given sample. However, in several samples, a substrate signal could be used for yield normalization. In this case, the uncertainty of the stopping power of ^{4}He in the substrate material must be propagated to the final results. This uncertainty is significantly lower than 2% in one particular case: the stopping power of silicon for ^{4}He at 1.5 MeV is known with an accuracy of 0.8% [3]. Thus, in the sample in which silicon was used as a substrate, total accuracies of the gold layer areal density of around 1% were obtained.

The method can be illustrated with one example. The data for one of the three detectors measured at the Ruđer Bošković Institute for ^{12}C in indium nitride (InN) are shown in Fig. 48, together with simulations made using SRIM stopping.

The information about the stopping power is extracted from the height and width of the indium signal. The energy calibration is the same for the 3 MeV and 6 MeV spectra, and again the same for the 10 MeV and 15 MeV spectra. The pulse height defect must be taken into account [69] because it affects both the linearity of the energy calibration and the actual height of the signals.

Clearly, the width of the indium signal, as calculated with SRIM stopping, is too small, which means that SRIM calculates an energy loss in the InN that is smaller than that observed.

A few of the stopping curves that were generated during the Bayesian inference–MCMC procedure are shown in Fig. 49. All the curves shown led to good simulations; that is, fits were consistent with the data once the experimental uncertainties were taken into account. A total of 50 000 such stopping curves were generated. The final stopping power determined was derived by calculating their average, with an uncertainty given by their standard deviation.

5.7. BEAM DAMAGE

Stopping power measurements of the same material for the same ion, and in the same energy range, frequently differ from each other by more than the stated accuracies of each experiment. This means that the actual accuracy is worse than what is thought by the experimentalists. This can happen if not all sources of accuracy are considered; often, only statistical errors are taken into account and experimental parameters, such as beam energy, detector resolution, scattering

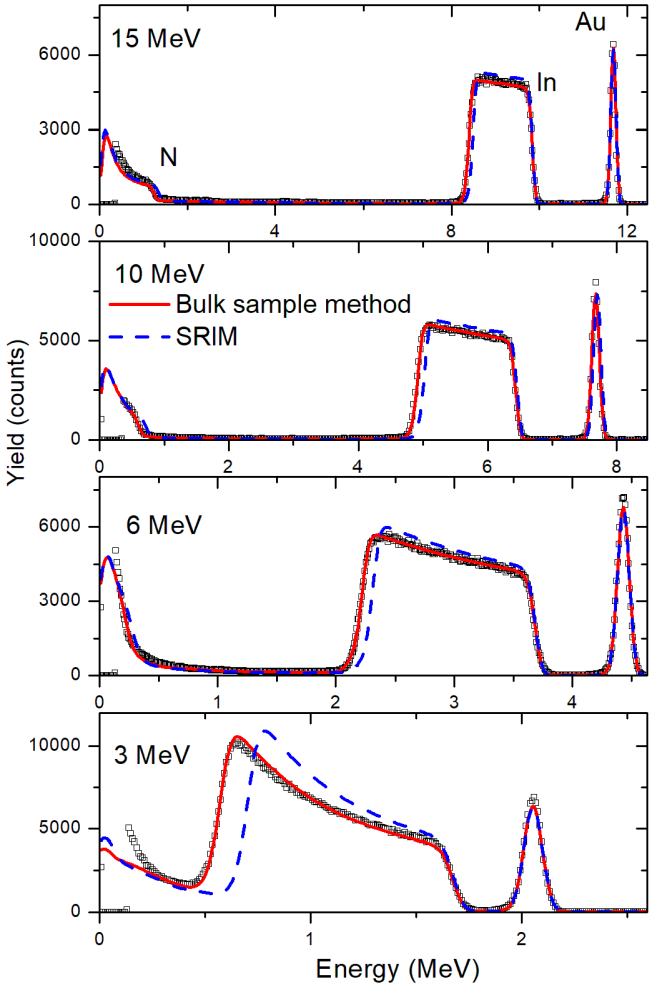

FIG. 48. Spectra collected for InN with ^{12}C with the 150° detector. Simulations using SRIM stopping (dashed) and the stopping curve determined (solid) are shown.

angle or, more generally, experimental geometry, are disregarded. It can also happen that the sample studied is not well characterized and has impurities or a different stoichiometry than what is thought. In this case, the experimental result may be correct, but it corresponds to a different material than what is stated.

One frequent source of error is the thickness or areal density of the thin foil used [28]. This error can result from the measurement of the thickness, but it can also result from beam damage; that is, during the experiment, the thickness and areal density of the foil may change. Foil contraction (i.e. the increase of the

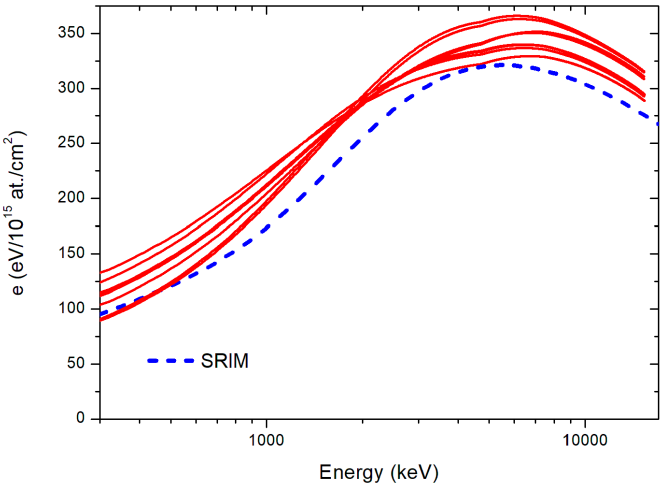

FIG. 49. Some of the 50 000 stopping curves that led to simulations consistent with the Rutherford backscattering spectroscopy data within uncertainties.

foil thickness) can happen in the beam spot. Desorption of absorbed layers at the surface of the foil also occurs. The biggest concern, however, is sputtering, defined as the removal of surface atoms as a result of energetic particle bombardment caused by collisions between the incoming particles and the atoms in the near surface layers of a solid [70].

Sputtering is a particular concern in the case of heavy ion beams, as a strong non-linear dependence of damage rate on electronic stopping power has been observed [71] and sputtering is one of the ultimate limitations for the analysis of thin layers by heavy ion ERDA [72].

The physical processes underlying sputtering are beyond the scope of this work. Here, the only concern is whether beam damage affected the samples used in the stopping power measurements. The answer is twofold. First, in the bulk sample experiments, in the cases in which bulk samples were truly used, sputtering of the sample itself did not play a role. However, in all cases, a thin gold marker layer was deposited on the surface of the samples for charge normalization purposes. If the areal density of this gold layer was not constant, the charge normalization would be incorrect. In the experiments performed, loss of gold atoms is more likely to be caused by poor adhesion of the gold layer to the surface of some of the samples used. In any case, loss of gold would be noticed as consecutive measurements were made. In fact, in two systems (Al_2O_3 and hafnium oxide), a noticeable diffusion of gold into the sample was observed and the data collected were, therefore, not used. In all other cases, the gold layer remained stable.

Second, in the transmission experiments, the beam fluence required to perform the measurements is typically several orders of magnitude lower than the beam fluence used in a heavy ion ERDA experiment. This is because the scattering cross-section for production of recoils (and of forward scattered beam particles) is very low. Consider, for instance, the heavy ion ERDA experiment reported in Section 9.2.7, undertaken with a 50 MeV ^{127}I beam, on a sample with a surface layer of 50 nm of gold. For a 1 msr solid angle, only about one gold recoil is detected for each 2.3×10^6 incident ^{127}I ions and only about one ^{127}I ion for each 0.7×10^6 incident ^{127}I ions. That is, in a transmission experiment, the total beam fluence can be kept millions of times lower than in a typical heavy ion ERDA experiment; thus, sputtering is generally not a cause for concern. Furthermore, list mode data were collected at the University of Jyväskylä and no change in the samples under the beam was found.

6. RESULTS — STOPPING CROSS-SECTIONS

This section summarizes the main results obtained. All the results reported by the laboratories involved were stopping cross-sections, which are of more general use in IBA than stopping powers.

Previous results from the literature are also shown, where available. Nevertheless, it is possible that some existing measurements have been overlooked because the literature on this subject is vast and not always easy to find. Stopping power measurements for a given system might be reported in papers about the analysis of that system, and indexing in databases can be problematic.

Even in cases in which uncertainties are reported in the original papers (often in the 3–5% range), it was chosen to present values from the literature without error bars. The reason is that, more often than not, the uncertainties quoted reflected only the statistical uncertainty, which was often only a small contribution to the total uncertainty. This fact should be clear from Section 5 of this report. Very often, systematic sources of uncertainty are overlooked in reported values [28, 40], and there are countless examples of different sets of data for the same system for which the reported values differ by much more than the respective stated accuracies.

On the contrary, a very strong and thorough effort has been made to explicitly include all sources of error in the uncertainties reported in this work. This means that deviations between reported values and, for instance, values calculated with interpolative schemes, such as SRIM, that are outside the uncertainties calculated should mean that the interpolative scheme is inaccurate for the ion–target and energy range considered.

The same reasoning means that if two experiments differ by more than their stated accuracies, it should be considered that there is something wrong with one or all of the experiments reported. However, a coverage factor $k = 1$ (one standard deviation) corresponds to a level of confidence of only 68%, and a coverage factor $k = 2$ (two standard deviations), corresponding to a confidence level of 95%, may be preferable before making definite statements.

The uncertainties for the new measurements reported are presented as error bars on both the value of the stopping cross-section and the energy value at which it is determined. For the fitting methods that determine a continuous curve (i.e. for the experiments performed at the University of Helsinki and those undertaken with the bulk sample method), two continuous lines are shown, corresponding to the average plus and minus one standard deviation.

Following the practice adopted by SRIM and MSTAR, the energy scale shown is logarithmic in all cases. Furthermore, in all cases, the results are compared with SRIM (version 2012-03) calculations. For compounds, where available, the SRIM built-in compound correction was used. In the other cases, the Bragg rule was used. Either way, the method used is always explicitly stated. For the systems where it is available, MSTAR (version 3.12) was also used to produce calculations. The molecular stopping of some compounds (such as Al_2O_3, SiO_2 and Mylar) are explicitly treated in MSTAR, and in those cases that option was used. Otherwise, the Bragg rule was used. Either way, the method used is always explicitly stated. The calculations were made using option ‘d’, which is the stopping for solids based on the data for the particular ion only.

One important point is that measurements of stopping powers determine the total stopping power, including electronic and nuclear stopping. Therefore, the calculated curves shown also include the contribution of nuclear stopping power, which is particularly important at low energies and for heavier ions. In the case of SRIM, the calculations directly yield electronic and nuclear stopping, where the latter is calculated from the ZBL universal interatomic potential (see Section 2.2). In the case of MSTAR, ZBL nuclear stopping power was calculated and added to the electronic stopping power provided by MSTAR.

First, the stopping power of elements is reported. This is followed by the stopping power of oxides, nitrides and, finally, other materials.

6.1. STOPPING CROSS-SECTION OF CARBON

The measured stopping cross-sections of carbon for several different ions are shown in Fig. 50. In this case, several previous measurements existed for all of the systems and they are also shown in the figure. Calculations made

with SRIM of the total stopping cross-section, including electronic and nuclear stopping, are also shown.

For ^{58}Ni, the new experimental results are in excellent agreement with SRIM. In the same energy range (0.65–1 MeV/nucleon), existing previous measurements yielded results higher than SRIM by 3–7%. Without a clear and full evaluation of uncertainties in those measurements, it is difficult to ascertain the significance of such differences.

For ^{63}Cu, one single point was measured, and excellent agreement with both SRIM and with previous results was again found.

Previous results from several groups for the stopping cross-section of carbon for ^{127}I indicated that SRIM seemed to underestimate the stopping cross-section at energies below 1.2 MeV/nucleon, whereas at energies between 1.2 and 1.5 MeV/nucleon, a large scatter of data points was observed. The new results presented here indicate that at 0.5 MeV/nucleon, SRIM indeed underestimates the stopping cross-section, whereas at 1.3 MeV/nucleon the new data are consistent with SRIM within the uncertainty.

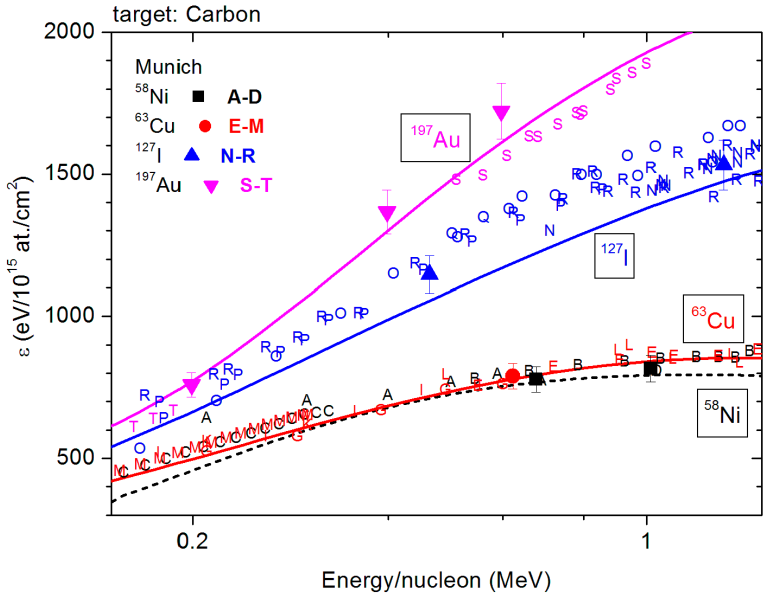

FIG. 50. Stopping cross-section of carbon for several ions. The lines are SRIM calculations (solid in all cases, except for ^{58}Ni, for which the line is dashed). The symbols with error bars are the new results reported in this publication. The letters are previous results from the literature: ^{58}Ni: A–D [73–77]; ^{63}Cu: E–M [73, 75, 76, 78–84]; ^{127}I: N–R [74, 78, 85–87]; ^{197}Au: S–T [78, 88].

Finally, for ^{197}Au ions, the new data agree with SRIM within uncertainties, even if at 0.6 MeV/nucleon the data point is slightly above the SRIM prediction. Previous data are, on the contrary, below the SRIM calculation, but it is difficult to judge whether the difference is within the uncertainty of the previous data.

6.2. STOPPING CROSS-SECTION OF OXYGEN

The stopping cross-section of oxygen for several ions is shown in Fig. 51. These results were derived from measurements of oxides, and the Bragg rule was used in the calculations. In this case, the uncertainty includes an extra 10% contribution owing to this fact. These results are shown because no data for these ion–target pairs were previously available, and even relatively inaccurate data are a significant contribution to existing knowledge. In all cases, the data are in good agreement with the SRIM prediction.

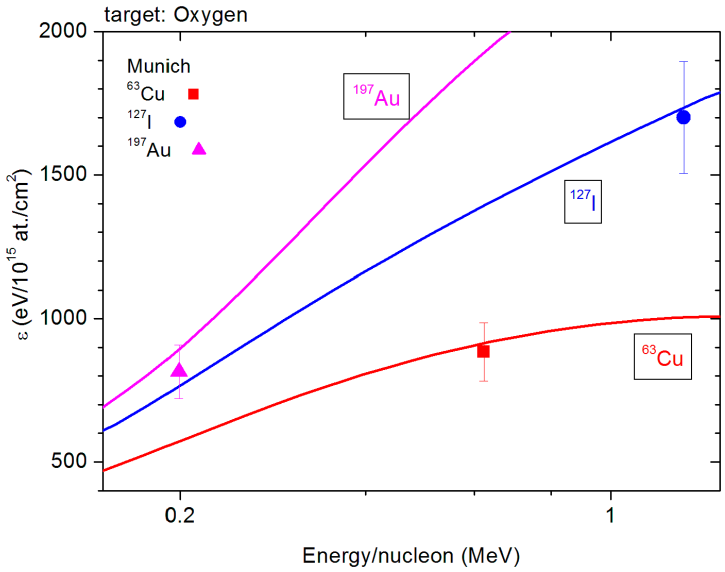

FIG. 51. Stopping cross-section of oxygen for several ions. The lines are SRIM2012 calculations. The symbols with error bars are the new results reported in this publication.

6.3. STOPPING CROSS-SECTION OF ALUMINIUM

The results obtained for aluminium are shown in Fig. 52, together with the result of previous measurements. The previous measurements all agree well with SRIM. The newly measured data, on the contrary, are all smaller than the SRIM prediction, albeit in most cases the difference is within two error bars. The SRIM calculations include both electronic and nuclear stopping (which is always the case in this work), so they are directly comparable to the experimental data, even at low energies.

The previously existing datasets were all published before 2000, with the exception of one dataset that is from 2002. Old data does not imply low quality, but it does mean that the data have been integrated into the interpolations made by SRIM. In a database as sparse as that for heavy ion stopping, a single dataset may have a large influence over the final result.

In particular, the largest difference between the new data reported here and SRIM is for ^{197}Au, for which only one previous dataset existed above 0.2 MeV/nucleon. For the other ions, for which more data were available, agreement between the new data, and both SRIM and the previously existing data is much better.

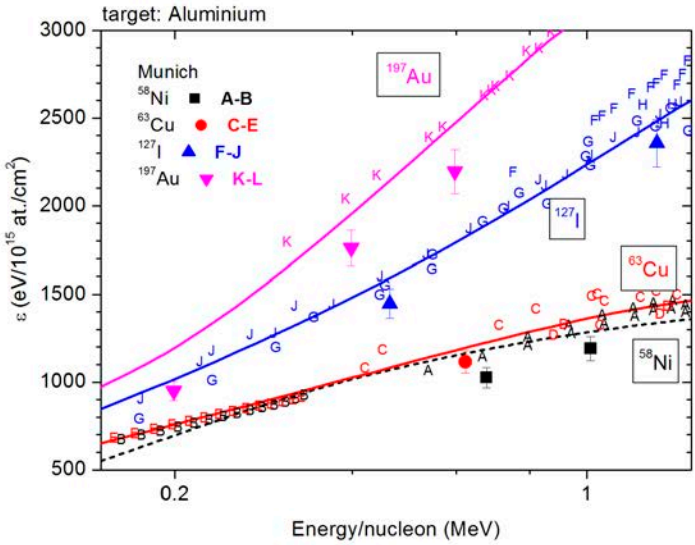

FIG. 52. Stopping cross-section of aluminium for several ions. The lines are SRIM2012 calculations (solid in all cases, except for ^{58}Ni, for which it is dashed). The symbols with error bars are the new results reported in this publication. The letters are previous results from the literature: ^{58}Ni: A, B [74–76]; ^{63}Cu: C–E [75, 76, 78, 84]; ^{127}I: F–J [74–76, 78, 87, 89]; ^{197}Au: K–L [78, 88].

This could mean that SRIM may be overestimating the stopping power of aluminium for gold ions. However, the possibility cannot be discarded that some unaccounted for systematic effect is present in the new experiments now reported that would affect, for instance, the value determined for the aluminium foil thickness. Given the care taken in evaluating uncertainties, such an effect is not likely to be present.

6.4. STOPPING CROSS-SECTION OF SILICON

The stopping cross-sections of silicon for several ions are shown in Fig. 53. In all cases, the bulk sample method was used; therefore, the results are presented, for each ion, as two continuous lines, corresponding to the average value plus and minus one standard deviation. That is, the two continuous lines represent the limits of confidence for the stopping cross-sections determined for a $k = 1$ coverage.

The values calculated with SRIM and MSTAR are also shown. In all cases, nuclear stopping power is included in the calculated stopping. Other previously available experimental data are also included in the figure, except for ^{4}He in

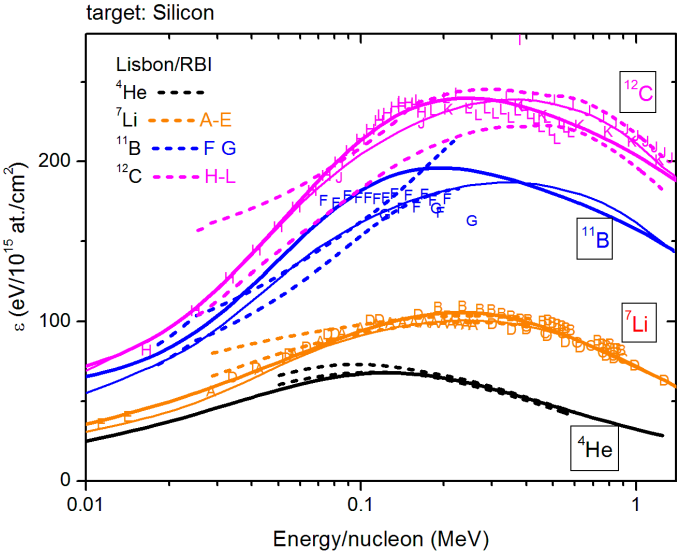

FIG. 53. Stopping cross-section of silicon for several ions. The new data are given as an average ±1 standard deviation (two dashed lines per ion). The SRIM and MSTAR predictions are shown as thick and thin solid lines, respectively. The letters are previous results from the literature: ^{7}Li: A–E [90–94]; ^{11}B: F, G [95, 96]; ^{12}C: H–L [93, 96–99]. RBI — Ruđer Bošković Institute.

silicon, where the amount of data is staggering. For that case, SRIM is accurate within 2% in an energy range close to the stopping maximum [42, 43] and within 0.8% at 1.5 MeV [3].

The measurement of the silicon stopping power for ^{4}He ions can be seen as a test case for the bulk sample method because this stopping power is very well known. The results agree very well both with SRIM and with Konac et al. [33] stopping values, which validates the present approach. At low energies, below 500 keV, the deviation seen is within two standard deviations, so it is statistically not significant.

For the other ions shown in Fig. 53, the SRIM and MSTAR calculations generally agree well with the results now obtained. The only exception is ^{11}B at energies between 0.04 and 0.18 MeV/nucleon, for which the new results confirm that SRIM overestimates the experimental data, something already suggested by the previously existing data, whereas MSTAR is in excellent agreement with the data collected.

The stopping cross-sections of silicon for ^{63}Cu, ^{127}I and ^{197}Au ions are shown in Fig. 54. In this case, the transmission method was used. No previous experimental data could be found for any of these ions in this energy range. The SRIM calculations are in good agreement with the new data reported here. For ^{63}Cu, previous data at lower energies than the results now reported were also in good agreement with SRIM.

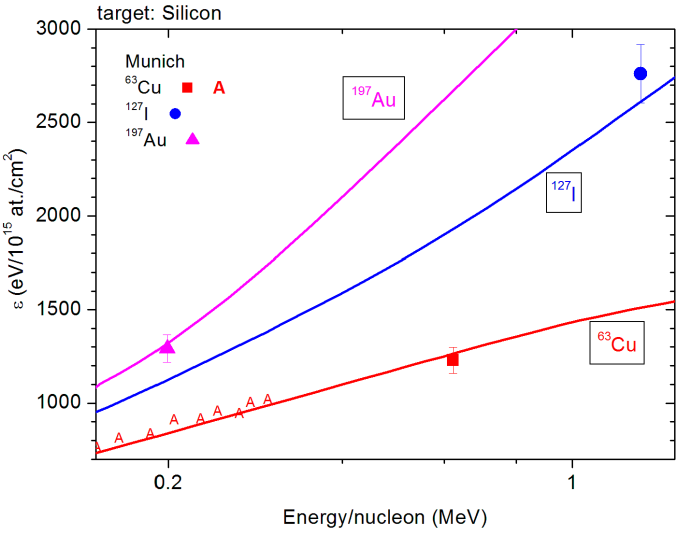

FIG. 54. Stopping cross-section of silicon for ^{63}Cu, ^{127}I and ^{197}Au ions. The SRIM calculations are shown as solid lines. The letters are previous results from the literature: ^{63}Cu: A [96].

6.5. STOPPING CROSS-SECTION OF NICKEL

The stopping cross-sections of nickel for ^{58}Ni, ^{127}I and ^{197}Au ions are shown in Fig. 55. In this energy range, only one previous experimental dataset could be found for gold [100], which was consistently below the SRIM calculation that is also shown in the figure. Two datasets were found for indium, one of them in agreement [86] and the other consistently below [87] the SRIM calculation.

The SRIM calculations include the contribution of nuclear stopping. In this case, for the energies at which the experiments are reported, this contribution is small: below 0.4% for gold ions and around 0.1% for nickel and indium ions.

The new data for ^{58}Ni and ^{127}I are in excellent agreement with the SRIM prediction. However, for ^{197}Au, the central values determined are slightly lower than the values calculated with SRIM and are in agreement with other experimental values previously reported in the literature. However, the difference is smaller than one standard deviation, and SRIM can be considered to be correct within the experimental uncertainty. In this case, the difference previously found is supported, but it cannot be definitively proven based on the new results now reported.

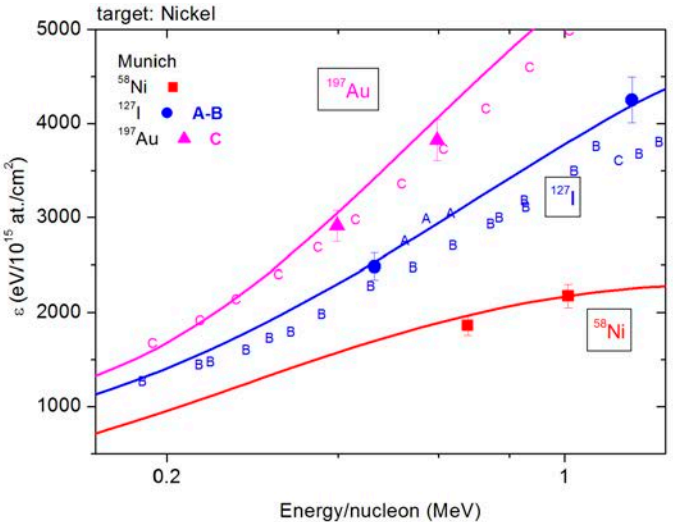

FIG. 55. Stopping cross-section of nickel for ^{58}Ni, ^{127}I and ^{197}Au ions. The SRIM calculations are shown as solid lines. The letters are previous results from the literature: ^{127}I: A, B [86, 87]; ^{197}Au: C [100].

6.6. STOPPING CROSS-SECTION OF HAFNIUM

The measured stopping cross-section of hafnium for ^{63}Cu, ^{127}I and ^{197}Au ions is shown in Fig. 56, together with the corresponding curves calculated with SRIM. In all cases, the experimental values are smaller than the SRIM calculation. For ^{63}Cu, the difference is within two standard deviations, so it may not be significant, and more data would be needed for a definitive assessment to be made.

For ^{127}I and ^{197}Au ions, on the contrary, the reported values are significantly below those from SRIM, and it can be concluded that the new data should lead to a change in the interpolations made by future versions of SRIM for this target and these ions.

In this case, it is essential to include the nuclear stopping power in the SRIM calculations when comparing with the experimental results. For instance, for gold at the energy measured, the contribution of nuclear stopping is around 15% of the contribution of electronic stopping, which is clearly significant. The experimental value is in agreement, within the uncertainty of the experiment, with the calculated electronic stopping power, which is misleading because the nuclear stopping power must be included in the calculations.

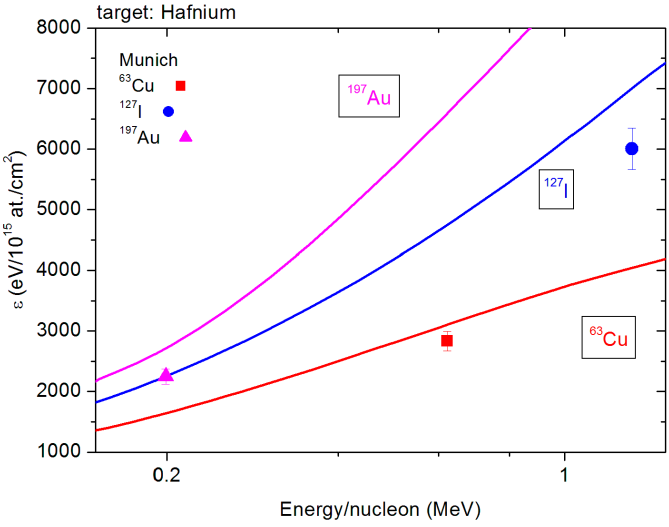

FIG. 56. Stopping cross-section of hafnium for ^{63}Cu, ^{127}I and ^{197}Au ions. The SRIM calculations are shown as solid lines.

6.7. STOPPING CROSS-SECTION OF GOLD

The stopping cross-sections of gold for ^{58}Ni, ^{127}I and ^{197}Au ions are shown in Fig. 57. For ^{127}I and ^{197}Au, several experimental datasets that already exist in the literature for this energy range are also included in the figure. The curves, as calculated with SRIM and including nuclear stopping, are also shown. For the new data measured, the contribution of nuclear stopping is always below 5%.

The new measurement for ^{58}Ni is in good agreement with the SRIM calculation, within the stated uncertainty. The central values determined are slightly above the calculation. Previously reported experimental data were also higher than SRIM in this energy range.

For ^{127}I at 170 MeV (around 1.3 MeV/nucleon), the new measurement reproduces the SRIM calculation well and is in good agreement with three previously existing datasets (B, C, D in Fig. 57). On the contrary, one dataset (F in Fig. 57 [87]) is much lower than all the other experiments and also much lower than SRIM for this energy. This dataset is also the earliest measurement for this system, published in 1967. It can be concluded that, at this energy, SRIM is correct and dataset F is too low.

At lower energies, and down to 0.4 MeV/nucleon, dataset F continues to be consistently lower than the SRIM calculation. This is the case, for instance,

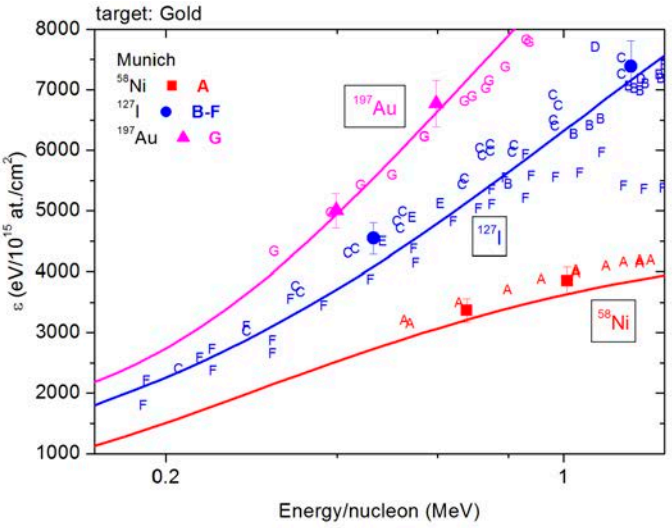

FIG. 57. Stopping cross-section of gold for ^{58}Ni, ^{127}I and ^{197}Au ions. The SRIM calculations are shown as solid lines. The letters are previous results from the literature: ^{58}Ni: A [74]; ^{127}I: B–F [74, 78, 86, 87, 89]; ^{197}Au: G [78].

at 60 MeV (around 0.47 MeV/nucleon), at which the newly measured data are in agreement with datasets C and E, and clearly above SRIM. It can be concluded that for this system the SRIM results are either correct or slightly too low in the energy range of 0.4–0.6 MeV/nucleon.

6.8. STOPPING CROSS-SECTION OF Al_2O_3

The stopping cross-section of Al_2O_3 for each ion is shown in a separate figure for clarity. The MSTAR calculations considered molecular stopping power and did not use the Bragg rule. The SRIM calculations used the Bragg rule. In both cases, the contribution of nuclear stopping was included in the calculations.

The experiments performed at the University of Helsinki utilized a transmission method (see Section 2.4.3), together with a fitting procedure, that led to a continuous stopping cross-section curve, while also providing the fitting error, which can be taken as the uncertainty. Therefore, the Helsinki results are shown as two lines, which represent the confidence limits of the experiment for a $k = 1$ coverage: they are the fitted stopping power curve plus and minus one standard deviation. Some of the previously measured data [48] were also originally presented as two continuous lines, and these are reproduced here as they were published.

The stopping cross-section of Al_2O_3 for ^{12}C ions is shown in Fig. 58. Three experiments were performed and, therefore, three new datasets are presented. One further dataset from the literature [48] is also shown. The significant uncertainties of the new datasets are dominated by the uncertainty of the energy loss in the Si_3N_4 membrane, as described in Section 5.2.5.

The universities of Helsinki and Jyväskylä used the same sample (i.e. the Al_2O_3 film grown on an Si_3N_4 membrane with ALD; see Section 4.1). In this respect, the two datasets are only partially independent of each other, given that the set-ups and method used were different. However, iThemba LABS used a completely different sample, produced by electron beam deposition onto Si_3N_4 foils at the Materials Department of iThemba LABS, as described in Section 3.5.

The new measurements agree with each other within the stated uncertainties. They also agree with the SRIM and MSTAR calculations in the energy range of 0.1–0.7 MeV/nucleon. The only dataset that extends to both lower and higher energies is the one collected at the University of Helsinki. At higher energies, the newly measured values are higher than both the previously reported experiments and than the SRIM and MSTAR calculations. However, the difference is within two standard deviations; therefore, it is not significant at $k = 2$ coverage.

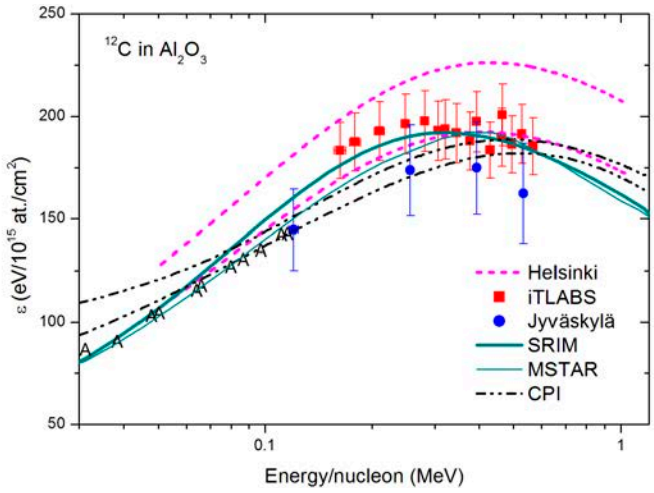

FIG. 58. Stopping cross-section of Al_2O_3 for ^{12}C. The data marked CPI [48] are given as two lines representing the limits of confidence of that experiment. The letters are previous results from the literature: A [101].

The stopping cross-section of Al_2O_3 for ^{16}O ions is shown in Fig. 59. Calculations made with SRIM and with MSTAR are also shown. Nuclear stopping already makes a significant contribution at the lowest energies probed: around 5% for the lowest energy measured by the University of Helsinki. The energy range measured by iThemba LABS does not extend to such low energies, and the contribution of nuclear stopping is, at most, only 0.6% of the total.

The two measurements agree with each other and with the SRIM and MSTAR calculations within their stated uncertainties. However, they seem to have a slightly different energy dependence. At the highest energies measured at iThemba LABS, close to 0.4–0.5 MeV/nucleon, the two experimental datasets have nearly the same values. As the energy decreases, the values from the iThemba LABS seem to decrease faster than those from the University of Helsinki; nevertheless, they are still within the stated experimental uncertainty. It should be stressed once again that the two experiments reported are completely independent, originating from separate samples produced in different laboratories and with different methods.

At energies higher than 0.5 MeV/nucleon and lower than 0.05 MeV/nucleon, the new experimental data are slightly higher than the values calculated with SRIM and MSTAR, but the difference is, again, within two standard deviations. Pascual-Izarra et al. [48] used a fitting method to analyse experimental data from a specially prepared sample with marker layers. The average values reported by

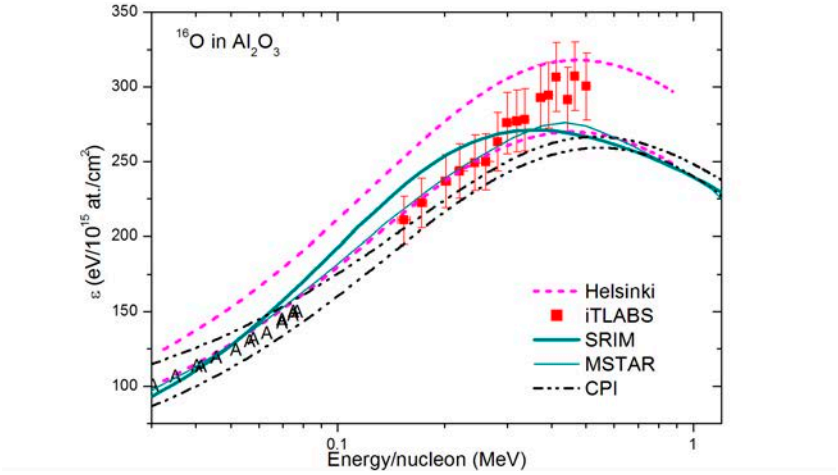

FIG. 59. Stopping cross-section of Al_2O_3 for ^{16}O. The data marked CPI [48] are given as two lines representing the limits of confidence of that experiment. The letters are previous results from the literature: A [101].

Pascual-Izarra et al. [48] are below the average values of the two new datasets. However, they fall within the uncertainty of the experiments.

The stopping cross-section of Al_2O_3 for ^{28}Si ions is shown in Fig. 60. The SRIM and MSTAR calculations include the contribution of nuclear stopping power, as calculated with SRIM. This contribution is 1.4% of the electronic stopping at the lowest energy measured, 0.14 MeV/nucleon.

A single dataset was measured in this work. The new data are slightly higher than data previously reported by Arstila [50] but in good agreement once the uncertainties are considered. The previous data by Arstila extend to lower energies, down to 0.06 MeV/nucleon. Both datasets are in good agreement with the values calculated with SRIM and MSTAR above 0.2 MeV/nucleon. However, below around 0.2 MeV/nucleon, the SRIM and MSTAR calculations become different, with the MSTAR values clearly below the SRIM ones. In that energy range, the Arstila data were closer to MSTAR. The new results now reported confirm that MSTAR reproduces the experimental data more closely at energies below 0.2 MeV/nucleon.

The stopping cross-section of Al_2O_3 for ^{35}Cl ions is shown in Fig. 61. No other previous data are known for this system.

The datasets measured by the universities of Helsinki and Jyväskylä both cover the energy range between 0.02 MeV/nucleon and 0.25 MeV/nucleon. The University of Helsinki data extend to higher energies, up to 0.5 MeV/nucleon, while the University of Jyväskylä data go down to about 0.01 MeV/nucleon.

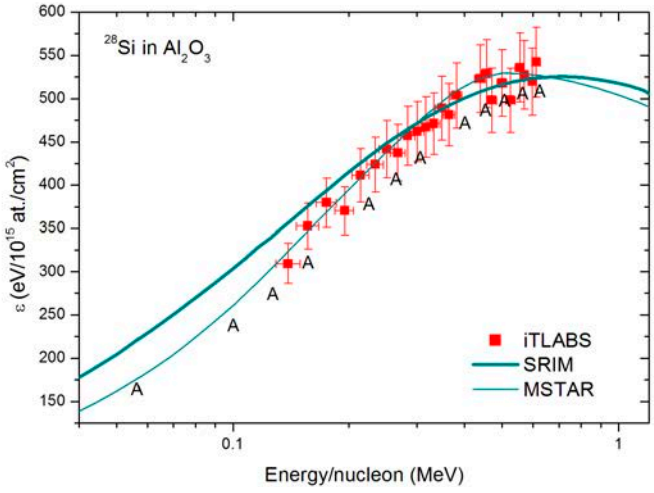

FIG. 60. Stopping cross-section of Al_2O_3 for ^{28}Si. The letters are previous results from the literature: A [50].

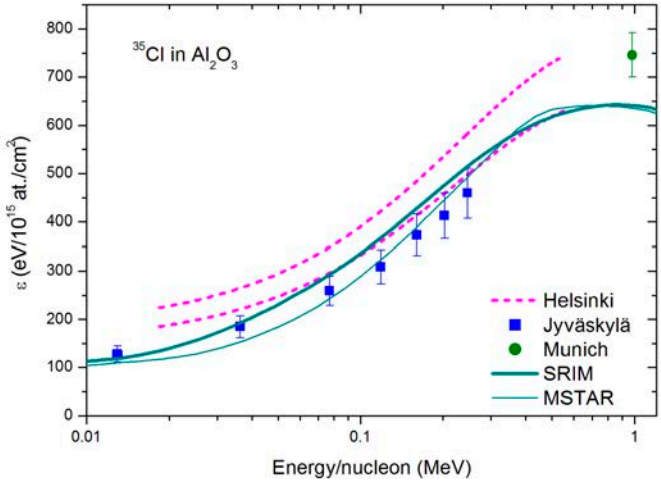

FIG. 61. Stopping cross-section of Al_2O_3 for ^{35}Cl.

The Munich data are one isolated measurement at a higher energy, at almost 1 MeV/nucleon. This measurement is above the SRIM and MSTAR calculations but within two standard deviations. The Helsinki values are higher than the Jyväskylä values for the same energy, but the differences are, in general, within the uncertainties. The Helsinki data agree better with the SRIM calculation, and

the Jyväskylä dataset is in almost perfect agreement with the MSTAR values, which are lower than the SRIM ones between 0.02 and 0.3 MeV/nucleon. All in all, given the fairly large uncertainties and the fact that nuclear stopping plays an important role at low energies in this system (at 0.01 and 0.02 MeV/nucleon, it is 48% and 21%, respectively, of the electronic stopping), the new data support both SRIM and MSTAR, and they are not sufficient to decide between the small difference between the two calculations.

The stopping cross-section of Al_2O_3 for ^{58}Ni ions is shown in Fig. 62. This is the only known result for this system. The data point at one single energy, around 1 MeV/nucleon, measured by the Munich group, is clearly above the SRIM calculation, outside the uncertainty of the experiment. MSTAR only calculates the stopping of ions with an atomic number, *Z*, between 3 and 18 and cannot be used for this system.

The stopping cross-section of Al_2O_3 for ^{79}Br ions is shown in Fig. 63. There are no known previous experimental data for this system. The Helsinki data are in agreement with the values calculated with SRIM for the entire energy range measured, between 0.04 and 0.5 MeV/nucleon. However, above 0.2 MeV/nucleon, the average values determined experimentally start to increase with respect to SRIM, which is confirmed by the Munich data point. It can be concluded that SRIM underestimates the experimental data at energies around 0.5 MeV/nucleon.

Finally, the stopping cross-section of Al_2O_3 for ^{127}I ions is shown in Fig. 64. No previously measured data could be found in the literature in the energy range

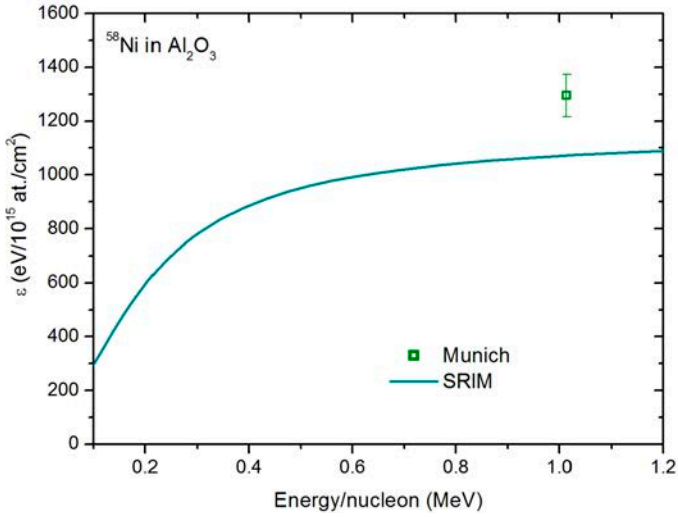

FIG. 62. Stopping cross-section of Al_2O_3 for ^{58}Ni.

now measured. One previous experiment at higher energies was found and is also shown. The dataset measured at the University of Helsinki agrees well with the SRIM calculations for the entire energy range measured.

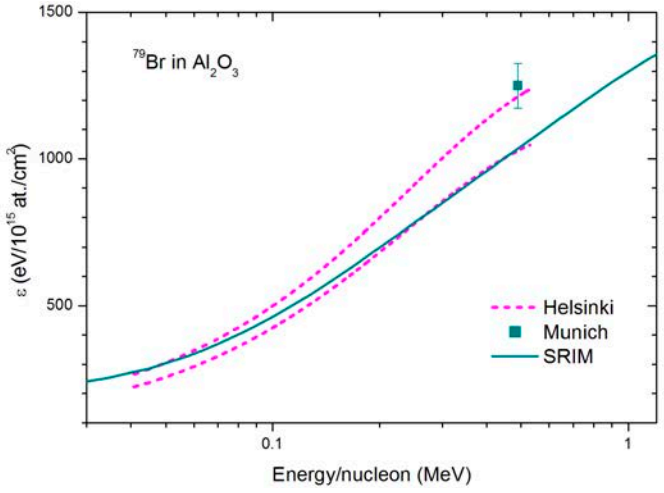

FIG. 63. Stopping cross-section of Al_2O_3 for ^{79}Br.

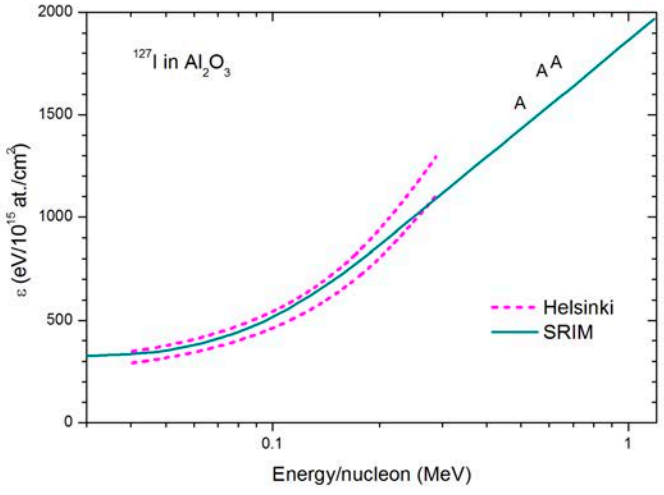

FIG. 64. Stopping cross-section of Al_2O_3 for ^{127}I. The letters are previous results from the literature: A [101].

6.9. STOPPING CROSS-SECTION OF SiO_2

The measured stopping cross-sections of SiO_2 for ^{12}C and ^{28}Si ions are shown in Fig. 65. Previously reported data are also shown, together with SRIM and MSTAR calculations. MSTAR considered molecular stopping power and did not use the Bragg rule. SRIM used the Bragg rule. In both cases, nuclear stopping, as calculated with SRIM, is included.

For both ions, the new data agree very well within uncertainties with the data from the literature. For ^{28}Si, the previously existing data seemed to lie between the values calculated with SRIM and those calculated with MSTAR at energies below around 0.2 MeV/nucleon. Without having a full uncertainty analysis for those experiments, it is difficult to evaluate whether that discrepancy is statistically significant or not.

The new data in that energy range (below around 0.2 MeV/nucleon) fall between the previous experimental data points and the SRIM calculation, which are 8% apart. In that case, to distinguish between the two cases, and considering a coverage factor $k = 2$ for a 95% level of confidence, an uncertainty of 2% in the new data would be required. This level of accuracy is extremely difficult to obtain, particularly considering that the systematic uncertainty owing, for instance, to the uncertainty in the areal density of the foil used is usually larger than that. For example, for the foils used at iThemba LABS, this was around 3–4%, as shown in Section 4.1.

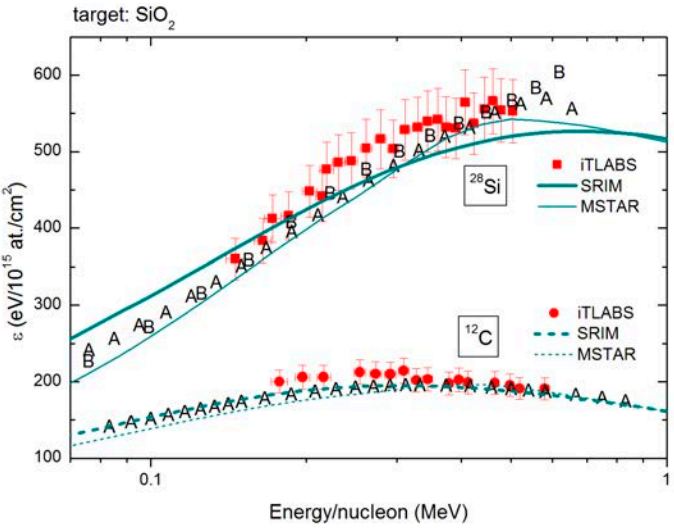

FIG. 65. Stopping cross-section of SiO_2 for ^{12}C and ^{28}Si ions. The letters are previous results from the literature: A [102] (^{12}C and ^{28}Si); B [50] (^{28}Si only).

Overall, the new data collected are in agreement, within the uncertainty, with the previously existing data and with both the SRIM and MSTAR calculations. Nevertheless, it can be observed that the shape of the stopping curve calculated with MSTAR is a better match to the experimental data than that calculated with SRIM.

6.10. STOPPING CROSS-SECTION OF TiO_2

The stopping cross-sections of TiO_2 for ^{4}He, ^{11}B, ^{12}C and ^{16}O ions are shown in Fig. 66. In all cases, the bulk sample method was used; therefore, the results are presented, for each ion, as two continuous lines, corresponding to the average value plus and minus one standard deviation; that is, the two continuous lines represent the limits of confidence for the stopping cross-sections determined for a $k = 1$ coverage.

Shown also are the stopping cross-sections calculated with SRIM and MSTAR from the titanium and oxygen elemental stopping powers, assuming the Bragg rule, and including nuclear stopping as calculated with SRIM. In all cases, the SRIM and MSTAR calculations are rather close to each other.

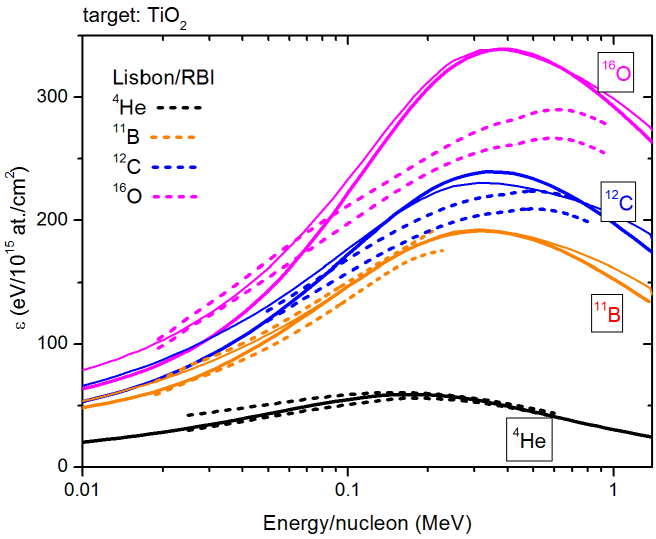

FIG. 66. Stopping cross-section of TiO_2 for several ions. The thick and thin solid lines are SRIM and MSTAR calculations using the Bragg rule, respectively. RBI — Ruđer Bošković Institute.

For the two lighter ions, ^{4}He and ^{11}B, the data are in good agreement with SRIM. For ^{11}B, where the MSTAR calculation is available, the data are also in good agreement with MSTAR.

For the two heavier ions, ^{12}C and ^{16}O, strong deviations are observed between the values now determined and SRIM, particularly at the Bragg peak. Considering the good agreement for the ^{4}He and ^{11}B ions, and the excellent agreement between SRIM and experimental values of the stopping of elemental titanium for oxygen in a similar energy range [103], this result might be considered somewhat unexpected. However, any departure from the Bragg rule used to calculate the SRIM and MSTAR curves is expected to occur precisely near the stopping power maximum, as observed here.

6.11. STOPPING CROSS-SECTION OF ZrO_2

The stopping cross-sections of ZrO_2 for several ions are shown in Fig. 67, together with calculations made with SRIM and MSTAR using the Bragg rule. Nuclear stopping, as calculated with SRIM, is included in both calculations.

In all cases, the new experimental results agree well with SRIM within the experimental uncertainty, and also with previous experiments that are available in the literature for ^{12}C, ^{16}O and ^{19}F. However, in all cases, MSTAR matches the data better, reproducing the data extremely well.

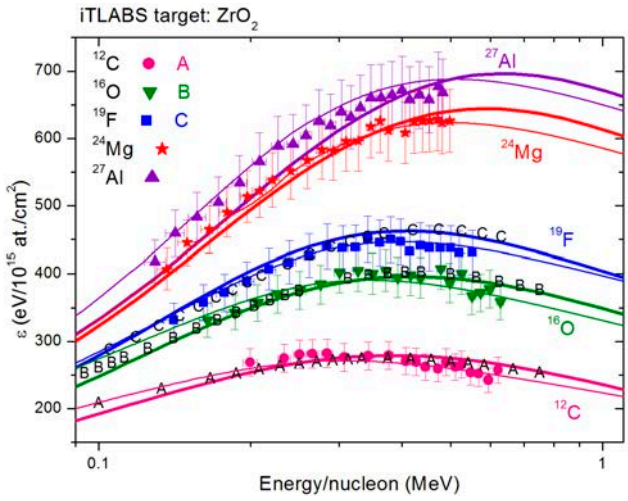

FIG. 67. Stopping cross-section of ZrO_2 for several ions. The thick and thin solid lines are SRIM and MSTAR calculations using the Bragg rule, respectively. The letters are previous results from the literature: ^{12}C: A [104]; ^{16}O: B [105]; ^{19}F: C [105].

6.12. STOPPING CROSS-SECTION OF Ta_2O_5

In the figures related to Ta_2O_5, the stopping cross-section for each ion is shown separately for the sake of clarity. The University of Helsinki results, as well as the results obtained with the bulk sample method by Instituto Superior Técnico or Ruđer Bošković Institute, are shown as two lines representing the limits of confidence for a coverage factor $k = 1$. The Bragg rule was used to calculate the molecular stopping power on the basis of the elemental stopping powers of tantalum and oxygen, with SRIM and MSTAR.

The stopping cross-section of Ta_2O_5 for ^{12}C is shown in Fig. 68. No reports of previous experiments were found in the literature.

Two experiments were performed, using two unrelated samples and with very different experimental methods. In the energy range in which the two experiments overlap, they agree with each other and with SRIM within the experimental uncertainty. In any case, the central values of the Helsinki dataset are always above the central values determined with the bulk sample method by Instituto Superior Técnico or Ruđer Bošković Institute. At energies below 0.15 MeV/nucleon, the Helsinki results become progressively higher than the SRIM and MSTAR calculations. At energies above that value, the experimental data agree better with SRIM than with MSTAR.

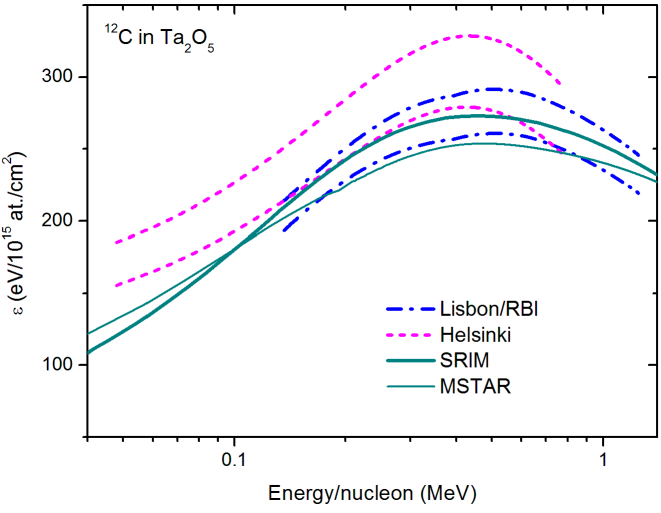

FIG. 68. Stopping cross-section of Ta_2O_5 for ^{12}C. RBI — Ruđer Bošković Institute.

The stopping cross-section of Ta_2O_5 for ^{16}O is shown in Fig. 69. The two new measurements agree with each other within uncertainties and with the data previously published by Zhang et al. [106]. At low energies, the Helsinki measurement starts to deviate slightly from the SRIM calculation, which otherwise represents the experimental data very well. MSTAR predicts higher values at those low energies and is, therefore, in better agreement with the data than SRIM in that energy range.

The stopping cross-section of Ta_2O_5 for ^{35}Cl is shown in Fig. 70. No previous data were found in the literature. Calculations made with SRIM and MSTAR using the Bragg rule are also shown. In both cases, nuclear stopping, as calculated with SRIM, is included. At 0.02 MeV/nucleon, it is 28% of the electronic stopping (as calculated with SRIM), at 0.1 MeV/nucleon this has decreased to 3.5% and at 1 MeV/nucleon it is 0.2%.

Three datasets were measured. All three of them, including the single point measured in Munich and the continuous curves obtained with the bulk sample method in Helsinki, agree very well with the SRIM calculation. MSTAR is always higher than SRIM for the entire energy range covered, and the difference towards the experimental data is outside the stated uncertainties, both for the single data point collected in Munich at 1 MeV/nucleon, and for the data collected by the Ruđer Bošković Institute (bulk sample method). In the case of the Helsinki data, the stated uncertainty is higher and the deviation towards the MSTAR calculation is only larger than the stated uncertainty in the higher energy range measured, above around 0.2 MeV/nucleon.

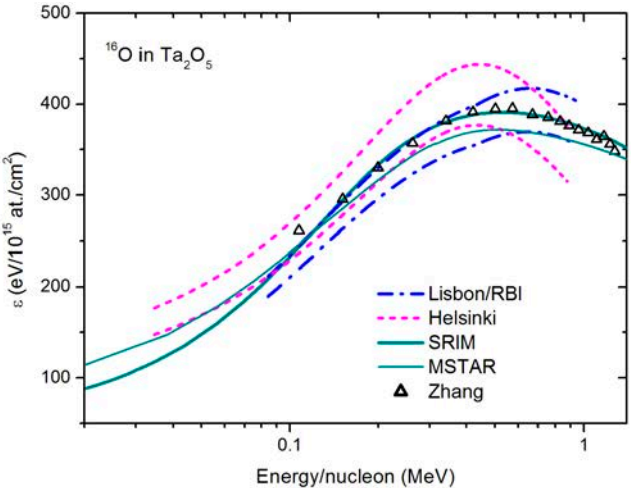

FIG. 69. Stopping cross-section of Ta_2O_5 for ^{16}O. The data marked Zhang are from Ref. [106]. RBI — Ruđer Bošković Institute.

The stopping cross-section of Ta_2O_5 for ^{58}Ni is shown in Fig. 71. No previously existing measurements of this system could be found in the literature, so the SRIM calculation shown necessarily comes from an interpolation based on data for other systems.

The experimental data now presented are higher than the SRIM calculation by around two standard deviations. This was not the case, for instance, with the stopping power of Ta_2O_5 for ^{35}Cl shown in Fig. 70, also measured in Munich, and using exactly the same sample, so a systematic effect caused by an inaccurate value of the areal density value used must be discarded, and it can be concluded that the SRIM calculation is too low by around 1 MeV/nucleon.

The stopping cross-section of Ta_2O_5 for ^{79}Br is shown in Fig. 72. No previous measurements were found in the literature. The Helsinki data agree with SRIM within the stated accuracy up to 0.4 MeV/nucleon, where they start to become higher than the values calculated with SRIM. The fairly large uncertainty means, however, that the deviation is always within two standard deviations. Nevertheless, the single point measured in Munich for an energy of around 0.5 MeV/nucleon is clearly higher than SRIM and the deviation is not within the stated uncertainty, which is lower for the Munich experiment. It can be concluded that the SRIM calculation, which in this case is also an interpolation based on results from other systems, underestimates the measured value.

The stopping cross-section of Ta_2O_5 for ^{127}I is shown in Fig. 73. Good agreement between the data and the SRIM calculation is found for the entire energy range measured. At energies between 0.04 and 0.15 MeV/nucleon, the

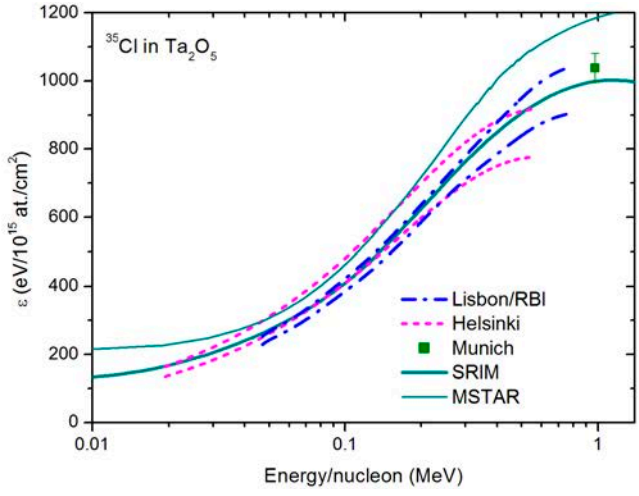

FIG. 70. Stopping cross-section of Ta_2O_5 for ^{35}Cl. RBI — Ruđer Bošković Institute.

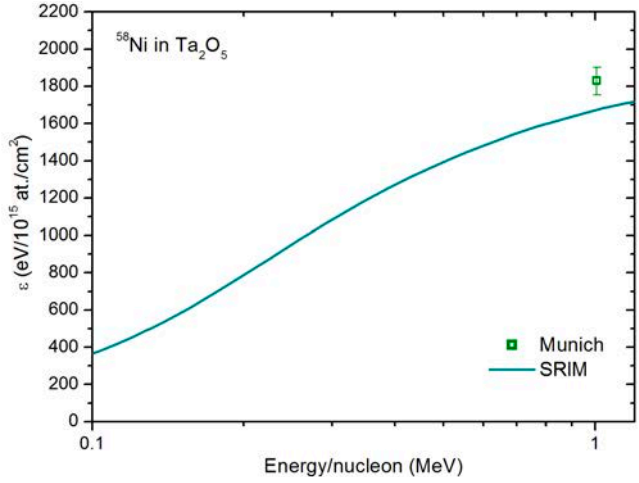

FIG. 71. Stopping cross-sections of Ta_2O_5 for ^{58}Ni.

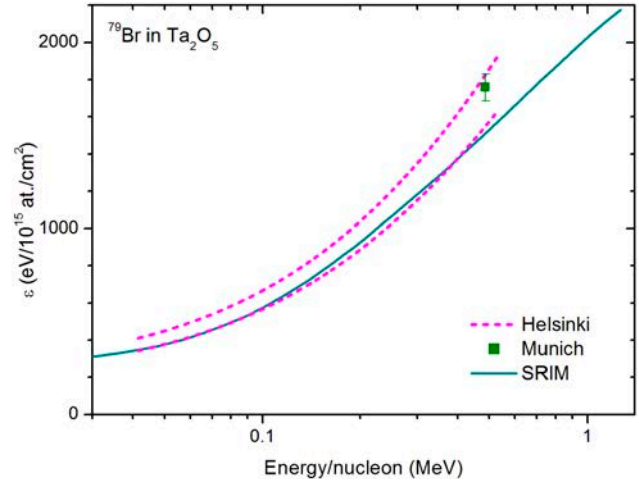

FIG. 72. Stopping cross-sections of Ta_2O_5 for ^{79}Br.

experimental data are above the curve calculated with SRIM, but the deviation is small, within two standard deviations.

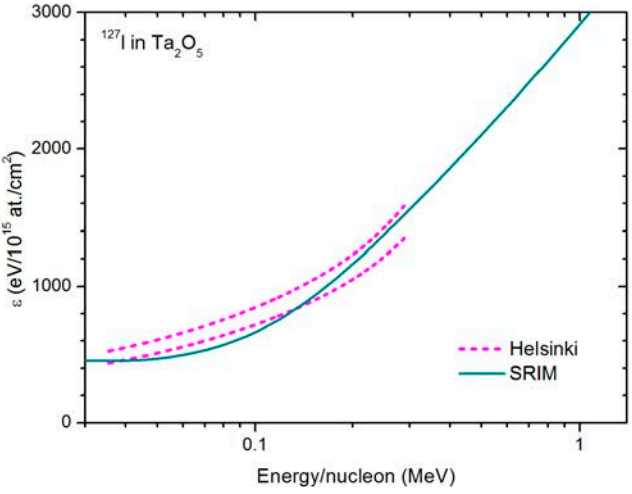

FIG. 73. Stopping cross-sections of Ta_2O_5 for ^{127}I.

6.13. STOPPING CROSS-SECTION OF Si_3N_4

In the figures related to Si_3N_4, the stopping cross-section for each ion is again shown separately for the sake of clarity. The Helsinki results are shown as two lines representing the limits of confidence for a coverage factor $k = 1$. The Bragg rule was used to calculate the molecular stopping power, based on the elemental stopping powers of silicon and nitrogen, with SRIM and MSTAR. The nuclear stopping power was calculated with SRIM and was included in all the SRIM and MSTAR calculations presented.

Some previously measured datasets were found in the literature for silicon nitride [107] for a non-stoichiometric sample with composition $Si_3N_{3.1}H_{0.06}$. The sample used in the experiments reported here was also not stoichiometric, with $Si_3N_{3.57}H_{0.13}C_{0.02}O_{0.08}$ determined with heavy ion ERDA. This raises the issue of whether the experiments are measuring comparable quantities. Here, SRIM was used to calculate the stopping power of ^{12}C and ^{16}O for the two non-stoichiometric silicon nitrides and for stoichiometric Si_3N_4. The results are shown in Figs 74 and 75 for ^{12}C and ^{16}O, respectively.

Clearly, the stopping powers calculated with SRIM for a stoichiometric Si_3N_4 and for the composition determined in Munich are very similar, with a difference of less than 0.7% at the Bragg peak for both ions. There are very few stopping power measurements that can demonstrate this accuracy.

For the sample used in Sun et al. [107], the difference is larger, reaching around 2.2% at the Bragg peak. However, this is much less than the difference

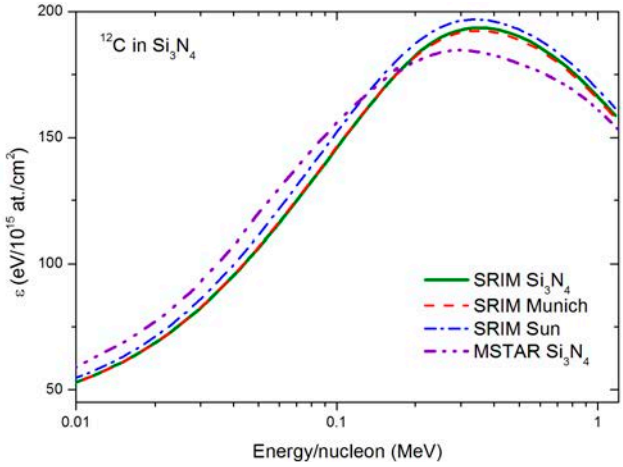

FIG. 74. Stopping cross-section of Si_3N_4 for ^{12}C, calculated with different models. The data marked Sun are from Ref. [107]. The data marked Munich are calculated for the silicon nitride stoichiometry of the sample used in the experiments reported here.

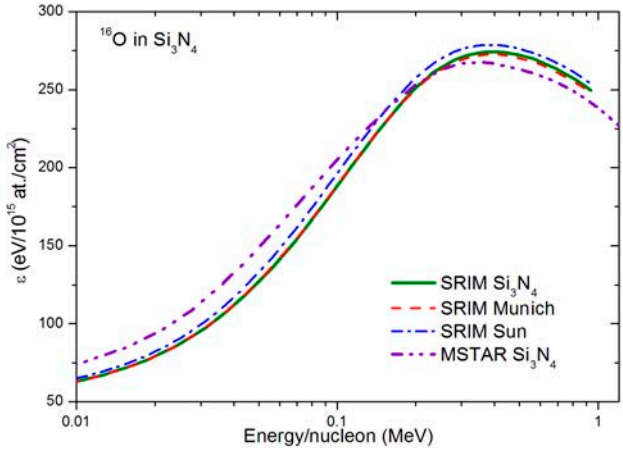

FIG. 75. Stopping cross-section of Si_3N_4 for ^{16}O, calculated with different models. The data marked Sun are from Ref. [107]. The data marked Munich are calculated for the silicon nitride stoichiometry of the sample used in the experiments reported here.

between the SRIM and MSTAR calculation for stoichiometric Si_3N_4, which is 4.6%, and few experiments claim an accuracy at the 2% level. In particular, the new data shown here have worse accuracy. In conclusion, the sample stoichiometry does have an expected influence on the stopping power, but this effect is not large, and our experimental data are not sensitive enough to measure it.

The stopping cross-section of Si_3N_4 for ^{12}C is shown in Fig. 76. The stopping power as calculated with SRIM and MSTAR for stoichiometric Si_3N_4 and for the stoichiometry of the sample used in Ref. [107] is also shown. The only previously published dataset for this system seems to be that in Ref. [107].

All the new experiments are in good agreement with each other within their stated uncertainties. They extend to energies down to 0.02 MeV/nucleon and up to 0.7 MeV/nucleon, which is beyond the dataset in Ref. [107]. The values measured are above the SRIM and MSTAR calculations in the entire energy range, with differences not covered by the uncertainties. This remains true for most data points, even considering a $k = 2$ coverage. The data in Ref. [107] are in agreement with the SRIM and MSTAR calculations, except at the highest energy measured, where they are clearly above the calculation and in good agreement with the new data reported here.

The stopping cross-section of Si_3N_4 for ^{16}O is shown in Fig. 77. The contribution of nuclear stopping is 10% of the contribution of electronic stopping, as calculated with SRIM for the lowest energy measured. This contribution becomes less important at higher energies. At 0.1 MeV/nucleon it is already 1% of the total calculated stopping power, which is already well below the accuracy of the experiments, and at higher energies it becomes insignificant.

As was observed for ^{12}C, the experimental results determined in Helsinki and Jyväskylä, and at iThemba LABS, all agree with each other within their respective uncertainties, and they are all consistently above both the SRIM and MSTAR calculated values and the results reported by Sun et al. [107], except in this case for the data point at the highest energy measured, which is in agreement

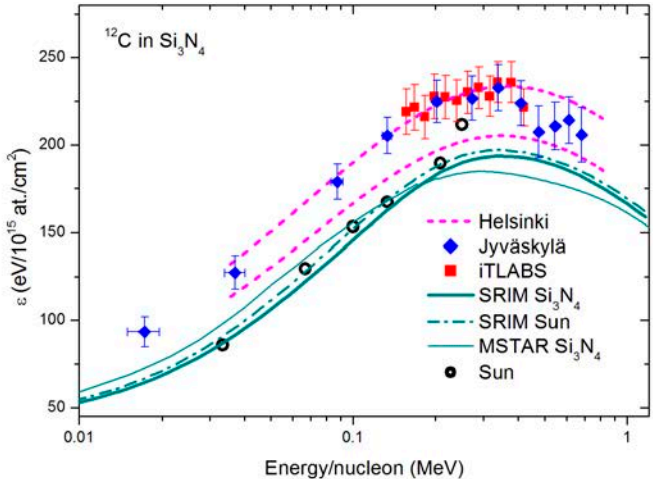

FIG. 76. Stopping cross-section of Si_3N_4 for ^{12}C. The data marked Sun are from Ref. [107].

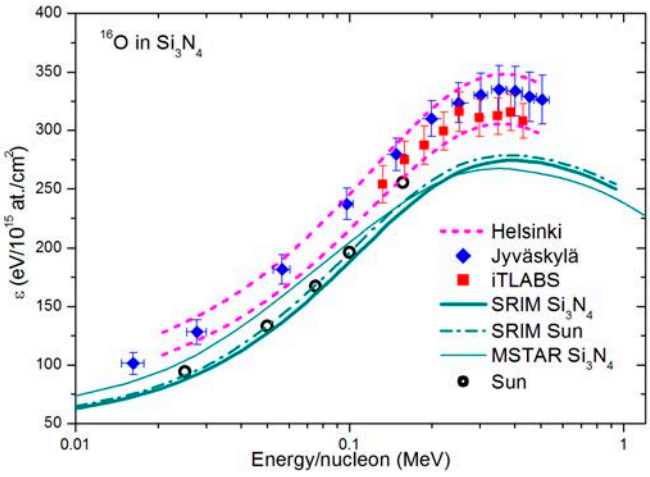

FIG. 77. Stopping cross-section of Si_3N_4 for ^{16}O. The data marked Sun are from Ref. [107].

with the new results reported. At low energies, the MSTAR calculation leads to higher values than SRIM and is, therefore, closer to the experimental data.

The stopping cross-section of Si_3N_4 for ^{28}Si is shown in Fig. 78. It seems that no other experimental data for this system have been previously published. The experimental results determined at iThemba LABS are consistently above the values calculated with SRIM and are in excellent agreement with those calculated with MSTAR.

The stopping cross-section of Si_3N_4 for ^{35}Cl is shown in Fig. 79. Again, no previous experiments could be found in the literature. The contribution of nuclear stopping relative to that of electronic stopping, as calculated with SRIM, is 27%, 2.4% and 0.56% at 0.017 MeV/nucleon (lowest energy measured), 0.1 MeV/nucleon and 0.56 MeV/nucleon (highest energy measured), respectively.

The three new datasets reported are all above the curves calculated with both SRIM and MSTAR, together with the Bragg rule. The deviations are, in general, larger than two standard deviations, and it can therefore be concluded that the SRIM and MSTAR calculations are too low.

The stopping cross-section of Si_3N_4 for ^{58}Ni is shown in Fig. 80. In this case, nuclear stopping power is around 0.3% of the total stopping power. Again, there appear not to be any previously determined datasets for this system. The values calculated with SRIM are below the experimental data, and the difference is not covered by the stated uncertainty.

The stopping cross-section of Si_3N_4 for ^{79}Br is shown in Fig. 81. In the Munich experiment, nuclear stopping does not play a role as it is only 0.6% of the total stopping power. However, in the Helsinki data, nuclear stopping reaches 24%

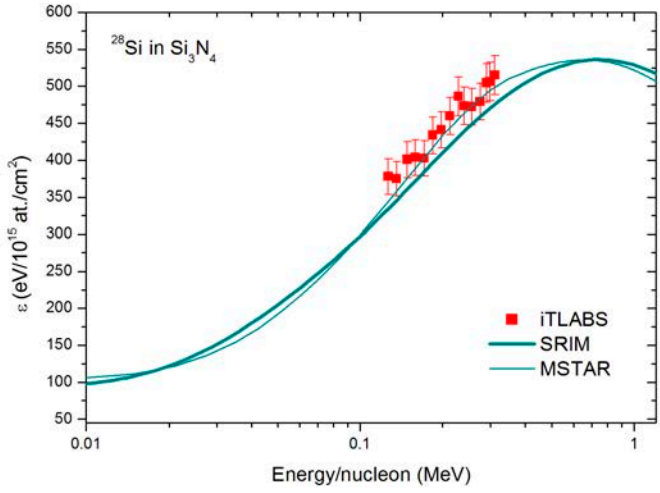

FIG. 78. Stopping cross-section of Si_3N_4 for ^{28}Si.

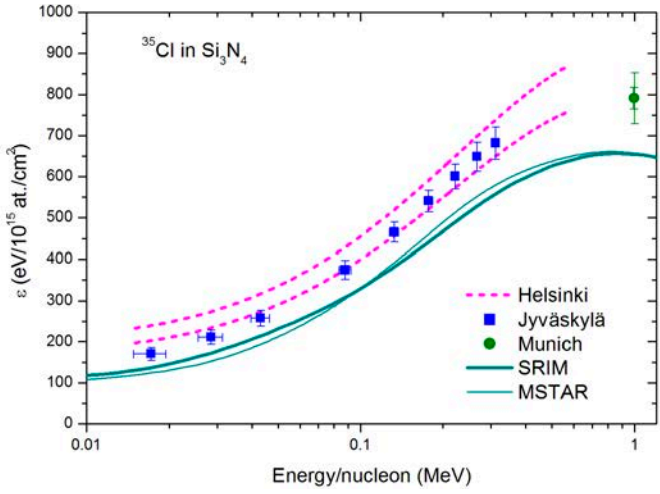

FIG. 79. Stopping cross-section of Si_3N_4 for ^{35}Cl.

at the lowest energy measured and, therefore, makes a large contribution. The two datasets agree with each other in the limited energy range over which they are superimposed. That two independent experiments were undertaken, and that they confirm each other, leads to a high level of confidence in the results obtained.

The stopping cross-section of Si_3N_4 for ^{127}I is shown in Fig. 82. Nuclear stopping power was calculated with SRIM and is included in the calculated curve

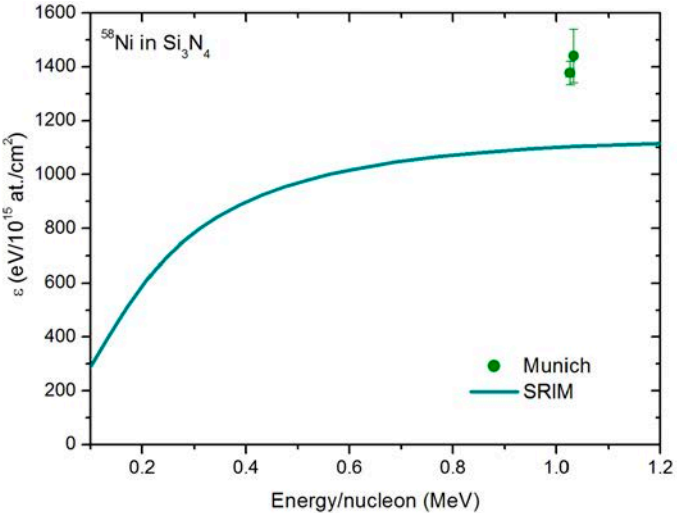

FIG. 80. Stopping cross-sections of Si_3N_4 for ^{58}Ni.

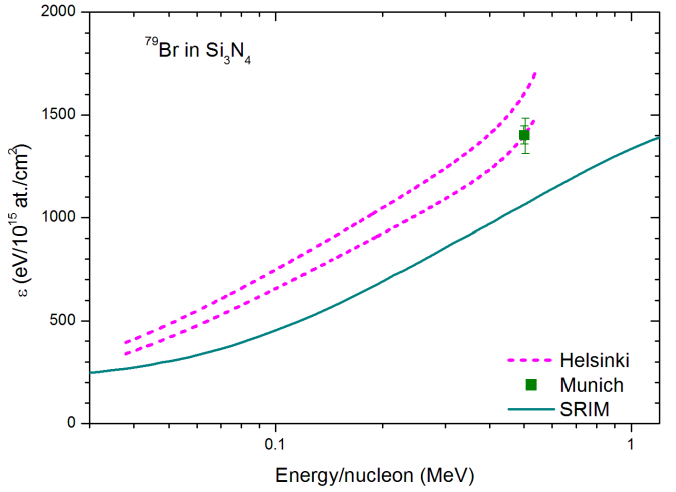

FIG. 81. Stopping cross-sections of Si_3N_4 for ^{79}Br.

shown. For this system, it is very large, reaching 63% of the electronic stopping value at the lowest energy value probed, and 2.5% at the highest energy.

This seems to be the first experimental data collected for this system and, therefore, the SRIM calculation is based on interpolations from the data of other

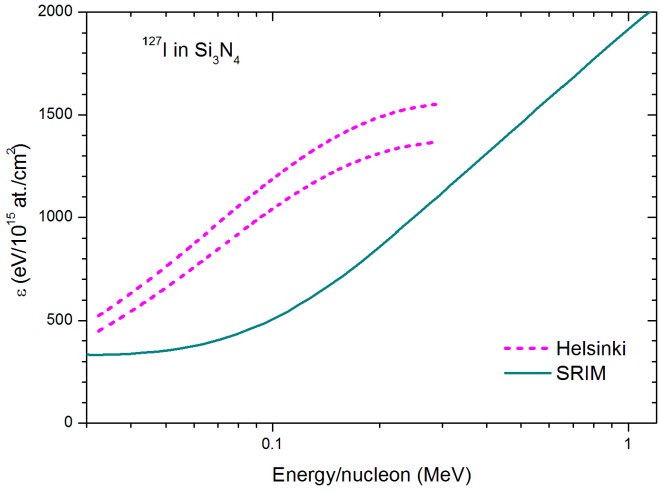

FIG. 82. Stopping cross-sections of Si_3N_4 for ^{127}I.

systems. The deviation between data and calculation is extremely large, up to a factor of two.

On the one hand, such extremely large deviations between SRIM and experiment are not expected. In addition, the actual shape of the stopping cross-section curve determined is very different from the shape calculated with SRIM for this ion. For this same material, but for lighter ions, this was not the case, as the observed and calculated shape of the stopping power curves were at least similar in general terms.

On the other hand, if large deviations are to be found, it is exactly in insulating or semiconducting oxides or nitrides of high *Z* materials. In any case, it would be important to perform an independent measurement of the stopping power for the same system to enable a definite assertion on the deviation between the SRIM prediction and the data to be made.

Taking into account the results now reported for all of the different ions, there appears to be a trend of increasing the deviation between the data and the SRIM calculation for this material as the atomic number of the projectile increases.

6.14. STOPPING CROSS-SECTION OF GaN

No experimental stopping power data of gallium nitride (GaN) for any ion appears to have been presented before this project, including for hydrogen and helium ions.

In all cases, the bulk sample method was used; therefore, the results are presented for each ion as two continuous lines, corresponding to the average value plus and minus one standard deviation; that is, the two continuous lines represent the limits of confidence for the stopping cross-sections determined for a $k = 1$ coverage (one standard deviation).

The results are shown in Fig. 83, as are the SRIM calculations. In this case, the values were calculated from the elemental stopping cross-sections of gallium and nitrogen, using the Bragg rule to calculate the molecular stopping cross-section. Nuclear stopping is included in the calculations.

Excellent agreement between the SRIM calculation and the new data is found for ^{4}He and ^{12}C. For ^{16}O, reasonable agreement is found near the Bragg peak, with deviations between the experiment and SRIM always within two standard deviations; at lower energies, the experiment shows that SRIM may be too low.

Gallium nitride is crystalline. In this case, it is extremely hard to avoid accidental channelling in a transmission experiment. On the contrary, the bulk method is well suited in this case because the sample can be tilted away from normal incidence, so the beam does not travel around a channel of the crystal lattice just as in a standard RBS experiment. The sample holder can be continuously rotated to avoid planar channelling. The detectors are also at given angles, away from crystal channels.

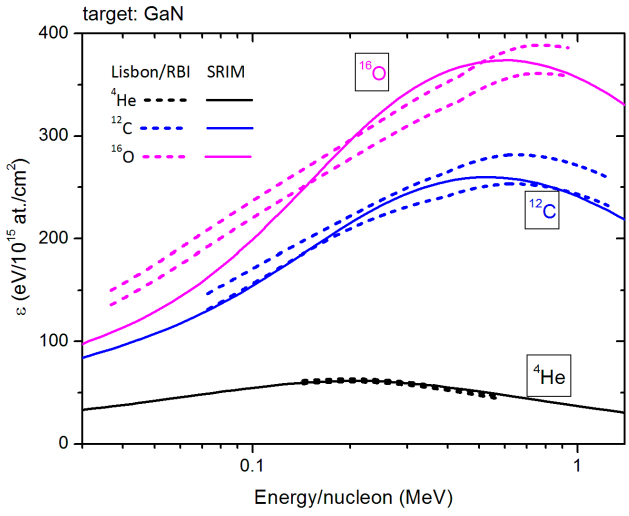

FIG. 83. Stopping cross-section of GaN for ^{4}He, ^{12}C and ^{16}O ions. RBI — Ruđer Bošković Institute.

6.15. STOPPING CROSS-SECTION OF InN

No known experimental stopping power of InN for any ion has been presented before this project, including for hydrogen and helium ions.

In all cases, the bulk sample method was used; therefore, the results are presented for each ion as two continuous lines, corresponding to the average value plus and minus one standard deviation. That is, the two continuous lines represent the limits of confidence for the stopping cross-sections determined for a $k = 1$ coverage (one standard deviation).

The results are shown in Fig. 84 as are SRIM calculations. In this case, the values were calculated from the elemental stopping cross-sections of indium and nitrogen, using the Bragg rule to calculate the molecular stopping cross-section. Nuclear stopping is included in the calculations.

Excellent agreement between the SRIM calculation and the new data is found for ^{4}He, as it was for GaN. For ^{12}C, the experimental values are consistently above the SRIM calculation, but around the Bragg peak the difference is within two standard deviations, so for a level of confidence of 95% it cannot be said that SRIM is too low.

For ^{16}O, reasonable agreement is found near the Bragg peak, with deviations between the experiment and SRIM always within two standard deviations, whereas both at higher and at lower energies the experiment shows that SRIM may be too low.

The same considerations regarding accidental channelling apply for GaN.

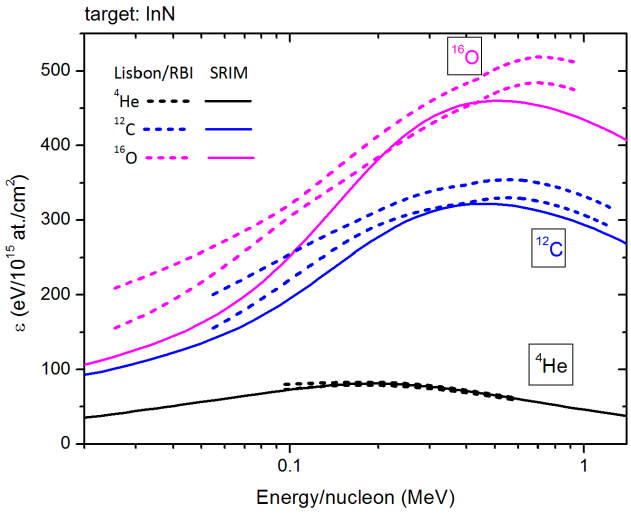

FIG. 84. Stopping cross-section of InN for ^{4}He, ^{12}C and ^{16}O ions. RBI — Ruđer Bošković Institute.

6.16. STOPPING CROSS-SECTION OF MYLAR

The stopping cross-sections of Mylar for several ions are shown in Fig. 85. Previously published experimental results are also shown for three of the ions. For the ^{19}F and ^{24}Mg ions, no previous data could be found in the literature.

The stopping cross-sections calculated with SRIM and with MSTAR are also shown. In this case, the built-in SRIM compound correction to the Bragg rule was used, based on the Cores and Bounds approach [113], given that Mylar is included in the compound dictionary of SRIM. The correction relative to the Bragg rule is in this case 4.3%, which is less than the accuracy of the experiments reported. In MSTAR, the molecular stopping power of Mylar is included and was used.

For all the ions, the new experimental results reported here agree with the SRIM and MSTAR calculations within the stated uncertainties. They are also in agreement with the vast majority of previously published experimental data. However, in some cases, a slightly better agreement of the new data collected is found with MSTAR than with SRIM.

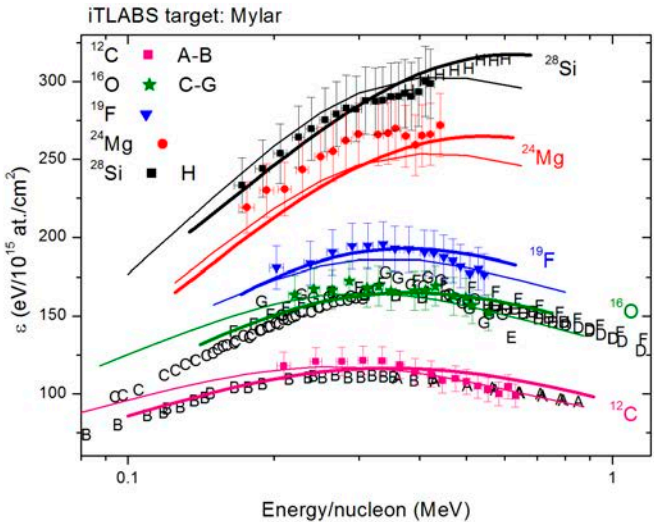

FIG. 85. Stopping cross-section of Mylar for several ions. SRIM and MSTAR calculations are shown as thick and thin solid lines, respectively. The letters are previous measurements: ^{12}C: A, B [108, 109]; ^{16}O: C–G [35, 94–102, 104–106, 108–111]; ^{28}Si: H [112].

7. RESULTS — STRAGGLING

7.1. STRAGGLING MEASUREMENTS (iTHEMBA LABS)

The results of the energy loss experiments can also be used to determine energy loss straggling. The energy spread of the beam can easily be determined from the width of the time signals, as for instance, those shown in Fig. 34. For a width of the time signal equal to Δt_i, the energy spread is:

$$\Omega_{\mathrm{i}} = 2\Delta t_i / t_i E_i \tag{20}$$

where i = 1 or 2 for the beam with and without the foil, respectively.

At a first approximation, the straggling Ω is:

$$\Omega^2 = \Omega_1^2 - \Omega_2^2 \tag{21}$$

Correct data treatment must take into account the measured roughness of the sample, which contributes to the energy spread of the beam, as well as the propagation of energy spread through thick layers, known as the Tschalär effect [114]. This was done in all cases.

Figure 86 shows a typical result of an electronic energy loss straggling evaluation (of ^{16}O ions through ZrO_2) from TOF spectra obtained during energy loss measurements [115]. The solid line is a simple second order polynomial fit to the experimental data for reproducing the straggling. Table 32 includes the fit parameters for the other ions studied in this work.

For all four ions measured, it was found that Yang et al.'s empirical formula [116] greatly underestimates straggling over the energy ranges in question. Yang et al.'s formula is based on straggling data that are, for the most part, ^{1}H and ^{2}He ions straggling through solids, and much less data on heavy ions.

Geometrical straggling and energy spread caused by multiple scattering were calculated with the state of the art code WDEPTH [9]. In this case, both contributions are negligible compared with energy loss straggling and cannot explain the difference between the data and Yang et al.'s formula.

Charge exchange straggling is expected to be a major contributor to total energy loss straggling for heavy ions. Unfortunately, there is no straggling theory at the moment that adequately addresses charge exchange straggling, and so empirical formulations such as Yang et al.'s are relied on to meet the immediate practical needs of practitioners of heavy IBA. New experimental data, as now reported, are essential to drive the development of an improved theoretical framework.

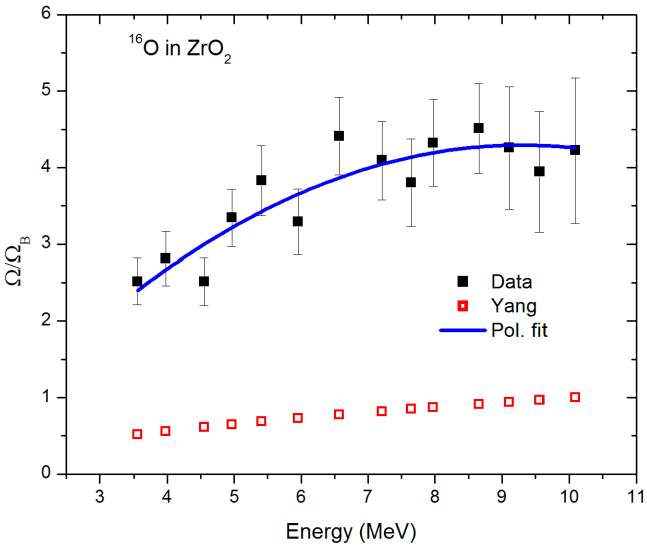

FIG. 86. Experimental electronic energy loss straggling of ^{16}O ions through ZrO_2 normalized to Bohr straggling compared with Yang et al.'s [116] predictive formulation.

TABLE 32. FIT CONSTANTS OF THE SECOND ORDER POLYNOMIAL FIT TO THE EXPERIMENTAL ENERGY LOSS STRAGGLING DATA OF ^{12}C, ^{16}O, ^{27}Al AND ^{84}Kr IONS THROUGH ZrO_2

Ion	Energy range (MeV)	a_0	a_1	a_2
^{12}C	2.0–8.0	−2.749	2.049	−0.1213
^{16}O	3.0–11.0	0.684	1.071	−0.0577
^{27}Al	4.0–15.0	0.821	0.136	0.0067
^{84}Kr	7.0–24.0	1.592	−0.0184	0.0022

7.2. STRAGGLING MEASUREMENTS (MUNICH)

The same method was employed, as by iThemba LABS, to determine the energy loss straggling in the nitride films. In the experiments done in Munich, the energy loss was around 2% of the initial energy and the Tschalär effect did not play a role. The results are given in Table 33.

TABLE 33. EXPERIMENTAL ENERGY LOSS STRAGGLING RESULTS (MUNICH)

Ion and energy	Material	Ω/Ω_{Bohr}
60 MeV nickel	Si_3N_4 (using a 100 nm sample)	1.032 34
	Si_3N_4 (using a 30 nm sample)	0.918 28
	Al_2O_3	1.135 28
	Ta_2O_5	0.925 17
40 MeV bromine	Si_3N_4 (using a 100 nm sample)	0.963 77
	Si_3N_4 (using a 30 nm sample)	1.030 42
	Al_2O_3	1.020 94
	Ta_2O_5	0.930 34
35 MeV chlorine	Si_3N_4 (using a 100 nm sample)	1.616 09
	Si_3N_4 (using a 30 nm sample)	1.699 84
	Al_2O_3	1.769 1
	Ta_2O_5	1.498 68

The results for Al_2O_3 and Ta_2O_5 were calculated by subtracting the straggling in the Si_3N_4 membrane, which was obtained from the straggling measured for the membrane without foil by scaling it to the Si_3N_4 areal density in the samples with foil.

8. RESULTS — ELECTRON SCREENING EXPERIMENTS (UNIVERSITY OF JYVÄSKYLÄ)

The Rutherford cross-section is derived for a purely electrostatic interaction between two bare nuclei. This is an approximation as, strictly speaking, the interaction is neither purely electrostatic nor between two bare nuclei. Short range nuclear forces, at energies sufficiently high that the distance of closest

approach between the ion and the target nuclei becomes comparable to the size of the nuclei, lead to strong deviations from the Rutherford cross-section (and, eventually, to inelastic nuclear reactions), but deviations appear even at much lower energies [117].

At low energies, where the distance of closest approach is greater than the radius of the innermost electron shell of the target nucleus, the electrostatic interaction is no longer between bare nuclei, and electron screening plays an important role, leading to a decrease of the scattering cross-section. Given the quantum mechanical nature of the interaction, electron screening is always present.

To take electron screening into account, scattering cross-sections derived from a potential that includes electron screening can be used [11]. Data analysis codes usually take a different approach, implementing an analytical screening correction to the Rutherford cross-section, such as that given by L'Ecuyer et al. [118] or by Andersen et al. [61]. However, as was shown in Section 5.2.1, different calculations yield slightly different results. In particular, the analytical corrections were derived mostly on the basis of data for ^{1}H and ^{4}He.

Thus, experimental studies of electron screening for heavy ion projectiles are valuable for testing the accuracy of the screening models that were taken. A three element BaTiO thin film, with a thickness of less than 10 nm, was used as a test sample. By means of an RBS measurement using 2 MeV ^{4}He incident ions, for which the effect of screening on the cross-section is small, the ratio of Ba:Ti was determined to be 0.74 ± 0.02 keV. Then, the same sample was measured with TOF–ERDA by means of ^{35}Cl and ^{63}Cu beams in the energy range of 3.415–11.915 MeV. The scattering angle was 41.1°, and the sample was tilted to an angle of 20.5º. One experiment is shown in Fig. 87.

In the TOF–ERDA method, the major concerns are elemental losses during the measurement, detection efficiency for hydrogen, multiple scattering of the incident ion, and recoils and poorly known stopping forces. One additional factor is the scattering in the first carbon foil, which can play a major role in the case of heavy, low energy ions that can be deflected away from the detector. In this study, the elemental ratios were calculated using pure Rutherford cross-sections or with screened cross-sections, according to the Andersen et al. screening or from the ZBL universal potential. The two options with screening led to similar results, and only the Andersen et al. screening is shown.

Figure 88 shows the Ba:Ti ratio measured using a ^{35}Cl beam and the signal from the barium and titanium recoils. It is evident that the ratio is quite far from the one determined with RBS. When screening is included, the ratio improves, but it remains far from the expected ratio.

Figure 89 shows the same ratio determined from the forward scattered incident ^{35}Cl ions, leading to a ratio that is quite close to that of 0.74. With

increasing energy, the result improves. The stoichiometry determined becomes more barium poor, with lower beam energy. In this case, lower energy ^{35}Cl ions scattered from the titanium suffer more from the scattering in the first carbon foil; therefore, carbon foil scattering cannot explain the decreasing Ba:Ti ratio for lower energies.

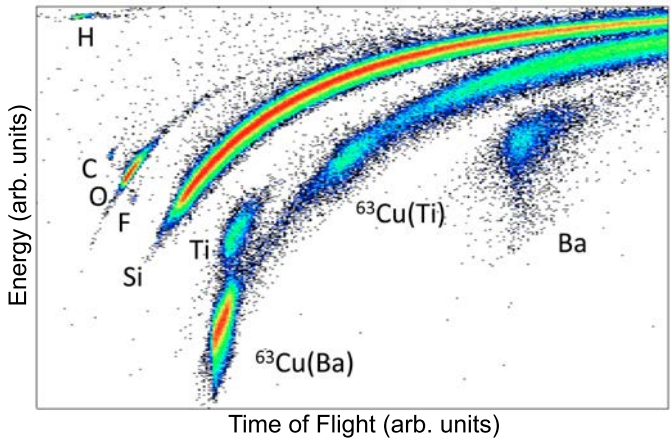

FIG. 87. Time of flight–E histogram from a thin BaTiO film on silicon measured with an 11.915 MeV ^{63}Cu beam. (Reproduced courtesy of the University of Jyväskylä.)

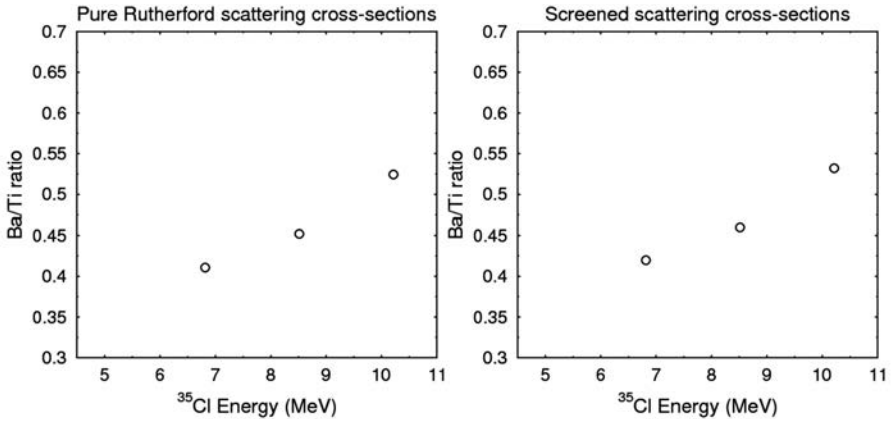

FIG. 88. Ba:Ti ratio as determined with barium and titanium recoils ejected by a ^{35}Cl beam. The ratio is far from the one (0.74) determined by ^{4}He Rutherford backscattering spectroscopy. (Reproduced courtesy of the University of Jyväskylä.)

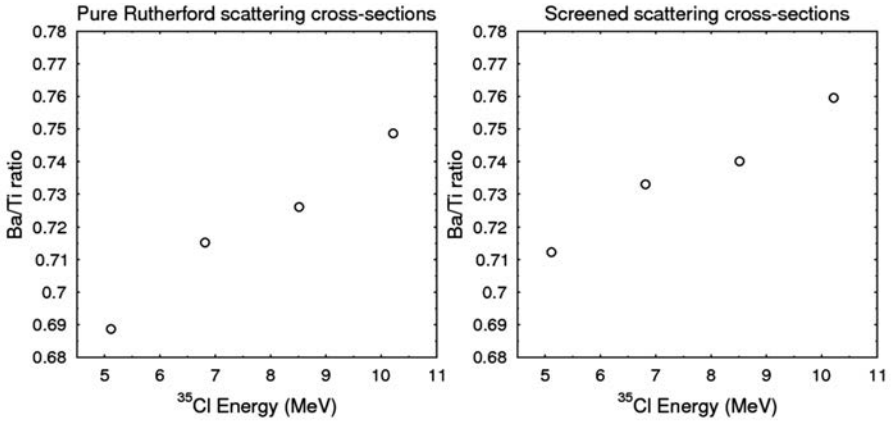

FIG. 89. Ba:Ti ratio as determined from ^{35}Cl beam ions that were scattered to the detector by barium and titanium sample atoms. The ratio is quite close to the one (0.74) determined by ^{4}He Rutherford backscattering spectroscopy. (Reproduced courtesy of the University of Jyväskylä.)

In any case, the screening effect should be stronger for the forward scattered ions than for the recoils. This is because recoils are produced from collisions that are nearly head on, leading to a smaller distance of closest approach, whereas forward scattering comes from collisions with a higher impact parameter (i.e. larger distance of closest approach), where screening is more important. However, it is observed that it is for the recoils that the Ba:Ti ratio changes the most.

The Ti:O ratio determined for measurements made with a ^{35}Cl beam is shown in Fig. 90; the ratio is very constant over the energy range. In Fig. 91, the same ratio was measured with a ^{63}Cu beam, and a much greater variation as a function of energy is observed. Higher energy measurements show a more titanium rich composition.

These results are only an indication that screening models, such as Andersen et al. screening and universal potential screening, may not be accurate enough for heavy ion ERDA. However, all the results were collected from the same sample; therefore, some systematic effect may be occurring. This could be preferential sputtering of one of the elements under the beam, issues with partial overlap of signals in the TOF–E histogram that may impact quantification or some effect attributable to the detection system, such as the first carbon foil or the detector efficiency for different ions and energies. A systematic study with other systems, samples and beams would be useful to clarify these issues.

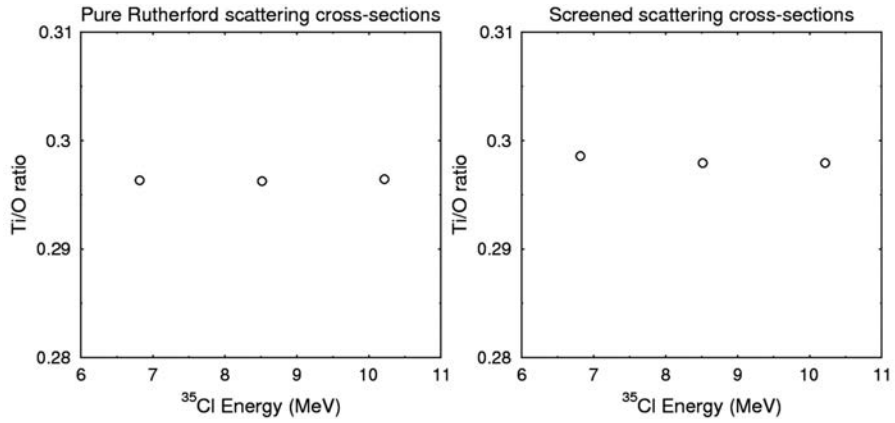

FIG. 90. Ti:O ratio determined from the recoils using an incident ^{35}Cl beam. (Reproduced courtesy of the University of Jyväskylä.)

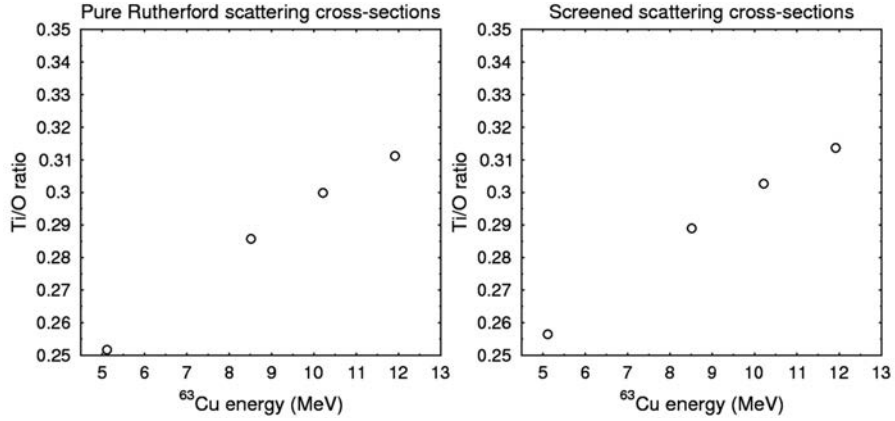

FIG. 91. Ti:O ratio determined from the recoils using an incident ^{63}Cu beam. (Reproduced courtesy of the University of Jyväskylä.)

9. RESULTS — IMPROVED MODELLING

9.1. IMPROVEMENT OF MONTE CARLO SIMULATIONS

9.1.1. Scope and objectives

Analytical data analysis codes have been used for many decades to analyse IBA data and are still the most widely used option [45]. New generation analytical codes include advanced models to describe the ion–target interaction, as well as effects occurring in the detection system. Nevertheless, the algorithms employed have limitations that originate from two main sources. First, many phenomena are treated either with approximate models or in a statistical manner, disregarding the details of the interactions. This includes, for instance, straggling, plural scattering and multiple scattering. In particular, the theory behind analytical, multiple scattering calculations breaks down at grazing angles [10]. Second, a detailed description of the detection system is normally not included.

In heavy ion ERDA, particularly given that the set-ups are usually more complex than for RBS or ^{4}He ERDA, these phenomena play a particularly important role, and currently available analytical codes may not be adequate for accurate data analysis [3].

The alternative is to develop a Monte Carlo simulation of the individual particle–particle interactions. Complex physical processes, as well as the full ion–detection system interaction, are taken into account in a natural way, without the approximations that standard codes involve. Ion–electron interactions are not calculated in Monte Carlo data analysis codes, and tabulated stopping powers, like the ones determined in this work, must be used.

MCERD is a Monte Carlo simulation program in binary collision approximation that takes multiple collisions between incident ions and target atoms into account [119, 120]. The code is used for simulations of ERDA measurements and includes multiple and plural scattering effects; it can be used for accurate analysis of concentration distributions in samples.

However, it has not been in widespread use outside of the laboratory where it was first developed. The main barrier has been the lack of a user friendly graphical interface as expert knowledge was needed to use the existing version.

The scope of this activity was to design and develop a user interface for MCERD and make it generally available to every IBA practitioner. The requirements were that the resulting software should be distributed under the terms of the GNU General Public License and that it should be possible to use it with different operating systems. The software was also to include sufficient installation and operating guidance.

9.1.2. Results and achievements

A new user interface for MCERD was developed by using a cross-platform widget toolkit for creating graphical user interfaces called GTK+ [121]. The toolkit is written in C language, so it is a good choice for this project because the original MCERD code, which is open source, is also written in C. GTK+ is licensed under the GNU Lesser General Public License, version 2.1, so the developed software can be distributed under the terms of the GNU General Public License. Users need GTK+, which can be downloaded from the Internet. Clear and easy to follow installation instructions are included with the software.

In simulations, MCERD code needs input parameters relating to the ion beam, detector, target and measurement geometry. One of the goals was that all the input parameters could be input through the user interface for easier use of the program. Figure 92 shows an example of how a user can set these parameters. The user interface also checks that the values given are between specific limits and provides some information related to the specific parameter.

After the simulation, the MCERD code generates data files containing the simulation results. The user interface plots the energy spectrum directly from the data files after the simulation. The energy spectrum of the specified element is generated in a new window, and this simulated energy spectrum can be compared with the experimental energy spectrum.

In the same window, the concentration distribution of the simulated element can be changed graphically using the mouse, which allows generation and visualization of the simulated energy spectrum in real time. The idea is to easily adjust the concentration distribution until the simulated energy spectrum corresponds to the experimental energy spectrum. A simulation and comparison is made for all the elements in the sample, and the depth profile of the sample can be created by combining the concentration distributions of all the elements.

The results from the example simulation are shown for an ERDA measurement of a C_xN_{1-x} foil on a silicon substrate with a ^{35}Cl ion beam simulated. The energy spectrum and concentration distribution window for carbon and oxygen are shown in Figs 93 and 94, respectively, and the depth profile obtained is shown in Fig. 95.

9.2. IMPROVEMENT OF ANALYTICAL SIMULATIONS

9.2.1. Scope and objectives

As discussed in Section 9.1.1, analytical data analysis codes face the challenge of evolving in order to be able to accurately analyse heavy ion ERDA

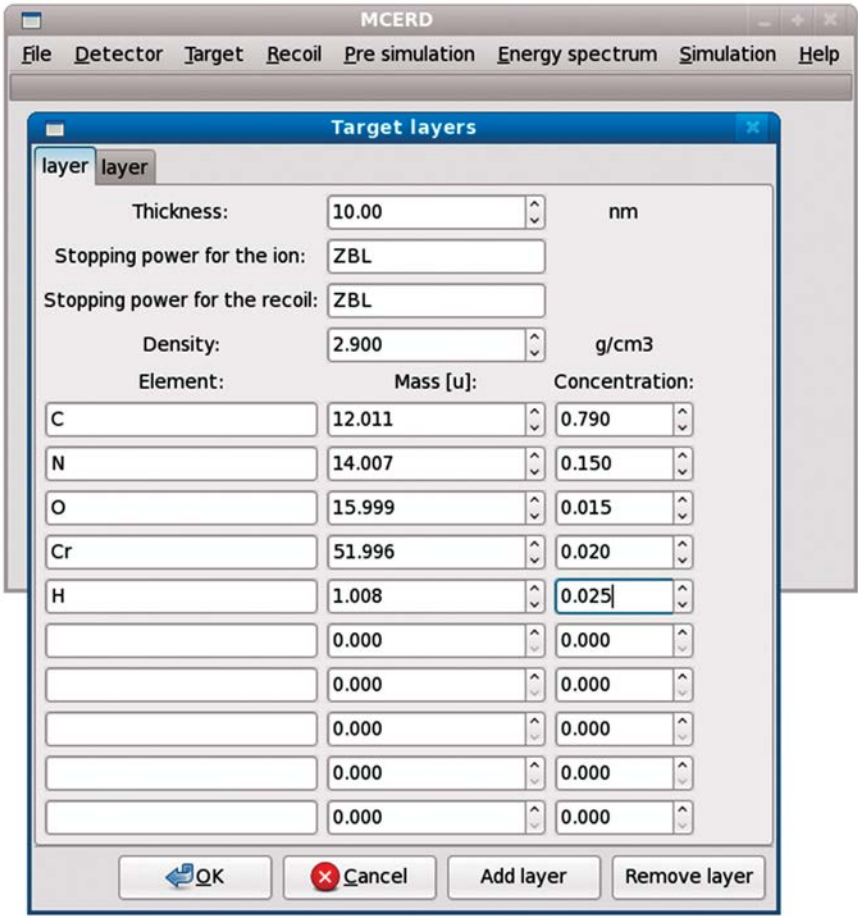

FIG. 92. Screenshot from the new MCERD user interface. The target layers window is shown and all the parameters relating to the target can be specified. (Reproduced courtesy of the University of Jyväskylä.)

data. In particular, the standard code for IBA data analysis, NDF [18], was one of the participants in the IAEA intercomparison of IBA software [3]. It includes advanced analytical models, but at the time of the IAEA intercomparison, it was clear that there was scope for improvement.

Given that Monte Carlo calculations are still comparatively slow, it would be highly desirable to have improved analytical simulations as well. This can be achieved by developing and implementing further advanced physics models in an existing code, such as NDF, which is in active development.

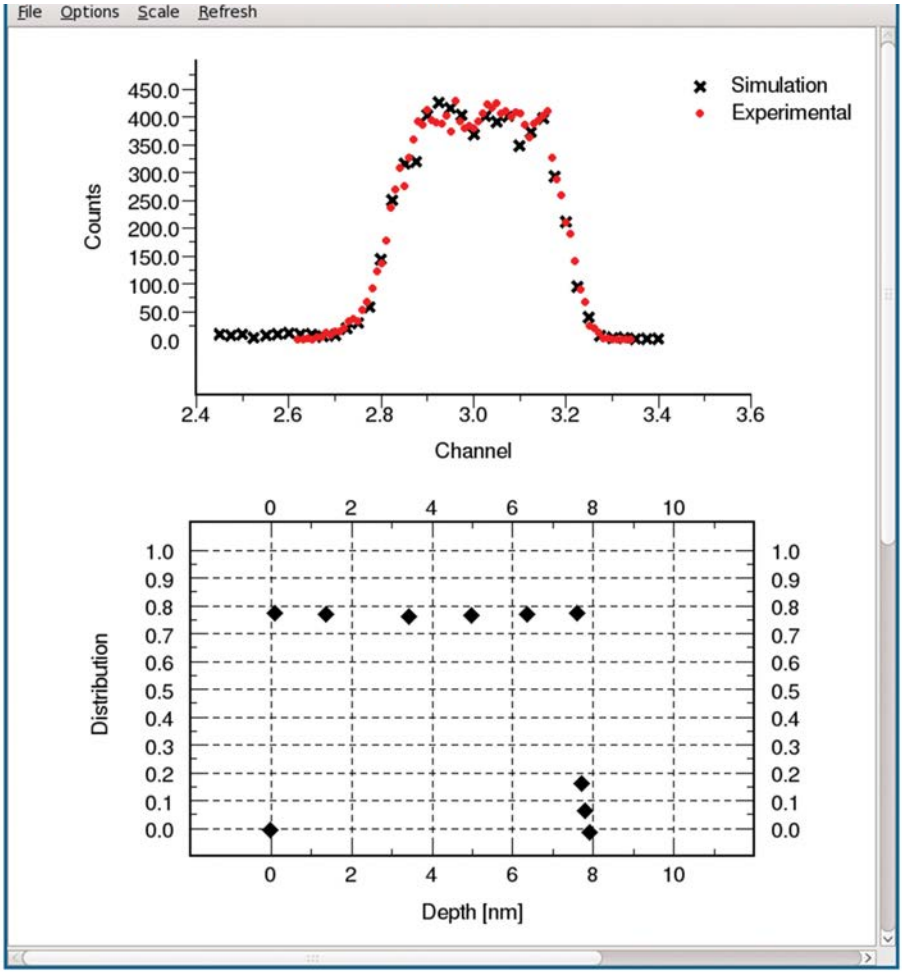

FIG. 93. Screenshot from the energy spectrum/concentration distribution window. Simulated and experimental spectra for carbon (above) and concentration distribution for carbon (below) are shown. (Reproduced courtesy of the University of Jyväskylä.)

9.2.2. Handling of stopping powers in the NDF code

IBA data analysis codes rely on schemes, such as SRIM, to calculate the stopping powers. In codes such as RUMP or SIMNRA, these stopping powers can be scaled by a constant factor across the whole energy range, but a completely different stopping power curve cannot be loaded. In particular, a given experimentally determined stopping power curve cannot be utilized in data

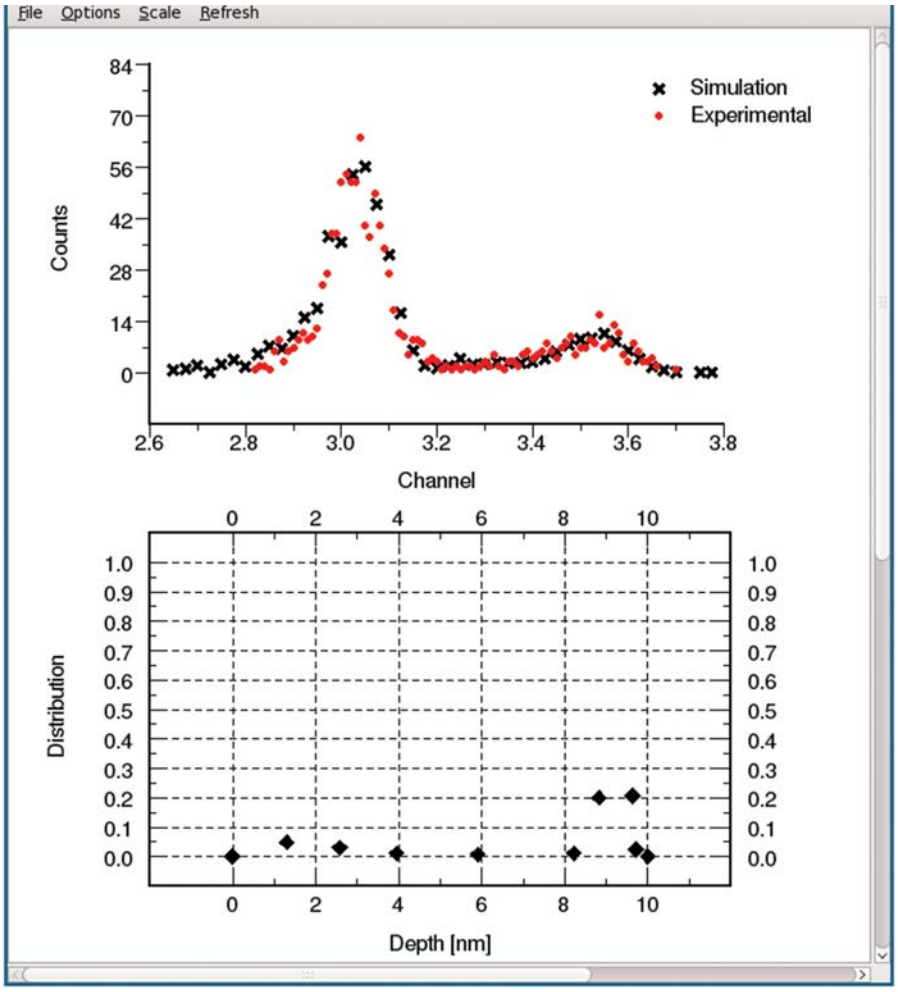

FIG. 94. Screenshot from the energy spectrum/concentration distribution window. Simulated and experimental spectra for oxygen (above) and concentration distribution for oxygen (below) are shown. (Reproduced courtesy of the University of Jyväskylä.)

analysis until it has been incorporated into SRIM. Even then, the weight given to the new measurement can be small because it is unclear whether the accuracy of each measurement is taken into account in the calculations made. This can be a severe barrier to using newly determined accurate stopping power values in the data analysis of real samples.

Furthermore, as a result of this project, it became clear that: (a) particularly for heavy ions, there are experimental values available as tabulated data that are

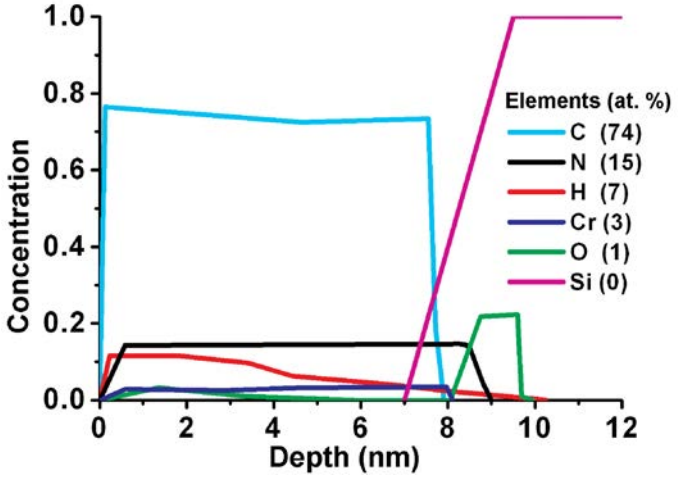

FIG. 95. Depth profile of the C_xN_{1-x} foil on a silicon substrate. Average concentrations are calculated (shown after each element). (Reproduced courtesy of the University of Jyväskylä.)

more accurate than SRIM, and (b) the capability of loading tabulated stopping power curves becomes essential. This possibility was introduced in NDF in a completely universal and flexible way. Any combination of interpolative schemes (including any version of SRIM) and of experimental data can be used simultaneously, so that the user can effectively choose which stopping power for which ion–target atom combination is to be used. This required major extensive changes in how the stopping power was handled internally in NDF. No other IBA data analysis currently has this capability.

The importance of this capability is illustrated in Fig. 48, in which RBS data, collected with a ^{12}C beam for an InN film on graphite with a gold marker layer on top, are shown. Simulations were made with NDF using SRIM stopping powers and the new stopping powers measured in this project. At high energy (15 MeV), the two simulations are very similar because the SRIM values agree well with the experimental data; at lower energies, increasingly large deviations are observed.

9.2.3. Implementation of double scattering in elastic recoil detection analysis

A long standing problem in IBA simulation is to be able to include multiple and plural scattering in an efficient way in the calculation of theoretical spectra. This calculation is important as it improves the accuracy of simulations and extends their range of applicability to more classes or problems. While multiple

and plural scattering are facets of the same phenomenon (i.e. that ions do not undergo one single collision in the sample), the distinction has proven useful. Conventionally, multiple scattering refers to many successive small angle scattering events, which can be treated in a statistical way. Plural scattering refers to the succession of a few large angle scattering events. Given that the scattering cross-section is small for large angle events, the probability of n successive large angle scattering events becomes much smaller as n increases. In many practical cases, double scattering ($n = 2$) accounts for most of the effect, which is a low energy background.

A new analytical model to calculate the influence of double scattering in ERDA spectra was developed and included in the NDF code [122]. This was unavailable prior to this CRP.

9.2.4. Non-ionizing losses in solid state (silicon) detectors

Extensive calculations of the pulse height defect and non-ionizing losses in silicon detectors [41] were made for many different incident ions and energies. On the basis of these calculations, a simple analytical model was developed and implemented in NDF in a user friendly way [69]. The user must only specify the thickness of the detector dead layer. It was shown that for heavy ion RBS this effect might be essential to obtain accurate simulations, particularly when multiple spectra are collected from the same sample and a simultaneous consistent fit to all data is needed. The same applies for heavy ion ERDA.

This was an essential point in the determination of stopping powers with the bulk sample method because the pulse height defect influences the height of the measured signals.

9.2.5. Non-Gaussian straggling

A non-Gaussian model for straggling near the surface (the most important region in ERDA) was developed, namely by introducing the gamma energy loss function [123]; this was first done for nuclear reaction analysis, where it is essential because of the very narrow resonances. It was then also implemented for ERDA and RBS.

9.2.6. Influence of multiple scattering on the width of Rutherford backscattering spectroscopy and elastic recoil detection analysis spectra

The most important effect of multiple scattering on IBA data is an extra contribution to energy spread. In fact, in grazing angle conditions, multiple

scattering can be the dominating component of energy spread. However, it has been shown by Bauer et al. [124], with Monte Carlo methods, that multiple scattering also induces a change in the yield of signals. A new analytical calculation was developed to calculate the effect of multiple scattering on the yield in RBS and ERDA spectra, and it was included in the NDF code [125].

9.2.7. The IAEA intercomparison of ion beam analysis software

The final results of the IAEA intercomparison of IBA software were published in 2007 [3]. Overall, the codes that participated showed good agreement, indicating that the fundamental simulation algorithms and calculations were correct. However, some issues remained outstanding. In some cases, improvements in some of the codes might be necessary. In the case of heavy ion ERDA using a heavy beam (^{127}I) at fairly low velocities (50 MeV or 0.4 MeV/nucleon), Monte Carlo calculations did not agree very well with the analytical codes and, in this case, the reasons were unclear. It was also unclear whether it was the Monte Carlo or the analytical calculations that needed improvement, or both.

The simulations made with MCERD, NDF and SIMNRA for simulation 12 of the IAEA intercomparison of IBA software is shown in Fig. 96. This was heavy ion ERDA with a 50 MeV $^{127}I^{10+}$ beam on a sample of silicon bulk/SiO_2 200 nm/gold 50 nm. It is clear that the simulation of the forward scattered beam is not equivalent in the Monte Carlo code or in NDF, and SIMNRA is even

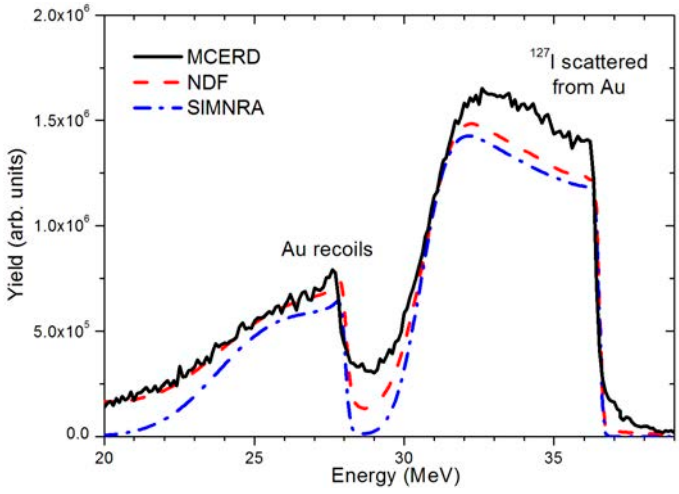

FIG. 96. Calculated curves corresponding to simulation 12 of the IAEA intercomparison of ion beam analysis software [3].

further away. However, in this complex case, the Monte Carlo simulation also has issues, including the scattering cross-section, which is heavily screened. In this simulation, no screening was used, and scattering events at very small angles have a large cross-section and could lead to some overestimation of the forward scattered yield. This is still a point that requires more research, ideally by comparing simulations with real data from well characterized structures.

For the gold recoils, for which screening has a much smaller role, the agreement between MCERD and NDF is excellent. Such an agreement is only possible with the new developments introduced.

10. CONCLUSIONS

The foremost objective of this CRP on the improvement of the reliability and accuracy of heavy ion beam nuclear analytical techniques was to deliver demonstrable improvements in the ability of heavy ion ERDA to analyse light elements and obtain a higher degree of reliability, accuracy and user confidence than had previously been possible. The CRP also had two specific research objectives: to improve the reliability and accuracy of software codes for heavy ion beam characterization of light elements in materials and to improve the reliability and accuracy of reference heavy ion stopping powers in selected elements.

These objectives were fully met. The stopping power was measured for 16 target materials and for 15 ions, for a total of 89 ion–target combinations. Of these combinations, 42 were thought to be completely new, with no previous experimental data available in the energy range measured. Furthermore, the binary materials used in the stopping power measurements are technologically important and widely used in the thin film industry. In many of the systems for which some data were already available, the new measurements allowed a better assessment to be made, sometimes because different sets of previously existing data did not agree well with one another or because it was previously unclear whether observed deviations from SRIM calculations were within the uncertainties of the measurements available.

When making comparisons with SRIM, depending on the ion as well as on the material, extremely good agreement was found in some cases, while large deviations were observed in some other systems. There is no apparent systematic method with which it can be foreseen when SRIM is incorrect. This is probably because of the very sparsely available datasets used to produce the SRIM model; therefore, the new results presented are a strong driving force for the improvement of the SRIM predictive capability for heavy ions. This should

lead to improvements in the models included in SRIM. Given the interpolative nature of SRIM, the benefits of the present results are expected to be extended to the prediction of stopping power for heavy ions in general.

A determined effort was made to provide realistic estimates of the uncertainties in the stopping powers measured. This is not often the case in published work, where uncertainties quoted are either not justified by an analysis of the sources of errors or they reflect only the statistical uncertainty of measured signals, which is seldom the dominant contribution. The bulk sample method in conjunction with a Bayesian inference data analysis directly provides uncertainties in the results obtained. The uncertainties in the results of the more widely used methods of transmission in thin films come from the uncertainty in the film thickness, including any thickness inhomogeneity, the accuracy of the determination of the average beam energy before and after crossing the film, the actual changing energy of the beam while inside the film, and the experimental parameters. In this case, the framework set by the GUM [56] of the Joint Committee for Guides in Metrology of the International Bureau of Weights and Measures for the evaluation of uncertainties was followed, and the recognized methods it describes were used. It was found that one critical source of uncertainty is the knowledge of the composition and homogeneity of the target. In samples in which the foil of interest was deposited onto a substrate, the uncertainty of the substrate thickness, as well as the uncertainty of the stopping power of the substrate for the incident ion also played a determinant role in the final accuracy of the experiment.

The software codes MCERD and NDF, a Monte Carlo and an analytical code, respectively, were improved under the aegis of this CRP. Monte Carlo simulations can, naturally, include all the relevant physics effects and, therefore, produce high quality simulations that are still not possible with analytical codes. MCERD, however, was previously used almost exclusively by its author and co-workers as it was a command line program without a graphical user interface. As a result of this CRP, a graphical user interface was developed for MCERD, which is now generally available to every IBA practitioner. The resulting software can be distributed under the terms of the GNU General Public License and can be operated by different operating systems. The software also includes sufficient installation and operating guidance, effectively making MCERD a new tool available to the entire IBA community for data analysis.

In parallel, new analytical models were developed and implemented in NDF, leading to a remarkable improvement in the accuracy of analytical simulations of heavy ion ERDA. In particular, no software was previously available that could directly use experimentally determined stopping powers; therefore, new measurements such as the ones presented here only led to an improvement in the simulations after they were included in the SRIM interpolative algorithms.

This possibility was introduced into NDF, a standard code for ion beam data analysis. This included the capability of treating compounds as such, using the experimental stopping power of given compounds in data analysis, instead of using elemental stopping powers together with the Bragg rule, which was hitherto the only possibility in all available codes. However, the former approach often led to deviations of up to 10–20%. Dramatically better agreement between experimental results and theoretical simulations was demonstrated by the simulations produced with the new stopping power values rather than with those previously available.

Finally, there has been substantial knowledge and technology transfer as a result of this CRP. An affordable and easy to implement TOF–ERDA telescope and data acquisition system has been developed at the University of Jyväskylä. The high performance (depth resolution down to 1 nm; all elements can be depth profiled) and the requirement of having only a small accelerator (with terminal voltage equal to or greater than 1 MV) make this technique available and attractive for smaller research laboratories that have no resources to do the development work by themselves. In the future, the aim of the ongoing development work is to also make gas ionization detectors and digitizing electronics available to other groups.

Substantial development of the heavy ion ERDA facility at iThemba LABS took place during the course of the CRP. A TOF spectrometer was assembled and adapted for stopping force measurements using the transmission technique. Development of the ERDA facility has increased research capacity at the tandem accelerator in Johannesburg; students and researchers from local universities can now perform thin film characterizations previously not possible with existing facilities. This has led to a research collaboration programme between iThemba LABS and the Algiers Nuclear Research Centre to measure stopping powers and energy loss straggling in polymeric foils, which has already led to joint publications.

Appendix

TABULATED DATA

In this Appendix, all the stopping cross-sections measured, including the uncertainties, within the scope of this CRP are given in Table 34 to facilitate inclusion in databases. In all cases, the units of energy are MeV/nucleon, the units of the stopping cross-sections are eV/(10^{15} at./cm^2) and the uncertainties are given in per cent, for a coverage k = 1, which corresponds to one standard deviation. Each dataset is identified by the target material, the ion and the participant.

Datasets that were continuous curves were discretized to enable them to be represented in tables. Ten equally spaced points were given for each order of magnitude, starting from the lowest energy probed and ending with the highest.

TABLE 34. STOPPING POWER DATA MEASURED WITHIN THE SCOPE OF THE CRP

System	Laboratory	Energy (MeV/nucleon)	ε (eV/(10^{15} at./cm^2)	Uncertainty (%)
^{58}Ni in carbon	Munich	0.676	777.9	5.1
		1.014	815.8	5.1
^{63}Cu in carbon	Munich	0.622	788.4	5.1
^{127}I in carbon	Munich	0.463	1146.8	5.1
		1.312	1531.8	5.1
^{197}Au in carbon	Munich	0.199	758.9	5.1
		0.398	1366.2	5.1
		0.597	1721.3	5.1
^{63}Cu in oxygen	Munich	0.622	883.5	11.2
^{127}I in oxygen	Munich	1.312	1700.5	11.2
^{197}Au in oxygen	Munich	0.199	814.4	11.2
^{58}Ni in aluminium	Munich	0.676	1026.0	5.1
		1.014	1191.8	5.1
^{63}Cu in aluminium	Munich	0.622	1115.9	5.1
^{27}I in aluminium	Munich	0.463	1447.2	5.1
		1.312	2356.7	5.1
^{197}Au in aluminium	Munich	0.199	949.4	5.1
		0.398	1760.8	5.1
		0.597	2195.4	5.1
^{4}He in silicon	Lisbon/RBI	0.050	63.4	4.5
		0.064	67.4	4.4
		0.083	69.9	4.1
		0.106	70.6	3.4
		0.136	69.5	2.5
		0.174	67.0	1.7
		0.223	63.4	2.1
		0.285	58.9	2.2
		0.365	53.6	1.9
		0.468	47.9	2.1
		0.600	41.9	3.1

TABLE 34. STOPPING POWER DATA MEASURED WITHIN THE SCOPE OF THE CRP (cont.)

System	Laboratory	Energy (MeV/nucleon)	ε (eV/(10^{15} at./cm^2)	Uncertainty (%)
^{7}Li in silicon	Lisbon/RBI	0.029	73.0	9.7
		0.037	78.4	7.9
		0.047	83.4	6.2
		0.060	87.8	4.7
		0.077	91.7	3.6
		0.098	95.0	2.9
		0.126	97.9	2.5
		0.160	100.1	2.1
		0.205	101.4	2.0
		0.262	101.4	2.1
		0.335	101.1	2.4
		0.428	98.5	2.8
^{11}B in silicon	Lisbon/RBI	0.018	79.2	7.9
		0.023	92.1	8.0
		0.030	101.8	7.4
		0.039	111.0	6.5
		0.050	121.8	5.6
		0.064	134.1	4.6
		0.083	147.5	3.5
		0.107	161.5	2.7
		0.137	175.5	3.1
		0.177	188.5	5.2

TABLE 34. STOPPING POWER DATA MEASURED WITHIN THE SCOPE OF THE CRP (cont.)

System	Laboratory	Energy (MeV/nucleon)	ε (eV/(10^{15} at./cm^2))	Uncertainty (%)
^{12}C in silicon	Lisbon/RBI	0.025	130.4	20.4
		0.032	141.2	16.6
		0.041	152.0	12.9
		0.053	163.5	10.0
		0.067	175.4	8.2
		0.086	187.9	7.1
		0.109	200.8	6.4
		0.139	213.9	6.7
		0.178	224.0	6.7
		0.227	229.9	6.1
		0.289	232.9	5.3
		0.369	233.1	4.8
		0.470	232.2	4.1
		0.599	229.5	4.4
		0.764	220.9	4.7
		0.975	208.5	5.0
		1.243	192.9	5.3
^{63}Cu in silicon	Munich	0.622	1229.1	5.1
^{127}I in silicon	Munich	1.312	2760.4	5.1
^{197}Au in silicon	Munich	0.199	1292.0	5.1
^{58}Ni in nickel	Munich	0.676	1861.4	5.1
		1.014	2173.3	5.1
^{127}I in nickel	Munich	0.463	2485.1	5.1
		1.312	4249.1	5.1
^{197}Au in nickel	Munich	0.398	2913.9	5.1
		0.597	3820.3	5.1
^{63}Cu in hafnium	Munich	0.622	2834.4	5.1
^{127}I in hafnium	Munich	1.312	6001.9	5.1
^{197}Au in hafnium	Munich	0.199	2248.0	5.1
^{58}Ni in gold	Munich	0.676	3368.8	5.1
		1.014	3859.4	5.1

TABLE 34. STOPPING POWER DATA MEASURED WITHIN THE SCOPE OF THE CRP (cont.)

System	Laboratory	Energy (MeV/nucleon)	ε (eV/(10^{15} at./cm^2))	Uncertainty (%)
^{127}I in gold	Munich	0.463	4546.3	5.1
		1.312	7391.8	5.1
^{197}Au in gold	Munich	0.398	5004.2	5.1
		0.597	6770.3	5.1
^{12}C in Al_2O_3	Helsinki	0.051	117.8	8.7
		0.064	131.1	8.4
		0.081	144.8	8.2
		0.102	158.6	8.0
		0.129	171.8	7.9
		0.163	184.0	7.9
		0.205	194.4	7.9
		0.259	202.3	7.9
		0.327	207.4	8.0
		0.413	209.2	8.1
		0.521	208.0	8.3
		0.657	203.8	8.5
		0.830	197.1	8.8
		1.047	188.5	9.2

TABLE 34. STOPPING POWER DATA MEASURED WITHIN THE SCOPE OF THE CRP (cont.)

System	Laboratory	Energy (MeV/nucleon)	ε (eV/(10^{15} at./cm^2)	Uncertainty (%)
^{12}C in Al_2O_3	iThemba LABS	0.162	183.3	7.5
		0.179	187.4	7.5
		0.210	192.7	7.5
		0.248	196.2	7.5
		0.282	197.6	7.5
		0.307	193.0	7.5
		0.321	193.5	7.5
		0.346	191.7	7.5
		0.377	187.9	7.5
		0.394	197.3	7.5
		0.431	183.4	7.5
		0.463	189.7	7.5
		0.466	200.7	7.5
		0.496	186.2	7.5
		0.529	191.3	7.5
		0.568	185.3	7.5
^{12}C in Al_2O_3	Jyväskylä	0.120	144.7	13.7
		0.256	173.6	12.8
		0.394	174.8	13.0
		0.532	162.4	15.0

TABLE 34. STOPPING POWER DATA MEASURED WITHIN THE SCOPE OF THE CRP (cont.)

System	Laboratory	Energy (MeV/nucleon)	ε (eV/(10^{15} at./cm^2))	Uncertainty (%)
^{16}O in Al_2O_3	Helsinki	0.032	114.2	9.1
		0.041	127.8	8.9
		0.052	143.2	8.6
		0.066	160.6	8.4
		0.083	179.7	8.2
		0.105	200.2	8.0
		0.133	221.5	7.9
		0.169	242.4	7.9
		0.213	261.6	7.9
		0.270	277.4	7.9
		0.342	288.5	8.0
		0.433	293.6	8.1
		0.548	292.4	8.3
		0.694	285.1	8.5
		0.878	272.6	8.9
^{16}O in Al_2O_3	iThemba LABS	0.154	210.7	7.5
		0.172	222.1	7.5
		0.202	236.6	7.5
		0.220	243.5	7.5
		0.244	249.0	7.5
		0.262	249.6	7.5
		0.282	263.0	7.5
		0.300	275.7	7.5
		0.320	276.9	7.5
		0.337	277.9	7.5
		0.374	292.7	7.5
		0.394	294.2	7.5
		0.413	306.5	7.5
		0.445	291.2	7.5
		0.466	307.0	7.5
		0.502	300.2	7.5

TABLE 34. STOPPING POWER DATA MEASURED WITHIN THE SCOPE OF THE CRP (cont.)

System	Laboratory	Energy (MeV/nucleon)	ε (eV/(10^{15} at./cm^2)	Uncertainty (%)
^{28}Si in Al_2O_3	iThemba LABS	0.139	309.4	7.5
		0.157	352.4	7.5
		0.175	379.5	7.5
		0.195	370.2	7.5
		0.215	411.3	7.5
		0.234	423.6	7.5
		0.251	441.6	7.5
		0.269	437.0	7.5
		0.285	456.8	7.5
		0.301	461.9	7.5
		0.318	467.0	7.5
		0.333	470.9	7.5
		0.349	489.0	7.5
		0.364	481.2	7.5
		0.381	503.5	7.5
		0.439	522.8	7.5
		0.456	528.8	7.5
		0.470	497.9	7.5
		0.501	517.9	7.5
		0.526	498.0	7.5
		0.557	535.8	7.5
		0.572	527.4	7.5
		0.600	519.4	7.5
		0.614	541.9	7.5

TABLE 34. STOPPING POWER DATA MEASURED WITHIN THE SCOPE OF THE CRP (cont.)

System	Laboratory	Energy (MeV/nucleon)	ε (eV/(10^{15} at./cm^2))	Uncertainty (%)
^{35}Cl in Al_2O_3	Helsinki	0.018	204.6	9.6
		0.023	215.5	9.4
		0.030	229.4	9.2
		0.038	246.9	9.0
		0.049	268.6	8.7
		0.062	295.0	8.5
		0.079	326.7	8.2
		0.101	364.1	8.0
		0.129	406.9	7.9
		0.165	454.8	7.9
		0.210	506.3	7.9
		0.268	559.1	7.9
		0.342	609.8	8.0
		0.437	654.1	8.1
		0.558	687.6	8.3
^{35}Cl in Al_2O_3	Jyväskylä	0.013	128.4	12.6
		0.036	184.7	12.3
		0.077	259.1	11.8
		0.119	308.6	11.5
		0.160	373.5	11.3
		0.203	412.8	11.2
		0.246	459.3	11.3
^{35}Cl in Al_2O_3	Munich	0.980	745.8	6.1
^{58}Ni in Al_2O_3	Munich	1.013	1295.0	6.1

TABLE 34. STOPPING POWER DATA MEASURED WITHIN THE SCOPE OF THE CRP (cont.)

System	Laboratory	Energy (MeV/nucleon)	ε (eV/(10^{15} at./cm^2))	Uncertainty (%)
^{79}Br in Al_2O_3	Helsinki	0.041	244.4	8.9
		0.051	286.9	8.6
		0.065	338.5	8.4
		0.082	400.7	8.2
		0.104	474.3	8.0
		0.131	559.8	7.9
		0.165	656.2	7.9
		0.209	760.9	7.9
		0.264	869.0	7.9
		0.333	974.0	8.0
		0.421	1068.1	8.1
		0.531	1143.3	8.3
^{79}Br in Al_2O_3	Munich	0.491	1249.0	6.1
^{127}I in Al_2O_3	Helsinki	0.040	320.4	8.9
		0.052	351.3	8.6
		0.066	393.8	8.4
		0.084	451.7	8.2
		0.108	530.7	8.0
		0.138	638.3	7.9
		0.177	783.5	7.9
		0.226	973.8	7.9
		0.289	1201.4	7.9

TABLE 34. STOPPING POWER DATA MEASURED WITHIN THE SCOPE OF THE CRP (cont.)

System	Laboratory	Energy (MeV/nucleon)	ε (eV/(10^{15} at./cm^2)	Uncertainty (%)
^{12}C in SiO_2	iThemba LABS	0.178	200.0	7.5
		0.197	205.9	7.5
		0.216	205.9	7.5
		0.255	212.5	7.5
		0.273	210.3	7.5
		0.292	209.9	7.5
		0.310	214.3	7.5
		0.327	202.0	7.5
		0.345	203.3	7.5
		0.379	197.6	7.5
		0.396	202.6	7.5
		0.413	199.1	7.5
		0.465	198.5	7.5
		0.498	195.3	7.5
		0.519	191.1	7.5
		0.581	190.5	7.5

TABLE 34. STOPPING POWER DATA MEASURED WITHIN THE SCOPE OF THE CRP (cont.)

System	Laboratory	Energy (MeV/nucleon)	ε (eV/(10^{15} at./cm^2))	Uncertainty (%)
^{28}Si in SiO_2	iThemba LABS	0.146	359.9	7.5
		0.165	384.0	7.5
		0.172	412.6	7.5
		0.185	416.0	7.5
		0.203	448.2	7.5
		0.215	441.6	7.5
		0.220	476.6	7.5
		0.231	485.9	7.5
		0.245	488.0	7.5
		0.262	504.6	7.5
		0.279	516.3	7.5
		0.295	503.7	7.5
		0.312	528.6	7.5
		0.329	531.6	7.5
		0.344	539.4	7.5
		0.361	541.9	7.5
		0.374	531.9	7.5
		0.391	530.5	7.5
		0.407	564.4	7.5
		0.423	536.8	7.5
		0.444	555.6	7.5
		0.461	566.1	7.5
		0.478	554.0	7.5
		0.504	552.6	7.5

TABLE 34. STOPPING POWER DATA MEASURED WITHIN THE SCOPE OF THE CRP (cont.)

System	Laboratory	Energy (MeV/nucleon)	ε (eV/(10^{15} at./cm^2)	Uncertainty (%)
^{4}He in TiO_2	Lisbon/RBI	0.025	36.0	16.9
		0.032	39.3	14.7
		0.041	42.8	12.6
		0.052	46.3	10.9
		0.066	49.8	9.6
		0.085	53.0	8.3
		0.108	55.6	6.9
		0.138	57.6	5.0
		0.176	58.2	3.8
		0.225	57.1	3.1
		0.288	54.8	2.7
		0.368	51.5	2.7
		0.470	47.2	3.0
		0.600	42.4	3.3
^{11}B in TiO_2	Lisbon/RBI	0.019	64.3	8.2
		0.024	74.4	8.3
		0.031	83.4	7.8
		0.040	93.4	7.2
		0.051	105.2	6.7
		0.065	118.4	6.2
		0.084	132.9	5.5
		0.108	147.9	4.6
		0.138	162.4	3.6
		0.177	175.5	3.7
		0.227	186.1	5.7

TABLE 34. STOPPING POWER DATA MEASURED WITHIN THE SCOPE OF THE CRP (cont.)

System	Laboratory	Energy (MeV/nucleon)	ε (eV/(10^{15} at./cm^2)	Uncertainty (%)
^{12}C in TiO_2	Lisbon/RBI	0.049	122.5	3.4
		0.062	136.1	3.1
		0.079	149.8	3.2
		0.100	163.2	3.3
		0.126	176.0	3.4
		0.160	187.7	3.4
		0.202	198.0	3.3
		0.255	206.2	3.3
		0.323	211.8	3.3
		0.408	214.7	3.3
		0.516	216.5	3.3
		0.653	213.0	3.3
		0.826	204.3	3.3
^{16}O in TiO_2	Lisbon/RBI	0.019	100.1	3.7
		0.025	115.8	3.7
		0.031	130.4	3.9
		0.040	145.9	4.1
		0.051	161.8	4.3
		0.065	177.7	4.3
		0.082	193.0	4.0
		0.105	207.8	3.4
		0.134	222.2	2.9
		0.171	236.1	2.6
		0.217	249.0	2.8
		0.277	260.0	3.1
		0.353	268.1	3.5
		0.450	273.5	3.8
		0.574	278.2	4.1
		0.731	275.8	4.4

TABLE 34. STOPPING POWER DATA MEASURED WITHIN THE SCOPE OF THE CRP (cont.)

System	Laboratory	Energy (MeV/nucleon)	ε (eV/(10^{15} at./cm^2)	Uncertainty (%)
^{12}C in ZrO_2	iThemba LABS	0.200	268.8	7.5
		0.233	275.0	7.5
		0.251	280.6	7.5
		0.266	281.6	7.5
		0.284	282.2	7.5
		0.307	276.5	7.5
		0.343	278.4	7.5
		0.376	279.0	7.5
		0.408	270.7	7.5
		0.427	269.4	7.5
		0.445	262.2	7.5
		0.472	259.4	7.5
		0.490	269.4	7.5
		0.511	262.1	7.5
		0.526	265.5	7.5
		0.548	253.9	7.5
		0.568	252.2	7.5
		0.594	242.4	7.5
		0.621	257.7	7.5

TABLE 34. STOPPING POWER DATA MEASURED WITHIN THE SCOPE OF THE CRP (cont.)

System	Laboratory	Energy (MeV/nucleon)	ε (eV/(10^{15} at./cm^2)	Uncertainty (%)
^{16}O in ZrO_2	iThemba LABS	0.164	331.2	7.5
		0.186	342.8	7.5
		0.207	357.1	7.5
		0.226	370.0	7.5
		0.251	375.4	7.5
		0.276	384.5	7.5
		0.301	402.3	7.5
		0.327	404.8	7.5
		0.350	400.1	7.5
		0.372	404.6	7.5
		0.392	394.9	7.5
		0.416	398.0	7.5
		0.436	394.1	7.5
		0.478	407.6	7.5
		0.498	386.6	7.5
		0.526	400.2	7.5
		0.551	367.2	7.5
		0.573	371.9	7.5
		0.598	377.9	7.5
		0.628	358.9	7.5

TABLE 34. STOPPING POWER DATA MEASURED WITHIN THE SCOPE OF THE CRP (cont.)

System	Laboratory	Energy (MeV/nucleon)	ε (eV/(10^{15} at./cm^2))	Uncertainty (%)
^{19}F in ZrO_2	iThemba LABS	0.141	331.6	7.5
		0.161	357.2	7.5
		0.178	372.0	7.5
		0.197	388.7	7.5
		0.218	406.7	7.5
		0.239	416.7	7.5
		0.262	426.6	7.5
		0.284	440.2	7.5
		0.305	437.6	7.5
		0.323	438.4	7.5
		0.342	451.0	7.5
		0.361	445.4	7.5
		0.380	450.3	7.5
		0.397	447.1	7.5
		0.414	432.8	7.5
		0.435	441.4	7.5
		0.454	437.5	7.5
		0.477	437.7	7.5
		0.500	437.6	7.5
		0.520	430.6	7.5
		0.552	431.1	7.5

TABLE 34. STOPPING POWER DATA MEASURED WITHIN THE SCOPE OF THE CRP (cont.)

System	Laboratory	Energy (MeV/nucleon)	ε (eV/(10^{15} at./cm^2))	Uncertainty (%)
^{24}Mg in ZrO_2	iThemba LABS	0.136	407.1	7.5
		0.150	445.8	7.5
		0.166	465.1	7.5
		0.180	490.4	7.5
		0.197	513.8	7.5
		0.209	522.0	7.5
		0.221	538.2	7.5
		0.241	551.6	7.5
		0.259	568.0	7.5
		0.277	583.2	7.5
		0.292	581.8	7.5
		0.310	596.1	7.5
		0.328	596.3	7.5
		0.347	617.6	7.5
		0.362	625.9	7.5
		0.376	612.0	7.5
		0.406	608.3	7.5
		0.423	624.7	7.5
		0.440	626.6	7.5
		0.454	627.1	7.5
		0.471	628.6	7.5
		0.481	624.2	7.5
		0.498	626.3	7.5

TABLE 34. STOPPING POWER DATA MEASURED WITHIN THE SCOPE OF THE CRP (cont.)

System	Laboratory	Energy (MeV/nucleon)	ε (eV/(10^{15} at./cm^2)	Uncertainty (%)
^{27}Al in ZrO_2	iThemba LABS	0.129	418.1	7.5
		0.142	459.5	7.5
		0.157	483.2	7.5
		0.173	505.2	7.5
		0.190	534.2	7.5
		0.208	565.5	7.5
		0.227	588.8	7.5
		0.243	591.4	7.5
		0.258	604.3	7.5
		0.274	625.6	7.5
		0.289	619.2	7.5
		0.303	639.0	7.5
		0.316	631.6	7.5
		0.331	645.7	7.5
		0.347	660.3	7.5
		0.364	660.6	7.5
		0.382	664.8	7.5
		0.400	671.6	7.5
		0.415	657.3	7.5
		0.433	664.5	7.5
		0.453	657.4	7.5
		0.473	677.4	7.5
		0.482	668.0	7.5

TABLE 34. STOPPING POWER DATA MEASURED WITHIN THE SCOPE OF THE CRP (cont.)

System	Laboratory	Energy (MeV/nucleon)	ε (eV/(10^{15} at./cm^2)	Uncertainty (%)
^{12}C in Ta_2O_5	Helsinki	0.048	170.4	8.7
		0.061	180.7	8.5
		0.076	193.0	8.3
		0.096	207.3	8.1
		0.121	223.8	7.9
		0.153	241.9	7.9
		0.193	261.0	7.9
		0.243	279.3	7.9
		0.307	294.3	8.0
		0.387	302.9	8.1
		0.488	302.4	8.2
		0.615	291.2	8.4
		0.776	270.2	8.7
^{12}C in Ta_2O_5	Lisbon/RBI	0.136	203.7	5.1
		0.174	227.5	4.6
		0.223	247.7	4.8
		0.285	262.4	5.2
		0.364	270.7	5.5
		0.466	275.8	5.6
		0.596	274.6	5.5
		0.762	265.4	5.5
		0.974	251.0	5.6
		1.246	232.4	5.7

TABLE 34. STOPPING POWER DATA MEASURED WITHIN THE SCOPE OF THE CRP (cont.)

System	Laboratory	Energy (MeV/nucleon)	ε (eV/(10^{15} at./cm^2)	Uncertainty (%)
^{16}O in Ta_2O_5	Helsinki	0.034	162.2	9.1
		0.043	175.8	8.8
		0.055	192.0	8.6
		0.069	211.2	8.4
		0.087	233.8	8.2
		0.110	260.0	8.0
		0.138	289.6	7.9
		0.174	321.7	7.9
		0.219	353.9	7.9
		0.276	382.5	7.9
		0.348	402.9	8.0
		0.439	410.4	8.2
		0.553	402.5	8.3
		0.697	379.6	8.6
		0.878	345.6	8.9
^{16}O in Ta_2O_5	Lisbon/RBI	0.084	200.3	5.4
		0.107	231.9	5.4
		0.136	264.3	5.4
		0.173	295.7	5.3
		0.221	324.2	5.4
		0.281	348.5	5.5
		0.357	367.2	5.6
		0.455	381.0	5.8
		0.579	392.1	6.0
		0.736	391.9	6.1
		0.937	380.4	6.2

TABLE 34. STOPPING POWER DATA MEASURED WITHIN THE SCOPE OF THE CRP (cont.)

System	Laboratory	Energy (MeV/nucleon)	ε (eV/(10^{15} at./cm^2)	Uncertainty (%)
^{35}Cl in Ta_2O_5	Helsinki	0.019	149.8	9.6
		0.025	177.1	9.4
		0.031	209.1	9.2
		0.040	246.3	8.9
		0.051	289.6	8.7
		0.065	339.3	8.4
		0.082	395.8	8.2
		0.105	458.8	8.0
		0.133	527.3	7.9
		0.170	599.4	7.9
		0.216	671.3	7.9
		0.275	738.0	7.9
		0.351	793.3	8.0
		0.446	831.3	8.2
		0.568	847.8	8.3
^{35}Cl in Ta_2O_5	Lisbon/RBI	0.047	241.2	5.0
		0.059	284.5	4.8
		0.075	333.3	4.7
		0.095	390.0	4.6
		0.119	450.2	4.6
		0.151	517.3	4.4
		0.190	593.1	4.2
		0.240	672.2	4.2
		0.303	747.8	4.7
		0.382	818.0	5.4
		0.482	884.2	6.1
		0.608	940.1	6.6
		0.768	972.6	7.0
^{35}Cl in Ta_2O_5	Munich	0.975	1037.6	4.1

TABLE 34. STOPPING POWER DATA MEASURED WITHIN THE SCOPE OF THE CRP (cont.)

System	Laboratory	Energy (MeV/nucleon)	ε (eV/(10^{15} at./cm^2))	Uncertainty (%)
^{79}Br in Ta_2O_5	Helsinki	0.041	377.2	8.9
		0.052	424.4	8.6
		0.066	482.2	8.4
		0.083	552.4	8.2
		0.105	637.1	8.0
		0.133	738.3	7.9
		0.167	858.1	7.9
		0.211	998.1	7.9
		0.267	1159.9	7.9
		0.337	1344.7	8.0
		0.425	1553.6	8.1
		0.536	1788.7	8.3
^{79}Br in Ta_2O_5	Munich	0.487	1758.0	4.1
^{127}I in Ta_2O_5	Helsinki	0.035	481.8	9.0
		0.045	532.8	8.8
		0.056	592.6	8.6
		0.071	662.2	8.3
		0.090	742.8	8.1
		0.114	836.0	8.0
		0.144	945.3	7.9
		0.181	1077.0	7.9
		0.229	1243.2	7.9
		0.289	1625.2	7.9

TABLE 34. STOPPING POWER DATA MEASURED WITHIN THE SCOPE OF THE CRP (cont.)

System	Laboratory	Energy (MeV/nucleon)	ε (eV/(10^{15} at./cm^2))	Uncertainty (%)
^{12}C in Si_3N_4	Helsinki	0.036	122.8	7.6
		0.045	135.2	7.3
		0.058	148.2	7.1
		0.073	161.5	6.8
		0.094	174.8	6.6
		0.119	187.4	6.4
		0.152	198.8	6.3
		0.193	208.3	6.3
		0.246	215.1	6.3
		0.314	218.8	6.4
		0.400	219.0	6.5
		0.509	215.6	6.7
		0.649	209.0	7.0
		0.826	199.5	7.4
^{12}C in Si_3N_4	Jyväskylä	0.017	93.4	9.3
		0.037	127.4	7.5
		0.088	179.0	5.7
		0.133	205.3	5.1
		0.202	224.8	5.4
		0.272	226.7	5.6
		0.339	232.7	5.7
		0.410	223.9	5.7
		0.476	207.3	7.2
		0.545	210.7	6.4
		0.611	214.2	6.3
		0.680	205.7	7.7

TABLE 34. STOPPING POWER DATA MEASURED WITHIN THE SCOPE OF THE CRP (cont.)

System	Laboratory	Energy (MeV/nucleon)	ε (eV/(10^{15} at./cm^2)	Uncertainty (%)
^{12}C in Si_3N_4	iThemba LABS	0.156	218.9	6.0
		0.168	221.5	5.9
		0.183	215.8	5.7
		0.198	227.7	5.6
		0.218	227.2	5.5
		0.240	225.3	5.4
		0.262	230.0	5.2
		0.288	232.6	5.2
		0.316	227.7	5.1
		0.338	236.0	5.0
		0.379	235.8	4.9
		0.421	221.3	4.8
^{16}O in Si_3N_4	Helsinki	0.021	118.3	8.1
		0.026	128.9	7.9
		0.034	141.7	7.6
		0.043	156.9	7.4
		0.055	174.9	7.1
		0.070	195.7	6.9
		0.089	219.0	6.6
		0.114	244.1	6.4
		0.145	269.5	6.3
		0.186	293.1	6.3
		0.237	312.2	6.3
		0.302	324.1	6.4
		0.386	326.6	6.5

TABLE 34. STOPPING POWER DATA MEASURED WITHIN THE SCOPE OF THE CRP (cont.)

System	Laboratory	Energy (MeV/nucleon)	ε (eV/(10^{15} at./cm^2)	Uncertainty (%)
^{16}O in Si_3N_4	Jyväskylä	0.016	101.3	9.0
		0.028	128.1	8.3
		0.057	181.6	6.9
		0.098	237.3	5.7
		0.148	279.4	5.0
		0.200	309.9	4.9
		0.250	323.6	5.2
		0.302	330.2	5.7
		0.352	334.9	6.1
		0.404	333.5	6.3
		0.454	328.9	6.4
		0.505	326.3	6.4
^{16}O in Si_3N_4	iThemba LABS	0.132	253.9	6.3
		0.159	274.7	6.0
		0.188	287.4	5.7
		0.221	299.5	5.5
		0.252	316.0	5.3
		0.299	310.7	5.1
		0.348	312.2	5.0
		0.388	315.2	4.9
		0.431	308.1	4.8

TABLE 34. STOPPING POWER DATA MEASURED WITHIN THE SCOPE OF THE CRP (cont.)

System	Laboratory	Energy (MeV/nucleon)	ε (eV/(10^{15} at./cm^2))	Uncertainty (%)
^{28}Si in Si_3N_4	iThemba LABS	0.127	377.9	6.4
		0.136	374.6	6.2
		0.148	400.7	6.1
		0.159	403.5	6.0
		0.171	402.6	5.8
		0.184	433.4	5.7
		0.198	441.1	5.6
		0.213	460.0	5.5
		0.228	486.1	5.4
		0.241	473.6	5.3
		0.256	472.3	5.3
		0.274	479.3	5.2
		0.290	504.5	5.2
		0.299	506.2	5.1
		0.311	515.0	5.1
^{35}Cl in Si_3N_4	Helsinki	0.015	215.0	8.3
		0.019	226.9	8.1
		0.024	242.2	7.9
		0.031	261.5	7.7
		0.040	285.4	7.5
		0.050	314.4	7.2
		0.064	349.0	7.0
		0.082	389.5	6.7
		0.104	435.9	6.5
		0.132	487.7	6.4
		0.168	544.0	6.3
		0.214	603.1	6.3
		0.273	662.6	6.3
		0.348	719.6	6.4
		0.442	770.6	6.6
		0.563	812.2	6.8

TABLE 34. STOPPING POWER DATA MEASURED WITHIN THE SCOPE OF THE CRP (cont.)

System	Laboratory	Energy (MeV/nucleon)	ε (eV/(10^{15} at./cm^2))	Uncertainty (%)
^{35}Cl in Si_3N_4	Jyväskylä	0.017	170.3	9.0
		0.028	210.7	8.3
		0.043	257.0	7.5
		0.088	374.1	5.9
		0.133	465.3	5.1
		0.177	540.1	4.9
		0.222	600.1	5.0
		0.267	648.5	5.4
		0.311	681.5	5.8
^{35}Cl in Si_3N_4	Munich	0.992	790.9	3.3
		0.998	791.2	3.3
^{58}Ni in Si_3N_4	Munich	1.026	1377.0	3.3
		1.033	1440.0	3.3
^{79}Br in Si_3N_4	Helsinki	0.038	366.4	7.5
		0.048	439.6	7.3
		0.061	520.5	7.0
		0.078	608.1	6.7
		0.099	700.7	6.5
		0.127	797.0	6.4
		0.161	895.8	6.3
		0.205	996.8	6.3
		0.261	1101.6	6.3
		0.332	1215.8	6.4
		0.423	1356.6	6.6
		0.538	1594.4	6.8
^{79}Br in Si_3N_4	Munich	0.500	1401.0	3.3
		0.505	1397.0	3.3

TABLE 34. STOPPING POWER DATA MEASURED WITHIN THE SCOPE OF THE CRP (cont.)

System	Laboratory	Energy (MeV/nucleon)	ε (eV/(10^{15} at./cm^2)	Uncertainty (%)
^{127}I in Si_3N_4	Helsinki	0.032	485.8	7.7
		0.041	606.6	7.4
		0.053	742.2	7.2
		0.067	886.6	6.9
		0.086	1031.0	6.7
		0.110	1165.7	6.5
		0.140	1281.2	6.3
		0.179	1370.5	6.3
		0.229	1429.7	6.3
		0.292	1458.6	6.4
^{4}He in GaN	Lisbon/RBI	0.143	60.3	2.5
		0.180	62.0	2.3
		0.227	61.8	2.3
		0.286	59.6	2.3
		0.361	55.7	2.2
		0.455	50.7	2.2
		0.575	45.3	2.5
^{12}C in GaN	Lisbon/RBI	0.073	138.9	5.6
		0.092	157.1	4.8
		0.117	175.8	3.9
		0.148	194.1	3.1
		0.187	211.3	2.8
		0.238	226.9	3.2
		0.301	240.5	3.9
		0.382	251.2	4.5
		0.484	262.0	5.0
		0.613	267.5	5.3
		0.777	265.5	5.4
		0.986	258.0	5.5

TABLE 34. STOPPING POWER DATA MEASURED WITHIN THE SCOPE OF THE CRP (cont.)

System	Laboratory	Energy (MeV/nucleon)	ε (eV/(10^{15} at./cm^2)	Uncertainty (%)
^{16}O in GaN	Lisbon/RBI	0.037	142.8	4.9
		0.046	161.1	4.7
		0.058	180.9	4.4
		0.074	201.6	4.0
		0.093	222.1	3.7
		0.117	242.0	3.5
		0.147	261.4	3.3
		0.186	280.7	3.2
		0.234	300.0	3.2
		0.295	318.9	3.3
		0.371	336.1	3.4
		0.468	352.7	3.5
		0.590	368.0	3.6
		0.743	374.7	3.7
		0.936	372.2	3.7
^{4}He in InN	Lisbon/RBI	0.096	76.5	4.6
		0.124	79.5	3.1
		0.160	81.0	2.3
		0.207	80.7	2.5
		0.267	78.3	2.6
		0.345	73.9	2.5
		0.445	67.9	2.3

TABLE 34. STOPPING POWER DATA MEASURED WITHIN THE SCOPE OF THE CRP (cont.)

System	Laboratory	Energy (MeV/nucleon)	ε (eV/(10^{15} at./cm^2)	Uncertainty (%)
^{12}C in InN	Lisbon/RBI	0.055	178.1	12.7
		0.070	200.7	10.5
		0.088	225.1	8.3
		0.113	250.0	6.1
		0.143	274.0	4.3
		0.182	295.4	3.2
		0.232	312.9	3.3
		0.294	325.8	3.6
		0.375	333.5	3.7
		0.476	340.5	3.6
		0.606	341.4	3.6
		0.771	333.9	3.7
		0.980	320.6	3.9
^{16}O in InN	Lisbon/RBI	0.025	182.4	14.7
		0.032	199.6	12.7
		0.041	219.3	10.4
		0.052	241.6	8.0
		0.066	266.1	5.5
		0.084	292.9	3.5
		0.107	321.6	2.5
		0.136	351.4	3.0
		0.174	381.3	3.5
		0.221	410.2	3.6
		0.281	436.7	3.5
		0.357	459.1	3.4
		0.454	477.8	3.3
		0.577	495.6	3.3
		0.733	501.0	3.5
		0.933	493.0	3.8

TABLE 34. STOPPING POWER DATA MEASURED WITHIN THE SCOPE OF THE CRP (cont.)

System	Laboratory	Energy (MeV/nucleon)	ε (eV/(10^{15} at./cm^2)	Uncertainty (%)
^{12}C in Mylar	iThemba LABS	0.209	118.0	0.075
		0.244	120.7	0.075
		0.276	120.8	0.075
		0.306	121.5	0.075
		0.335	121.1	0.075
		0.365	118.7	0.075
		0.392	114.2	0.075
		0.423	112.7	0.075
		0.446	108.6	0.075
		0.475	109.8	0.075
		0.500	107.8	0.075
		0.528	105.0	0.075
		0.553	102.6	0.075
		0.583	99.9	0.075
		0.609	104.6	0.075
		0.631	98.8	0.075
^{16}O in Mylar	iThemba LABS	0.221	163.7	0.075
		0.242	167.5	0.075
		0.264	166.7	0.075
		0.286	172.5	0.075
		0.312	168.2	0.075
		0.329	169.2	0.075
		0.349	166.2	0.075
		0.390	166.1	0.075
		0.411	166.3	0.075
		0.431	169.1	0.075
		0.470	162.8	0.075
		0.498	162.1	0.075
		0.513	156.9	0.075
		0.555	152.3	0.075

TABLE 34. STOPPING POWER DATA MEASURED WITHIN THE SCOPE OF THE CRP (cont.)

System	Laboratory	Energy (MeV/nucleon)	ε (eV/(10^{15} at./cm^2))	Uncertainty (%)
^{19}F in Mylar	iThemba LABS	0.202	180.9	0.075
		0.238	183.5	0.075
		0.264	190.6	0.075
		0.290	194.4	0.075
		0.313	194.6	0.075
		0.336	195.5	0.075
		0.355	192.7	0.075
		0.380	192.3	0.075
		0.409	190.4	0.075
		0.428	189.9	0.075
		0.449	187.4	0.075
		0.469	185.1	0.075
		0.486	181.7	0.075
		0.508	177.2	0.075
		0.529	180.1	0.075
		0.544	176.3	0.075
^{24}Mg in Mylar	iThemba LABS	0.176	219.3	0.075
		0.193	230.0	0.075
		0.210	231.0	0.075
		0.229	243.4	0.075
		0.250	251.8	0.075
		0.265	255.1	0.075
		0.282	262.2	0.075
		0.299	266.2	0.075
		0.329	265.8	0.075
		0.344	266.8	0.075
		0.357	269.9	0.075
		0.374	264.9	0.075
		0.392	259.2	0.075
		0.405	265.4	0.075
		0.421	266.1	0.075
		0.441	272.1	0.075

TABLE 34. STOPPING POWER DATA MEASURED WITHIN THE SCOPE OF THE CRP (cont.)

System	Laboratory	Energy (MeV/nucleon)	ε (eV/(10^{15} at./cm^2)	Uncertainty (%)
^{28}Si in Mylar	iThemba LABS	0.172	233.5	0.075
		0.189	244.1	0.075
		0.206	253.8	0.075
		0.225	264.5	0.075
		0.239	269.8	0.075
		0.255	275.4	0.075
		0.269	279.2	0.075
		0.282	283.1	0.075
		0.296	282.5	0.075
		0.309	287.9	0.075
		0.324	287.5	0.075
		0.335	288.0	0.075
		0.349	290.3	0.075
		0.362	290.5	0.075
		0.372	292.4	0.075
		0.385	290.6	0.075
		0.398	293.4	0.075
		0.411	300.2	0.075
		0.421	298.7	0.075

Note: RBI — Ruđer Bošković Institute.

REFERENCES

[1] INTERNATIONAL ATOMIC ENERGY AGENCY, Report of the Technical Meeting on the Status of Software for Ion Beam Analysis in Materials Development, IAEA, Vienna (2002).

[2] INTERNATIONAL ATOMIC ENERGY AGENCY, Report of the Consultants Meeting on Evaluation and Intercomparison of Software for Accelerator Science, IAEA, Vienna (2003).

[3] BARRADAS, N.P., et al., International Atomic Energy Agency intercomparison of ion beam analysis software, Nucl. Instrum. Methods Phys. Res. B **262** (2007) 281–303.

[4] CURIE, M., Sur la pénétration des rayons de Becquerel non déviables par le champ magnétique, Comptes Rendus **130** (1900) 76.

[5] PAUL, H., Comparing experimental stopping power data for positive ions with stopping tables, using statistical analysis, Nucl. Instrum. Methods Phys. Res. B **273** (2012) 15–17.

[6] FINE, J., NAVINSEK, B., NIST oxide-marker-layer standard reference material (SRM 2136) for depth profile analysis, Surf. Interface Anal. **23** (1995) 391–392.

[7] RAUHALA, E., ZIEGLER, J.F., "Energy loss and energy straggling", Handbook of Modern Ion Beam Analysis, 2nd edn (WANG, Y., NASTASI, M., Eds), Materials Research Society, Warrendale, PA (2009) 5–25.

[8] SIGMUND, P., Stopping power: Wrong terminology, ICRU News (2000) 16.

[9] SZILÁGYI, E., Energy spread in ion beam analysis, Nucl. Instrum. Methods Phys. Res. B **161–163** (2000) 37–47.

[10] AMSEL, G., BATTISTIG, G., L'HOIR, A., Small angle multiple scattering of fast ions, physics, stochastic theory and numerical calculations, Nucl. Instrum. Methods Phys. Res. B **201** (2003) 325–388.

[11] ZIEGLER, J.F., BIERSACK, J.P., LITTMARK, U., The Stopping and Range of Ions in Solids, Pergamon Press, New York (1985).

[12] BOHR, N., On the theory of the decrease of velocity of moving electrified particles on passing through matter, Phil. Mag. **25** (1913) 10–31.

[13] INTERNATIONAL COMMISSION ON RADIATION UNITS AND MEASUREMENTS, Stopping of Ions Heavier than Helium, ICRU Report 73, ICRU, Bethesda, MD (2005), Errata and Addenda (2009).

[14] INTERNATIONAL COMMISSION ON RADIATION UNITS AND MEASUREMENTS, Stopping Powers and Ranges for Protons and Alpha Particles, ICRU Report 49, ICRU, Bethesda, MD (1993).

[15] SIGMUND, P., SCHINNER, A., Shell correction in stopping theory, Nucl. Instrum. Methods Phys. Res. B **243** (2006) 457–460.

[16] SIGMUND, P., SCHINNER, A., Anatomy of the Barkas effect, Nucl. Instrum. Methods Phys. Res. B **212** (2003) 110–117.

[17] SØRENSEN, A.H., On the nonperturbative contributions to the stopping of H- and He-like heavy ions, Nucl. Instrum. Methods Phys. Res. B **264** (2007) 240–248.

[18] BARRADAS, N.P., JEYNES, C., WEBB, R.P., Simulated annealing analysis of Rutherford backscattering data, Appl. Phys. Lett. **71** (1997) 291.

[19] ZIEGLER, J.F., ZIEGLER, M.D., BIERSACK, J.P., SRIM — The stopping and range of ions in matter (2010), Nucl. Instrum. Methods Phys. Res. B **268** (2010) 1818–1823.
[20] PAUL, H., SCHINNER, A., An empirical approach to the stopping power of solids and gases for ions from ^{3}Li to ^{18}Ar, Nucl. Instrum. Methods Phys. Res. B **179** (2001) 299–315.
[21] PAUL, H., SCHINNER, A., An empirical approach to the stopping power of solids and gases for ions from ^{3}Li to ^{18}Ar: Part II, Nucl. Instrum. Methods Phys. Res. B **195** (2002) 166–174.
[22] GEISSEL, H., WEICK, H., SCHEIDENBERGER, C., BIMBOT, R., GARDÈS, D., Experimental studies of heavy-ion slowing down in matter, Nucl. Instrum. Methods Phys. Res. B **195** (2002) 3–54.
[23] SCHIWIETZ, G., GRANDE, P.L., Stopping of protons — Improved accuracy of the UCA model, Nucl. Instrum. Methods Phys. Res. B **273** (2012) 1–5.
[24] AGOSTINELLI, S., et al., Geant4 — A simulation toolkit, Nucl. Instrum. Methods Phys. Res. A **506** (2003) 250–303.
[25] ALLISON, J., et al., Geant4 developments and applications, IEEE Trans. Nucl. Sci. **53** (2006) 270–278.
[26] MAYER, M., Technical Report IPP9/113, Max Planck Institute for Plasma Physics, Garching (1997).
[27] BARRADAS, N.P., ALVES, E., SIKETIĆ, Z., BOGDANOVIĆ RADOVIĆ, I., Stopping power of He, C and O in InN, AIP Conf. Proc. **1336** (2011) 319.
[28] MERTENS, P., How to measure absolute stopping cross sections by backscattering and transmission methods: Part II. Transmission, Nucl. Instrum. Methods Phys. Res. B **27** (1987) 315–322.
[29] TRZASKA, W.H., ALANKO, T., LYAPIN, V., RÄISÄNEN, J., A novel method for obtaining continuous stopping power curves, Nucl. Instrum. Methods Phys. Res. B **183** (2001) 203–211.
[30] ALANKO, T., et al., Simultaneous wide-range stopping power determination for several ions, Nucl. Instrum. Methods Phys. Res. B **190** (2002) 60–63.
[31] WILKINS, B.D., FLUSS, M.J., KAUFMAN, S.B., GROSS, C.E., STEINBERG, E.P., Pulse-height defects for heavy ions in a silicon surface-barrier detector, Nucl. Instrum. Methods **92** (1971) 381–391.
[32] ZHANG, Y., WEBER, W. J., Role of energy partitioning on electron-hole recombination, trapping, and detection in silicon detectors, Phys. Rev. B **82** (2010).
[33] KONAC, G., KALBITZER, S., KLATT, Ch., NIEMANN, D., STOLL, R., Energy loss and straggling of H and He ions of keV energies in Si and C, Nucl. Instrum. Methods Phys. Res. B **136–138** (1998) 159–165.
[34] KREISSIG, U., GRÖTZSCHEL, R., BEHRISCH, R., Simultaneous measurement of the hydrogen isotopes H, D, T and ^{3}He with HIERD, Nucl. Instrum. Methods Phys. Res. B **85** (1994) 71–74.
[35] LIGUORI NETO, R., ADDED, N., COUTINHO, F.A.S., A new experimental method for precise energy loss measurements, Nucl. Instrum. Methods Phys. Res. B **161–163** (2000) 159–163.

[36] TIMMERS, H., STENSTROM, K., GRACZYK, M., WHITLOW, H.J., Energy loss measurements for mass-14 ions using a patterned stopping medium on a PIN diode, Nucl. Instrum. Methods Phys. Res. B **219–220** (2004) 263–267.
[37] RIBAS, R.V., et al., Stopping power of Au for silver ions at low velocities, Nucl. Instrum. Methods Phys. Res. B **211** (2003) 453–459.
[38] BERGSMANN, M., HÖRLSBERGER, P., KASTNER, F., BAUER, P., Evaluation of energy loss from DUAL-TOF spectra, Nucl. Instrum. Methods Phys. Res. B **136–138** (1998) 1218–1222.
[39] LEAVITT, J.A., McINTYRE, L.C., Jr., "Backscattering spectrometry", Handbook of Modern Ion Beam Analysis, 2nd edn (WANG, Y., NASTASI, M., Eds), Materials Research Society, Warrendale, PA (2009) 43–80.
[40] BAUER, P., How to measure absolute stopping cross sections by backscattering and by transmission methods: Part I. Backscattering, Nucl. Instrum. Methods Phys. Res. B **27** (1987) 301–314.
[41] LENNARD, W.N., XIA, H., KIM, J.K., Revisiting the stopping powers of Si and SiO_2 for ^{4}He ions: 0.5–2.0 MeV, Nucl. Instrum. Methods Phys. Res. B **215** (2004) 297–307.
[42] LIN, W.K., MATTESON, S., POWERS, D., α-Particle stopping cross section of gold and silver as measured from thick targets, Phys. Rev. B **10** (1974) 3746–3755.
[43] ASLANOGLOU, X.A., ASSIMAKOPOULOS, P.A., KOKKORIS, M., KOSSIONIDES, E., Simulations of channelling spectra in the system p+^{28}Si, Nucl. Instrum. Methods Phys. Res. B **140** (1998) 294–302.
[44] BARRADAS, N.P., JEYNES, C., WEBB, R.P., WENDLER, E., Accurate determination of the stopping power of ^{4}He in Si using Bayesian inference, Nucl. Instrum. Methods Phys. Res. B **194** (2002) 15–25.
[45] BARRADAS, N.P., RAUHALA, E., "Data analysis software for ion beam analysis", Handbook of Modern Ion Beam Analysis, 2nd edn (WANG, Y., NASTASI, M., Eds), Materials Research Society, Warrendale, PA (2009) 305–345.
[46] NIEMANN, D., KONAC, G., KALBITZER, S., Stopping power measurements of ^{1}H, ^{4}He and ^{14}N in Si in the energy range of 0.02–1 MeV/amu, Nucl. Instrum. Methods Phys. Res. B **118** (1996) 11–18.
[47] PASCUAL-IZARRA, C., GARCÍA, G., An efficient method for stopping force determination, Nucl. Instrum. Methods Phys. Res. B **225** (2004) 383–391.
[48] PASCUAL-IZARRA, C., BARRADAS, N.P., GARCÍA, G., CLIMENT-FONT, A., Experimental stopping forces for He, C, O, Al and Si ions in Al_2O_3 in the energy range of 40–1250 keV/nucleon, Nucl. Instrum. Methods Phys. Res. B **239** (2005) 135–146.
[49] HAUSER, U., NEUWIRTH, W., PIETSCH, W., RICHTER, K., On the determination of collision cross sections by nuclear Doppler shift, Z. Phys. **269** (1974) 181–188.
[50] ARSTILA, K., An experimental method for precise determination of electronic stopping powers for heavy ions, Nucl. Instrum. Methods Phys. Res. B **168** (2000) 473–483.
[51] PAUL, H., SCHINNER, A., Does the result of a stopping power measurement depend on the method used? Phys. Scr. **69** (2004) C41.
[52] JOKINEN, J., et al., Comparison of TOF–ERDA and nuclear resonance reaction techniques for range profile measurements of keV energy implants, Nucl. Instrum. Methods Phys. Res. B **119** (1996) 533–542.

[53] LÖFFLER, M., SCHEERER, H.J., VONACH, H., The ion optical properties of the Munich Q3D-spectrograph investigated by means of a special experimental ray tracing method, Nucl. Instrum. Methods **111** (1973) 1–12.
[54] DOLLINGER, G., Elastic recoil detection analysis with atomic depth resolution, Nucl. Instrum. Methods Phys. Res. B **79** (1993) 513–517.
[55] SILSON Ltd, Standard silicon nitride membrane windows, www.silson.com
[56] JOINT COMMITTEE FOR GUIDES IN METROLOGY, Evaluation of Measurement Data — Guide to the Expression of Uncertainty in Measurement JCGM 100:2008 (2008), www.iso.org/sites/JCGM/GUM/JCGM100/C045315e-html/C045315e.html
[57] SJÖLAND, K.A., MUNNIK, F., WÄTJEN, U., Uncertainty budget for ion beam analysis, Nucl. Instrum. Methods Phys. Res. B **161** (2000) 275–280.
[58] JEYNES, C., BARRADAS, N.B., "Pitfalls in ion beam analysis", Handbook of Modern Ion Beam Analysis, 2nd edn (WANG, Y., NASTASI, M., Eds), Materials Research Society, Warrendale, PA (2009) 347–383.
[59] JOINT COMMITTEE FOR GUIDES IN METROLOGY, Evaluation of Measurement Data — Supplement 1 to the "Guide to the expression of uncertainty in measurement" — Propagation of Distributions Using a Monte Carlo Method, JCGM 101:2008 (2008), www.bipm.org/utils/common/documents/jcgm/JCGM_101_2008_E.pdf
[60] FREY, C.M., DOLLINGER, G., BERGMAIER, A., FAESTERMANN, T., MAIER-KOMOR, P., Charge state dependence of the stopping power of 1 MeV/A ^{58}Ni-ions in the thin carbon foils, Nucl. Instrum. Methods Phys. Res. B **99** (1995) 205–209.
[61] ANDERSEN, H.H., BESENBACHER, F., LOFTAGER, P., MÖLLER, W., Large-angle scattering of light ions in the weakly screened Rutherford region, Phys. Rev. A **21** (1980) 1891–1901.
[62] SCHIETTEKATTE, F., Fast Monte Carlo for ion beam analysis simulations, Nucl. Instrum. Methods Phys. Res. B **266** (2008) 1880–1885.
[63] JEYNES, C., KIMBER, A.C., High accuracy data from Rutherford back-scattering spectra: Measurements of the range and straggling of 60–400 keV As implants into Si, J. Phys. D Appl. Phys. **18** (1985) L93.
[64] INTERNATIONAL ATOMIC ENERGY AGENCY, Stopping Power of Matter for Ions — Graphs, Data, Comments and Programs, www-nds.iaea.org/stopping/
[65] LEE, P.M., Bayesian Statistics, 2nd edn, Arnold, London (1997).
[66] BARRADAS, N.P., JEYNES, C., JENKIN, M., MARRIOTT, P.K., Bayesian error analysis of Rutherford backscattering spectra, Thin Solid Films **343–344** (1999) 31–34.
[67] SMITH, C.R., GRANDY, W.T. (Eds), Maximum-Entropy and Bayesian Methods in Inverse Problems, Springer, Dordrecht (1985).
[68] PÁSZTI, F., MANUABA, A., HAJDU, C., MELO, A.A., DA SILVA, M.F., Current measurement on MeV energy ion beams, Nucl. Instrum. Methods Phys. Res. B **47** (1990) 187–192.

[69] PASCUAL-IZARRA, C., BARRADAS, N.P., Introducing routine pulse height defect corrections in IBA, Nucl. Instrum. Methods Phys. Res. B **266** (2008) 1866–1870.
[70] BEHRISCH, R. (Ed.), "Sputtering by particle bombardment I", Topics in Applied Physics, Vol. 47, Springer Verlag, Berlin (1981).
[71] ASSMANN, W., et al., ERDA with very heavy ion beams, Nucl. Instrum. Methods Phys. Res. B **118** (1996) 242–250.
[72] DÖBELI, M., KOTTLER, C., GLAUS, F., SUTER, M., ERDA at the low energy limit, Nucl. Instrum. Methods Phys. Res. B **241** (2005) 428–435.
[73] HARIKUMAR, V., et al., Stopping power of carbon for Si, Fe, Ni and Cu ions using the ERDA technique, Nucl. Instrum. Methods Phys. Res. B **129** (1997) 143–146.
[74] ANTHONY, J.M., LANFORD, W.A., Stopping power and effective charge of heavy ions in solids, Phys. Rev. A **25** (1982) 1868–1879.
[75] ZHANG, Y., High-precision measurement of electronic stopping powers for heavy ions using high-resolution time-of-flight spectrometry, Nucl. Instrum. Methods Phys. Res. B **196** (2002) 1–15.
[76] ZHANG, Y., POSSNERT, G., WEBER, W.J., Measurement of electronic stopping power of swift heavy ions using high-resolution time-of-flight spectrometer, Appl. Phys. Lett. **80** (2002) 4662–4664.
[77] FREY, C.M., DOLLINGER, G., BERGMAIER, A., FAESTERMANN, T., MAIER-KOMOR, P., Charge state dependence of the stopping power of 1 MeV/A ^{58}Ni ions, Nucl. Instrum. Methods Phys. Res. B **107** (1992) 31–35.
[78] ABDESSELAM, M., et al., Cu, I and Au stopping powers in solid targets, Nucl. Instrum. Methods Phys. Res. B **72** (1992) 7–15.
[79] BIMBOT, R., et al., Stopping power measurements for 4–5 MeV/nucleon ^{16}O, ^{40}Ar, ^{63}Cu and ^{84}Kr in C, Al, Ni, Ag and Au, Nucl. Instrum. Methods **153** (1978) 161–169.
[80] HARIKUMAR, V., et al., Energy loss of MeV heavy ions in carbon, Nucl. Instrum. Methods Phys. Res. B **108** (1996) 223–226.
[81] HVELPLUND P., FASTRUP, B., Stopping cross section in carbon of 0.2–1.5-MeV atoms with $21 \leq Z_1 \leq 39$, Phys. Rev. **165** (1968) 408–414.
[82] KUMAR, S., SHARMA, S.K., NATH, N., Stopping power of carbon for heavy ions up to copper, Radiat. Effects Defects Solids **139** (1996) 197–206.
[83] SHARMA, A., et al., An experimental study of stopping power for MeV heavy ions, J. Phys. G Nucl. Part. Phys. **25** (1999) 135–142.
[84] GEISSEL, H., et al., A time-of-flight method for stopping power measurements of bunched ion beams, Nucl. Instrum. Methods Phys. Res. **206** (1983) 609–612.
[85] BROWN, M.D., MOAK, C.D., Stopping powers of some solids for 30–90- MeV ^{238}U ions, Phys. Rev. B **6** (1972) 90–94.
[86] KNYAZHEVA, G.N., et al., Energy losses of ^{252}Cf fission fragments in thin foils, Nucl. Instrum. Methods B **248** (2006) 7–15.
[87] BRIDWELL, L.B., NORTHCLIFFE, L.C., DATZ, S., MOAK, C.D., LUTZ, H.O., Stopping powers for iodine ions at energies up to 200 MeV, Phys. Rev. **159** (1967) 276–277.

[88] JOKINEN, J., Stopping powers of C, Al and Cu for use in ERDA analyses with probing MeV energy ^{197}Au ions, Nucl. Instrum. Methods Phys. Res. B **124** (1997) 447–452.
[89] OUICHAOUI, S., et al., Stopping powers of Al, Cu, Ag and Au media for 1.47 MeV/u ^{127}I, 2 MeV/u ^{32}S and ^{79}Br ions, Nucl. Instrum. Methods Phys. Res. B **95** (1995) 463–469.
[90] APEL, F., MÜLLER-JAHREIS, U., ROCKSTROH, G., SCHWABE, S., On the Z_2-dependence of electronic stopping cross sections, Phys. Status Solidi A **3** (1970) K173–K175.
[91] SANTRY, D.C., WERNER, R.D., Stopping power measurements of C, Al, Si, Ti, Ni, Ag, Au and Mylar using radioactive alpha sources, Nucl. Instrum. Methods Phys. Res. B **1** (1984) 13–15.
[92] LIU, J., ZHENG, Z., CHU, W.-K., Stopping cross sections of C, Al, and Si for ^{7}Li ions, Nucl. Instrum. Methods Phys. Res. B **118** (1996) 24–28.
[93] JIANG, W., GRÖTZSCHEL, R., PILZ, W., SCHMIDT, B., MÖLLER, W., Random and channelling stopping powers and charge-state distributions in silicon for 0.2–1.2 MeV/u positive heavy ions, Phys. Rev. B **59** (1999) 226–234.
[94] AZEVEDO, G.M., BEHAR, M., DIAS, J.F., GRANDE, P.L., DA SILVA, D.L., Random and channelling stopping powers of He and Li ions in Si, Phys. Rev. B **65** (2002).
[95] DOS SANTOS, J.H.R., et al., Electronic stopping power of ^{10}B in Si in random and <100> channelling directions, Phys. Rev. B **55** (1997) 13651–13657.
[96] ZHANG, Y., WEBER, W.J., WHITLOW, H.J., Electronic stopping powers for heavy ions in silicon, Nucl. Instrum. Methods Phys. Res. B **215** (2004) 48–56.
[97] SANTRY, D.C., WERNER, R.D., Measured stopping powers of ^{12}C and ^{14}N ions in thin elemental foils, Nucl. Instrum. Methods Phys. Res. B **53** (1991) 7–14.
[98] KURONEN, A., RÄISÄNEN, J., KEINONEN, J., TIKKANEN, P., RAUHALA, E., Electronic stopping power for ^{7}Li, ^{11}B, ^{12}C, ^{14}N and ^{16}O at energies 0.4 to 2.1 MeV/nucleon in Ta and Au, and for ^{12}C at energies 0.4, 0.8 and 1.4 MeV/nucleon in 18 elemental solids, Nucl. Instrum. Methods Phys. Res. B **35** (1988) 1–6.
[99] BUSSMANN, U., HECKING, N., HEIDEMANN, K.F., TE KAAT, E., Ranges and electronic stopping powers of 1–24 MeV ^{12}C and ^{14}N ions in Si targets from optical reflectivity measurements on bevelled samples, Nucl. Instrum. Methods Phys. Res. B **15** (1986) 105–108.
[100] PERKOWSKI, J., et al., The first experimental values for the stopping power of Au ions in nickel, Acta Phys. Pol. B **39** (2008) 507–511.
[101] L'HOIR, A., COHEN, C., AMSEL, G., "Experimental study of the stopping power and energy straggling of MeV ^{4}He, ^{12}C, ^{14}N and ^{16}O ions in amorphous aluminium oxide", Ion Beam Surface Layer Analysis (MEYER, O., LINKER, G., KÄPPELER, F., Eds), Plenum, New York (1976) 965.
[102] ZHANG, Y., WEBER, W.J., McCREADY, D.E., Experimental determination of electronic stopping for ions in silicon dioxide, Appl. Phys. Lett. **87** (2005).
[103] LU, X., XIA, Z., ZHENG, T., SHEN, Y., Stopping powers of C, Al, Ti, Cu, Nb and Ag for ^{16}O and ^{19}F ions, Nucl. Instrum. Methods Phys. Res. B **168** (2000) 287–293.

[104] ZHANG, Y., et al., Electronic stopping forces of heavy ions in metal oxides, Nucl. Instrum. Methods Phys. Res. B **249** (2006) 18–21.
[105] ZHANG, Y., WEBER, W.J., Response of materials to single ion events, Nucl. Instrum. Methods Phys. Res. B **267** (2009) 1705–1712.
[106] ZHANG, Y., WEBER, W.J., GROVE, D.A., JENSEN, J., POSSNERT, G., Electronic stopping powers for heavy ions in niobium and tantalum pentoxides, Nucl. Instrum. Methods Phys. Res. B **250** (2006) 62–65.
[107] SUN, G., et al., Energy loss and straggling of heavy ions in silicon nitride in the low MeV energy range, Nucl. Instrum. Methods Phys. Res. B **256** (2007) 586–590.
[108] JIN, C., et al., Stopping power of Mylar for low-velocity ^{11}B, ^{12}C, and ^{16}O ions, Phys. Rev. B **48** (1993) 6858–6861.
[109] RAUHALA, E., RÄISÄNEN, J., Stopping powers and energy loss of 3–22-MeV ^{12}C ions in Havar, nickel, Kapton, and Mylar, Phys. Rev. B **37** (1988) 9249–9253.
[110] HARI KUMAR, V., et al., Stopping power of Mylar and carbon, Radiat. Effects Defects Solids **132** (2006) 211–214.
[111] RÄISÄNEN, J., RAUHALA, E., Stopping of Havar, nickel, Kapton, and Mylar for 5–19-MeV ^{16}O ions, Phys. Rev. B **36** (1987) 9776–9780.
[112] RÄISÄNEN, J., RAUHALA, E., Stopping powers and energy loss of Mylar, Kapton, Havar, and Ni for 10 Z = 3–17 ions in the energy range 0.2–2.1 MeV/amu, Phys. Rev. B Condens. Matter **41** (1990) 3951–3958.
[113] BOTH, G., KROTZ, R., LOHMAN, K., NEUWIRTH, W., Density dependence of stopping cross sections measured in liquid ethane, Phys. Rev. A **28** (1983) 3212–3216.
[114] TSCHALÄR, C., Straggling distributions of large energy losses, Nucl. Instrum. Methods **61** (1968) 141–156.
[115] MSIMANGA, M., PINEDA-VARGAS, C.A., COMRIE, C.M., MURRAY, S., Heavy ion energy loss straggling data from time of flight stopping force measurements, Nucl. Instrum. Methods Phys. Res. B **273** (2012) 6–10.
[116] YANG, Q., O'CONNOR, D.J., WANG, Z., Empirical formulae for energy loss straggling of ions in matter, Nucl. Instrum. Methods Phys. Res. B **61** (1991) 149–155.
[117] GURBICH, A.F., On the concept of an actual Coulomb barrier, Nucl. Instrum. Methods Phys. Res. B **217** (2004) 183–186.
[118] L'ECUYER, J., DAVIES, J.A., MATSUNAMI, N., How accurate are absolute Rutherford backscattering yields, Nucl. Instrum. Methods **160** (1979) 337–346.
[119] ARSTILA, K., SAJAVAARA, T., KEINONEN, J., Monte Carlo simulation of multiple and plural scattering in elastic recoil detection, Nucl. Instrum. Methods Phys. Res. B **174** (2001) 163–172.
[120] ARSTILA, K., SAJAVAARA, T., KEINONEN, J., MCERD with Graphical Interface,
www.jyu.fi/fysiikka/en/research/accelerator/abasedmat/software
[121] GTK+, GIMP Toolkit,
www.gtk.org/
[122] BARRADAS, N.P., LORENZ, K., DARAKCHIEVA, V., ALVES, E., A double scattering analytical model for elastic recoil detection analysis, AIP Conf. Proc. **1336** (2011) 314.

[123] BARRADAS, N.P., et al., Thin film depth profiling using simultaneous particle backscattering and nuclear resonance profiling, Nucl. Instrum. Methods Phys. Res. B **268** (2010) 1829–1832.
[124] BAUER, P., STEINBAUER, E., BIERSACK, J.P., The width of an RBS spectrum: Influence of plural and multiple scattering, Nucl. Instrum. Methods Phys. Res. B **64** (1992) 711–715.
[125] BARRADAS, N.P., The width of an RBS spectrum revisited: Influence of multiple scattering, Nucl. Instrum. Methods Phys. Res. B **270** (2012) 44–46.

BIBLIOGRAPHY

Several of the stopping powers measured during this coordinated research project have been published in international journals, presented at international conferences and meetings, and made available to existing relevant stopping power databases. At the time of publication of this report, 29 publications had been published as a result of the activities of the coordinated research project (listed below). During the project, research activities and results contributed to three masters' and three PhD theses. In time, these new results will increase the accuracy and reliability of widely used semiempirical stopping power values such as those generated by the SRIM code. This bibliography lists publications at the time of publication of this report.

AMMI, H., et al., Stopping power measurements of heavy ions ($3 \leq Z_1 \leq 14$) in Mylar foil by time-of-flight spectrometry, Nucl. Instrum. Methods Phys. Res. B **269** (2011) 386–391.

ARSTILA, K., et al., Potku — New analysis software for heavy ion elastic recoil detection analysis, Nucl. Instrum. Methods Phys. Res. B **331** (2014) 34–41.

BARRADAS, N.P., The width of an RBS spectrum revisited: Influence of multiple scattering, Nucl. Instrum. Methods Phys. Res. B **270** (2012) 44–46.

BARRADAS, N.P., ALVES, E., FONSECA, M., SIKETIĆ, Z., BOGDANOVIĆ RADOVIĆ, I., Stopping power of C, O and Cl in tantalum oxide, Nucl. Instrum. Methods Phys. Res. B **332** (2014) 152–155.

BARRADAS, N.P., ALVES, E., SIKETIĆ, Z., BOGDANOVIĆ RADOVIĆ, I.

Stopping power of different ions in Si measured with a bulk sample method and Bayesian inference data analysis, AIP Conf. Proc. **1099** (2009) 331.

Stopping power of He, C and O in InN, AIP Conf. Proc. **1336** (2011) 319.

Stopping power of C in Si, Nucl. Instrum. Methods Phys. Res. B **273** (2012) 30–32.

Stopping power of He, C and O in GaN, Nucl. Instrum. Methods Phys. Res. B **273** (2012) 26–29.

Stopping power of He, C and O in TiO_2, Nucl. Instrum. Methods Phys. Res. B **273** (2012) 22–25.

BARRADAS, N.P., BERGMAIER, A., MIZOHATA, K., MSIMANGA, M., RÄISÄNEN, J., SAJAVAARA, T., SIMON, A., Determination of molecular stopping cross section of ^{12}C, ^{16}O, ^{28}Si, ^{35}Cl, ^{58}Ni, ^{79}Br, and ^{127}I in silicon nitride, Nucl. Instrum. Methods Phys. Res. B **360** (2015) 90–96.

BARRADAS, N.P., LORENZ, K., DARAKCHIEVA, V., ALVES, E., A double scattering analytical model for elastic recoil detection analysis, AIP Conf. Proc. **1336** (2011) 314.

BARRADAS, N.P., MARQUES, J.G., ALVES, E., Stopping power of ^{1}H and ^{4}He in lithium niobate, Nucl. Instrum. Methods Phys. Res. B **332** (2014) 330–333.

BARRADAS, N.P., MATEUS, R., FONSECA, M., REIS, M.A., LORENZ, K., VICKRIDGE, I., Thin film depth profiling using simultaneous particle backscattering and nuclear resonance profiling, Nucl. Instrum. Methods Phys. Res. B **268** (2010) 1829–1832.

DOLLINGER, G., et al., Nanosecond pulsed proton microbeam, Nucl. Instrum. Methods Phys. Res. B **267** (2009) 2008–2012.

EL-HAJJ, H., et al., Characteristics of boron δ-doped diamond for electronic applications, Diam. Relat. Mater. **17** (2008) 409–414.

HABLE, V., et al., The live cell irradiation and observation setup at SNAKE, Nucl. Instrum. Methods Phys. Res. B **267** (2009) 2090–2097.

LORENZ, K., et al., Hydrogen in group-III nitrides: An ion beam analysis study, AIP Conf. Proc. **1336** (2011) 310–313.

MIZOHATA, K., KEINONEN, J., RÄISÄNEN, J., Stopping forces of polyimide, vyns, formvar, and polysulfone for Cl, Br, and I ions, Nucl. Instrum. Methods Phys. Res. B **280** (2012) 74–78.

MIZOHATA, K., RÄISÄNEN, J., KEINONEN, J., HARKONEN, E., PALMANS, J., RITALA, M., Stopping cross sections of atomic layer deposited Al_2O_3 and Ta_2O_5 and of Si_3N_4 for ^{12}C, ^{16}O, ^{35}Cl, ^{79}Br and ^{127}I ions, Nucl. Instrum. Methods Phys. Res. B **300** (2013) 1–5.

MSIMANGA, M., Development of a Time of Flight–Energy Spectrometer for Applications in Heavy Ion–Elastic Recoil Detection Thin Film Analysis, PhD Thesis, Univ. of Cape Town (2010).

MSIMANGA, M., COMRIE, C.M., PINEDA-VARGAS, C.A., MURRAY, S., Experimental stopping powers of Al, Mg, F and O ions in ZrO_2 in the 0.1–0.6 MeV/u energy range, Nucl. Instrum. Methods Phys. Res. B **268** (2010) 1772–1775.

— Heavy ion energy loss straggling data from time of flight stopping force measurements, Nucl. Instrum. Methods Phys. Res. B **273** (2012) 6–10.

MSIMANGA, M., COMRIE, C.M., PINEDA-VARGAS, C.A., MURRAY, S., BARK, R., DOLLINGER, G., A time of flight–energy spectrometer for stopping power measurements in heavy ion–ERD analysis at iThemba LABS, Nucl. Instrum. Methods Phys. Res. B **267** (2009) 2671–2674.

NEUMAIER, P., et al., Bimodal range distributions of low-energy carbon ions in tetrahedral amorphous carbon, EPL **90** (2010) 46002.

PASCUAL-IZARRA, C., BARRADAS, N.P., Introducing routine pulse height defect corrections in IBA, Nucl. Instrum. Methods Phys. Res. B **266** (2008) 1866–1870.

SCHMID, T.E., et al., Differences in the kinetics of γ-H2AX fluorescence decay after exposure to low and high LET radiation, Int. J. Radiat. Biol. **86** (2010) 682–691.

SIKETIĆ, Z., BOGDANOVIĆ RADOVIĆ, I., ALVES, E., BARRADAS, N.P., Stopping power of ^{11}B in Si and TiO_2 measured with a bulk sample method and Bayesian inference data analysis, Nucl. Instrum. Methods Phys. Res. B **268** (2010) 1768–1771.

SIMON, A., et al., New experimental molecular stopping cross section data of Al_2O_3, for heavy ions, Nucl. Instrum. Methods Phys. Res. B **332** (2014) 341–345.

TABORDA, A., ALVES, L.C., BARRADAS, N.P., CHAVES, P.C., REIS, M.A., IBIXFIT: A tool for the analysis of microcalorimeter PIXE spectra, AIP Conf. Proc. **1336** (2011) 276.

ABBREVIATIONS

AFM	atomic force microscopy
ALD	atomic layer deposition
CRP	coordinated research project
ERDA	elastic recoil detection analysis
FWHM	full width at half maximum
GUM	Guide to the Expression of Uncertainty in Measurement
IBA	ion beam analysis
LABS	Laboratory for Accelerator Based Sciences
MCMC	Markov chain Monte Carlo
PIGE	particle induced gamma ray emission
PIXE	particle induced X ray emission
RBS	Rutherford backscattering spectroscopy
SRIM	stopping and range of ions in matter
STIM	scanning tunnelling ion microscopy
TOF	time of flight
TOF–E	time of flight–energy
ZBL	Ziegler, Biersack and Littmark

CONTRIBUTORS TO DRAFTING AND REVIEW

Alves, E.	Instituto Superior Técnico, Portugal
Arstila, K.	University of Jyväskylä, Finland
Barradas, N.P.	Instituto Superior Técnico, Portugal
Bergmaier, A.	Universität der Bundeswehr München, Germany
Bogdanović Radović, I.	Ruđer Bošković Institute, Croatia
Comrie, C.	iThemba LABS, South Africa
Dollinger, G.	Universität der Bundeswehr München, Germany
Härkönen, E.	University of Helsinki, Finland
Heiskanen, J.	University of Jyväskylä, Finland
Jakšić, M.	Ruđer Bošković Institute, Croatia
Julin, J.	University of Jyväskylä, Finland
Laitinen, M.	University of Jyväskylä, Finland
Mizohata, K.	University of Helsinki, Finland
Msimanga, M.	iThemba LABS, South Africa
Paul, H.	University of Linz, Austria
Pineda-Vargas, C.	iThemba LABS, South Africa
Räisänen, J.	University of Helsinki, Finland
Ritala, M.	University of Helsinki, Finland
Sajavaara, T.	University of Jyväskylä, Finland
Siketić, Z.	Ruđer Bošković Institute, Croatia
Simon, A.	International Atomic Energy Agency
Skukan, N.	Ruđer Bošković Institute, Croatia

Research Coordination Meetings

Vienna, Austria: 2–14 November 2007; 26–28 May 2009;
12–14 October 2010; 11–13 October 2011

Consultants Meeting

Vienna, Austria: 7–10 April 2014

IAEA
International Atomic Energy Agency

No. 25

ORDERING LOCALLY

In the following countries, IAEA priced publications may be purchased from the sources listed below or from major local booksellers.

Orders for unpriced publications should be made directly to the IAEA. The contact details are given at the end of this list.

CANADA

Renouf Publishing Co. Ltd
22-1010 Polytek Street, Ottawa, ON K1J 9J1, CANADA
Telephone: +1 613 745 2665 • Fax: +1 643 745 7660
Email: order@renoufbooks.com • Web site: www.renoufbooks.com

Bernan / Rowman & Littlefield
15200 NBN Way, Blue Ridge Summit, PA 17214, USA
Tel: +1 800 462 6420 • Fax: +1 800 338 4550
Email: orders@rowman.com Web site: www.rowman.com/bernan

CZECH REPUBLIC

Suweco CZ, s.r.o.
Sestupná 153/11, 162 00 Prague 6, CZECH REPUBLIC
Telephone: +420 242 459 205 • Fax: +420 284 821 646
Email: nakup@suweco.cz • Web site: www.suweco.cz

FRANCE

Form-Edit
5 rue Janssen, PO Box 25, 75921 Paris CEDEX, FRANCE
Telephone: +33 1 42 01 49 49 • Fax: +33 1 42 01 90 90
Email: formedit@formedit.fr • Web site: www.form-edit.com

GERMANY

Goethe Buchhandlung Teubig GmbH
Schweitzer Fachinformationen
Willstätterstrasse 15, 40549 Düsseldorf, GERMANY
Telephone: +49 (0) 211 49 874 015 • Fax: +49 (0) 211 49 874 28
Email: kundenbetreuung.goethe@schweitzer-online.de • Web site: www.goethebuch.de

INDIA

Allied Publishers
1st Floor, Dubash House, 15, J.N. Heredi Marg, Ballard Estate, Mumbai 400001, INDIA
Telephone: +91 22 4212 6930/31/69 • Fax: +91 22 2261 7928
Email: alliedpl@vsnl.com • Web site: www.alliedpublishers.com

Bookwell
3/79 Nirankari, Delhi 110009, INDIA
Telephone: +91 11 2760 1283/4536
Email: bkwell@nde.vsnl.net.in • Web site: www.bookwellindia.com

ITALY

Libreria Scientifica "AEIOU"
Via Vincenzo Maria Coronelli 6, 20146 Milan, ITALY
Telephone: +39 02 48 95 45 52 • Fax: +39 02 48 95 45 48
Email: info@libreriaaeiou.eu • Web site: www.libreriaaeiou.eu

JAPAN

Maruzen-Yushodo Co., Ltd
10-10 Yotsuyasakamachi, Shinjuku-ku, Tokyo 160-0002, JAPAN
Telephone: +81 3 4335 9312 • Fax: +81 3 4335 9364
Email: bookimport@maruzen.co.jp • Web site: www.maruzen.co.jp

RUSSIAN FEDERATION

Scientific and Engineering Centre for Nuclear and Radiation Safety
107140, Moscow, Malaya Krasnoselskaya st. 2/8, bld. 5, RUSSIAN FEDERATION
Telephone: +7 499 264 00 03 • Fax: +7 499 264 28 59
Email: secnrs@secnrs.ru • Web site: www.secnrs.ru

UNITED STATES OF AMERICA

Bernan / Rowman & Littlefield
15200 NBN Way, Blue Ridge Summit, PA 17214, USA
Tel: +1 800 462 6420 • Fax: +1 800 338 4550
Email: orders@rowman.com • Web site: www.rowman.com/bernan

Renouf Publishing Co. Ltd
812 Proctor Avenue, Ogdensburg, NY 13669-2205, USA
Telephone: +1 888 551 7470 • Fax: +1 888 551 7471
Email: orders@renoufbooks.com • Web site: www.renoufbooks.com

Orders for both priced and unpriced publications may be addressed directly to:

Marketing and Sales Unit
International Atomic Energy Agency
Vienna International Centre, PO Box 100, 1400 Vienna, Austria
Telephone: +43 1 2600 22529 or 22530 • Fax: +43 1 26007 22529
Email: sales.publications@iaea.org • Web site: www.iaea.org/books

18-03461

HANDS-ON TRAINING COURSES USING RESEARCH REACTORS AND ACCELERATORS
Training Course Series No. 57
IAEA-TCS-57 (103 pp; 2014)

ACCELERATOR SIMULATION AND THEORETICAL MODELLING OF RADIATION EFFECTS IN STRUCTURAL MATERIALS
IAEA Nuclear Energy Series No. NF-T-2.2
STI/PUB/1732 (116 pp; 2018)
ISBN 978–92–0–107415–7 Price: €39.00

UTILIZATION OF ACCELERATOR BASED REAL TIME METHODS IN INVESTIGATION OF MATERIALS WITH HIGH TECHNOLOGICAL IMPORTANCE
IAEA Radiation Technology Reports No. 4
STI/PUB/1649 (104 pp; 2015)
ISBN 978–92–0–102314–8 Price: €37.00

NUCLEAR TECHNIQUES FOR CULTURAL HERITAGE RESEARCH
IAEA Radiation Technology Series No. 2
STI/PUB/1501 (205 pp; 2011)
ISBN 978–92–0–114510–9 Price: €58.00

DEVELOPMENT OF A REFERENCE DATABASE FOR PARTICLE INDUCED GAMMA RAY EMISSION (PIGE) SPECTROSCOPY
IAEA-TECDOC-1822 (2017)
ISBN 978–92–0–106317–5 Price: €18.00

Many emerging technologies are based on the development of advanced engineering materials capable of withstanding higher temperatures, higher stresses, and more aggressive corrosive and oxidizing environments than their predecessors. Nuclear analytical facilities and techniques support the development of these new light element composites and alloys, and the use of heavy ions from particle accelerators is particularly valuable in this area. The coordinated research project described in this publication helped to address identified shortcomings and limitations in the use of heavy ions through the delivery of better analytical tools with a higher degree of reliability, accuracy and user confidence. This publication is unique as it includes a detailed description of theory, experimental procedures and data evaluation practice, together with the new stopping power dataset. All these elements will significantly contribute to the improvement of light element analysis and its practice worldwide.

INTERNATIONAL ATOMIC ENERGY AGENCY
VIENNA
ISBN 978–92–0–103517–2
ISSN 0074–1914